SOFT X-RAY DIAGNOSTICS OF TOROIDAL PLASMAS

by

Phillip Anthony Gaisford

Department of Physics

Royal Holloway College

University of London

Submitted for the degree of ~~Doctor of Philosophy~~ MPhil

to the University of London, March 1985

SOFT X-RAY DIAGNOSTICS OF TOROIDAL PLASMAS

P A Gaisford

ABSTRACT

This work is a presentation of the application of soft x-ray measurements to the diagnostics of toroidal plasmas currently of interest in the controlled thermonuclear reaction research program. Soft x-ray techniques are here used in a study of auxiliary plasma heating at the second harmonic of the electron cyclotron resonance (ECRH) in the small (R = 0.3 m, a < 0.1 m) TOSCA tokamak

The importance of soft x-ray diagnostics in relation to the parameters of current fusion plasma experiments is shown by detailing the dependence of the soft x-ray radiation power on the plasma conditions, through a consideration of the contributing atomic processes. The contribution from soft x-ray measurements to the existing body of knowledge of tokamak physics is outlined by way of a review of the more significant results obtained to date. It is shown how radially resolved measurements of the soft x-ray flux may be used in conjunction with soft x-ray spectral measurements to deduce the form of the distribution in minor cross-section of the local electron temperature in a tokamak. The profiles obtained in this way from TOSCA are comparable with laser scattering measurements performed on the Alcator A and TM-3 tokamaks. This work is extended to the study of the effect of ECRH in TOSCA, which is found to be strongly localised in major radius at electron densities well above the extraordinary mode cut-off condition, and also strongly asymmetric with respect to the minor axis. Some progress is made in evaluating the electron temperature profile during ECRH. The local electron temperature at the ECR could at least be doubled. The significant role of trapped electrons under ECRH is discussed.

ACKNOWLEDGEMENTS

I wish to express my thanks to Drs D C Robinson of the Culham Laboratory, and to Dr E R Wooding of Royal Holloway College. Their interest and encouragement in various aspects of this work has been much appreciated. Thanks are also due to T C Hender, who generously made available the results of calculations from his heat conduction and resistive field diffusion code for used in chapter 6.

The provision of experimental and computing facilities, and of financial maintenance, by the UKAEA Culham Laboratory is acknowledged.

Table of Contents

CHAPTER 1 INTRODUCTION

It is without doubt true to say that much of the current interest in the study of plasma physics stems from the role of plasmas in controlled thermonuclear reaction (CTR) research. The much publicised aim of CTR research is of course the economic generation of useful power through the controlled release of energy associated with the fusion of light atomic nuclei. The term thermonuclear embodies the concept of reacting species deriving sufficient energy of activation for the fusion reaction from their thermal motions alone. Even with the most favourable combination of reacting nuclear fuels, that is deuterium and tritium in a straight D-T reaction, a minimum temperature in excess of 10 K is necessary to achieve an adequate reaction rate at realistic nuclei densities. At these temperatures matter adopts the plasma state. CTR research is currently addressing the problems of how best to provide an energy-efficient insulating confinement for such a plasma, and how to supply efficient heating to reach the required temperature for thermonuclear ignition.

Presumably 10^8 K.

After nearly thirty years of steady progress, conditions closest to those required for fusion power generation have been attained in toroidal magnetic confinement devices, where magnetic forces are used to isolate high temperature plasma from material walls. Outstanding amongst this general class of machines is the tokamak, in which charged particles are constrained to orbit along the helically twisted lines of force of a strong externally applied toroidal magnetic field. The principles of plasma confinement in toroidal devices are outlined in chapter 2. A more detailed review of plasma equilibrium and stability in the tokamak is given, and the importance of the magnetohydrodynamic safety factor in determining the upper limit of the plasma current for a given toroidal field strength is described. This stability criterion leads to a practical limitation on the plasma ohmic heating power density, and introduces the need for auxiliary plasma heating to ignition in

the tokamak. The suitability of radio-frequency heating, utilising wave absorption at the electron cyclotron resonance is discussed, and the proposed heating schemes are summarised. Interest in this mode of heating is being stimulated by the recent availability of high power microwave sources of appropriate frequency.

The increasing achievement of CTR experiments over the years (in terms of confined plasma density, temperature and lifetime) has been measured by a wide variety of diagnostic techniques. As temperatures have increased then the plasma x-ray emission (from bremsstrahlung, recombination and impurity line radiation) has become relatively more powerful, and so soft x-ray diagnostics have become increasingly important. Spectroscopic x-ray studies yield information on the spatial and charge-state distribution of impurity ions, and give a measure of the electron velocity distribution function, whilst the sensitivity of the emitted soft x-ray power to the plasma parameters of density, temperature and ionic composition means that spatially and time resolved x-ray flux monitors give a wealth of information on the equilibrium distribution of these quantities, and on their redistribution by instabilities and relaxation processes. The techniques of soft x-ray diagnostics, and important results, are reviewed under the broad division of spectroscopic, and of flux diagnostics in chapter 3. Methods of flux-signal analysis applicable to the particular diagnostic installed on TOSCA are developed.

The x-ray observations of electron cyclotron resonance heating reported in this work were recorded on the TOSCA tokamak. TOSCA is a small (R = 0.3 m, a = 0.1 m) air-cored tokamak whose research aims are the study of the effects of plasma cross-section shaping, compression and pressure upon confinement. Recent modifications to the machine, to permit the injection of high power (up to 200 kW) microwave beams from a gyrotron device, allow extension of the high pressure studies by using the additional heating effect of the RF power, and widen the research scope to include investigation of RF-induced toroidal

plasma currents, and through the localisation of the heating to the study of plasma heat conduction properties, and of current profile control. The basic machine and its sub-systems, including the gyrotron micro-wave generator and antenna, and principle diagnostics are fully described in chapter 4.

Auxiliary plasma heating experiments in TOSCA have been conducted, utilising the second harmonic of the electron cyclotron resonance. A characteristic feature of this heating is its localisation, due to spatial variation of the magnetic field strength in the tokamak major radius. The spatial resolution of the soft x-ray flux diagnostic installed on TOSCA is fully exploited in the study of the resulting heating effect. Reported in chapter 6 are the first results from such experiments anywhere in the world.

Calculations on the temperature dependence of the signal from the soft x-ray detectors employed on TOSCA, developed in chapter 3, are used to assist in the establishment, in chapter 5, of models of the spatial profiles of the local electron and ion temperatures. These models are developed in an attempt to simulate the physics and plasma profiles thought to be involved in the RF-heated discharge. A discussion of the experimental results in terms of the likely mode of action of electron cyclotron resonance heating in TOSCA is given in chapter 7.

CHAPTER 2 PLASMA CONFINEMENT AND HEATING IN TOROIDAL DEVICES

This chapter introduces the principles of plasma confinement in toroidal devices. A review of plasma equilibrium and stability in the tokamak is given, and it is shown how an important stability criterion leads to a practical limitation on the plasma ohmic heating power density. This in turn introduces the need for auxiliary plasma heating in order to achieve the ultimate aim of ignition conditions in the tokamak. The suitability of radio-frequency heating, utilising wave absorption at the electron cyclotron resonance is discussed, and the proposed heating schemes in the tokamak are summarised. The discussion is illustrated throughout with examples drawn from measurements made on, and from the proposed electron cyclotron resonance scheme for, the TOSCA tokamak.

2.1 TOKAMAK CONFINEMENT

Described by the ideal magnetohydrodynamic (MHD) model, the equation of motion of a plasma in a magnetic field may be written [1] (in SI units)

$$\rho \frac{\partial \underline{v}}{\partial t} + \rho \underline{v}.\nabla \underline{v} = \underline{j} \times \underline{B} - \nabla p \qquad 2.1$$

where ρ is the fluid mass density, $\underline{v}$ is the fluid velocity, $\underline{j}$ the current density, B the magnetic flux density and p the pressure. For a stationary plasma, this reduces to

$$\underline{j} \times \underline{B} = \nabla p \qquad 2.2$$

assuming that the plasma pressure may be represented by a scalar. From equation 2.2 it follows that

$$\underline{j}.\nabla p = 0 \quad ; \quad \underline{B}.\nabla p = 0 \qquad 2.3$$

In a closed system, the condition p = constant defines a closed surface. Since the pressure gradient will everywhere be normal to this surface, it follows from equation 2.2 that p = constant defines a magnetic surface of constant B. A theorem of topology [37,38] states that such surfaces confining

a closed volume of plasma must be toroidal surfaces. The simplest closed field-line system is then the toroidal pinch. The conventional coordinate system used to describe the toroidal pinch is shown in figure 2.1. Early experiments [39] found the toroidal pinch configuration to be highly unstable with respect to MHD instabilities. Stability was improved by the addition of a toroidal field B_ϕ, as in the well known Zeta device [40,41]. Russian workers found a further improvement in confinement and stability with the addition of a very strong toroidal field, such that $B_\phi \gg B_\theta$, a result confirmed by the diagnostic measurements of a group from the UK [42]. It is this system that came to be known as the tokamak, the term being a Russian acronym for toroidal magnetic chamber.

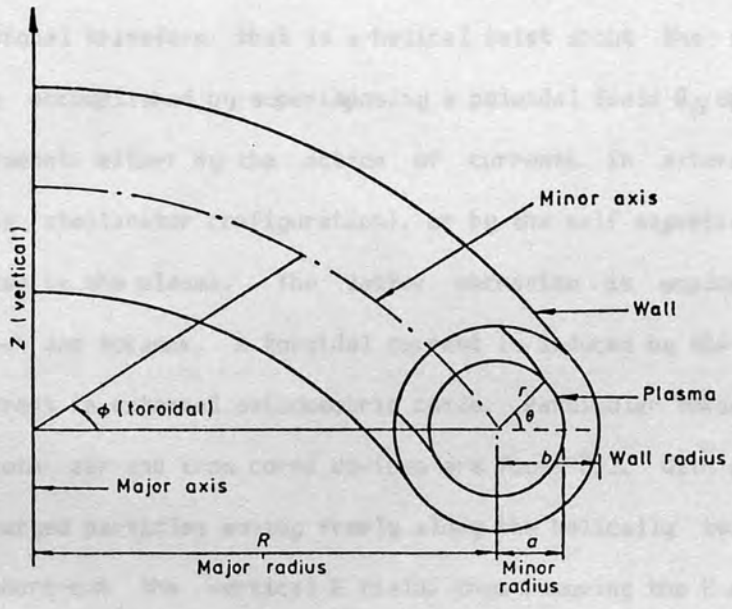

Figure 2.1

Toroidal coordinate system

2.1.1 TOKAMAK EQUILIBRIUM

The characteristic feature of the tokamak is the strong confining toroidal field. This field is generated by currents flowing in external coils, which encircle the torus in minor circumference. This configuration gives a field variation across the torus, given approximately by

$$B_\phi(R) \cong B_{\phi 0} \frac{Rp}{R} \qquad 2.4$$

where R_p is the major radius of the geometric axis of the plasma column. The field gradient ∇B is then directed radially inward, and this results in a vertical drift of charged particles, with electrons and ions drifting in opposite directions. The charge separation so produced gives rise to a vertical electric field E, such that a further drift motion arises. The drift velocity is [32]

$$\underline{v}_D = \frac{\underline{E} \times \underline{B}}{B^2} \qquad 2.5$$

and is directed outward in major radius for both electrons and ions. A simple toroidal field thus fails to provide a confining equilibrium for plasma particles. This radial drift can be avoided by giving the toroidal field lines a rotational transform, that is a helical twist about the minor axis. This may be accomplished by superimposing a poloidal field B_θ upon the main toroidal component, either by the action of currents in external helical windings (the stellarator configuration), or by the self magnetic field of a current induced in the plasma. The latter mechanism is employed in the toroidal pinch and tokamak. A toroidal current is induced by the transformer action of current in external axisymmetric coils. Particular tokamak designs vary, and both air and iron cored devices are found [6]. With a rotational transform, charged particles moving freely along the helically twisted field lines can short-out the vertical E field, thus removing the E driven $\underline{E} \times \underline{B}$ drift. The field components in the tokamak are illustrated by those of the TOSCA tokamak, in figure 2.2. The angular rotation of a field line per unit length in the toroidal direction is given by

$$i'(r) = \frac{B_\theta}{r} \cdot \frac{1}{B_\phi} \qquad 2.6$$

where r is the minor radius in the plasma. The rotational transform i, defined as the rotation about the minor axis per turn in the toroidal direction is then

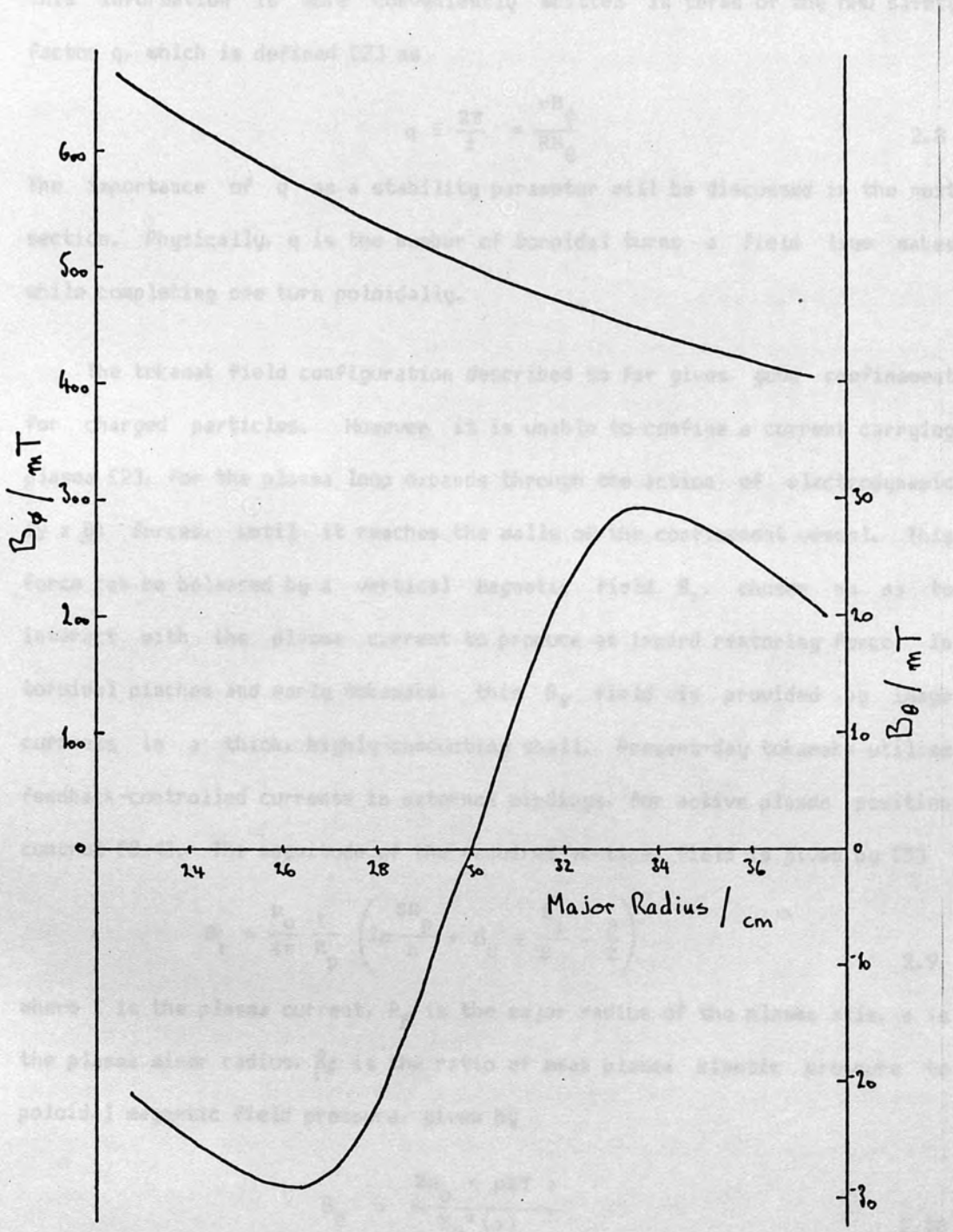

Figure 2.2

Field Distribution in a Tokamak

Showing vacuum toroidal field and calculated poloidal field

for a 7.9 kA discharge in TOSCA

$$i(r) = \frac{B_\theta}{r} \cdot \frac{2\pi R}{B_\phi} \qquad 2.7$$

This information is more conveniently written in terms of the MHD safety factor q, which is defined [2] as

$$q \equiv \frac{2\pi}{i} = \frac{rB_\phi}{RB_\theta} \qquad 2.8$$

The importance of q as a stability parameter will be discussed in the next section. Physically, q is the number of toroidal turns a field line makes while completing one turn poloidally.

The tokamak field configuration described so far gives good confinement for charged particles. However it is unable to confine a current carrying plasma [2], for the plasma loop expands through the action of electrodynamic ($\underline{v}$ x $\underline{B}$) forces, until it reaches the walls of the confinement vessel. This force can be balanced by a vertical magnetic field B_v, chosen so as to interact with the plasma current to produce an inward restoring force. In toroidal pinches and early tokamaks, this B_v field is provided by image currents in a thick, highly-conducting shell. Present-day tokamaks utilise feedback-controlled currents in external windings, for active plasma position control [3,4]. The magnitude of the required vertical field is given by [5]

$$B_r = \frac{\mu_o}{4\pi} \frac{I}{R_p} \left(\ell n \frac{8R_p}{a} + \beta_\theta + \frac{\ell_i}{2} - \frac{3}{2} \right) \qquad 2.9$$

where I is the plasma current, R_p is the major radius of the plasma axis, a is the plasma minor radius, β_θ is the ratio of mean plasma kinetic pressure to poloidal magnetic field pressure, given by

$$\beta_\theta = \frac{2\mu_o < nkT >}{B_\theta^2(a)} \qquad 2.10$$

and l_i is the internal inductance per unit length of the plasma, which depends upon the distribution of current density within the plasma cross-section. For a cylindrical plasma cross section

$$\ell_i = \frac{1}{\pi a^2 \, B_\theta^2(a)} \int B_\theta^2 \, dS \qquad 2.11$$

integrated over the cross-section. Theoretical calculations [43] indicate that β_θ, an important measure of the efficiency of utilisation of magnetic field energy, may have a limiting value, from equilibrium considerations [2], of order

$$\beta_\theta \lesssim R_p/a \qquad 2.12$$

This arises since as plasma pressure and β_θ increase, magnetic surfaces become increasingly distorted, ultimately breaking open with loss of equilibrium. Shaped cross-section tokamaks are an attempt to accommodate this distortion, and are seen as a means of obtaining higher mean values of β [6].

The vertical field also plays a role in providing a stable equilibrium in the vertical direction. In a purely vertical field the plasma torus would have neutral stability with respect to vertical motion. A positively stable arrangement is obtained by using a vertical field with outward convex field lines, thus introducing a nett radial field component to a vertically displaced plasma. The vertical field shape is described by the the decay index n:

$$n = -\frac{R}{B_r}\frac{\partial B_r}{\partial R} \qquad 2.13$$

the condition for vertical stability being that [5]

$$n > 0 \qquad 2.14$$

Under this condition the vertical field assumes some poloidal component. This poloidal field is generated by coils carrying current in the toroidal direction. In the presence of this shaped vertical field, stability with respect to horizontal displacement further requires that [5]

$$n < 3/2 \qquad 2.15$$

The presence of quadrupole (and higher order) poloidal fields is reflected in the plasma shape in minor cross-section. Stabilisation of shaped plasmas, produced in high β studies, to axisymmetric modes requires the use of a conducting shell, or feed-back control of the poloidal field [4]. Important unstable modes in this context are vertical displacement (m = 1) and

triangulation (m = 3) [33].

2.1.2 MHD STABILITY IN THE TOKAMAK

A plasma column is unstable to variety of motions. The normal modes of the system may be represented [7], in cylindrical geometry, by

$$\varepsilon = \varepsilon(r) \exp i(m\theta + kz) \qquad 2.16$$

where ε is the displacement, m is the mode number in the poloidal angle θ taking values 0,1,2,... , and k is the wave number in the z direction. The first three m-modes are illustrated in figure 2.3. The m = 0 mode is known as the sausage instability; a small reduction in plasma minor radius at any point results in an increase in the local B_θ field, thus driving the column to still smaller local radii. The m = 1 mode takes the form of a radial kinking of the plasma column. It is driven unstable by the difference in magnetic pressure across the radius of the kink. Higher m-modes result in a helical fluting of the plasma column surface, as illustrated in figure 2.3c.

Tokamak stability under ideal MHD can be analysed in a similar manner. Stability is determined by calculating the change in energy due to the perturbation of a normal mode, by expansion in the inverse aspect ratio [7]. The modes which are unstable in the highest order of inverse aspect ratio expansion, and which therefore potentially have the greatest growth rates, are the kink modes, also known as surface modes. For m > 1, these modes are stabilised by the local minimum B of the tokamak configuration [6], termed 'favourable magnetic curvature'. The m = 1 mode is stabilised in the tokamak by a periodicity constraint, that is by forcing the wavelength of the mode to be greater than the circumference of the machine. A mode grows about its so-called singular surface, where $\underline{k}.\underline{B} = 0$. For a plasma displacement of the form $\exp\{i(m\theta - n\phi)\}$ [7], where n is the toroidal mode number,

$$\underline{k}.\underline{B} = \frac{m}{r}B_\theta - \frac{n}{R}B_\phi \qquad \Rightarrow \frac{rB_\phi}{RB_\theta} = \frac{m}{n} = q(r) \qquad 2.17$$

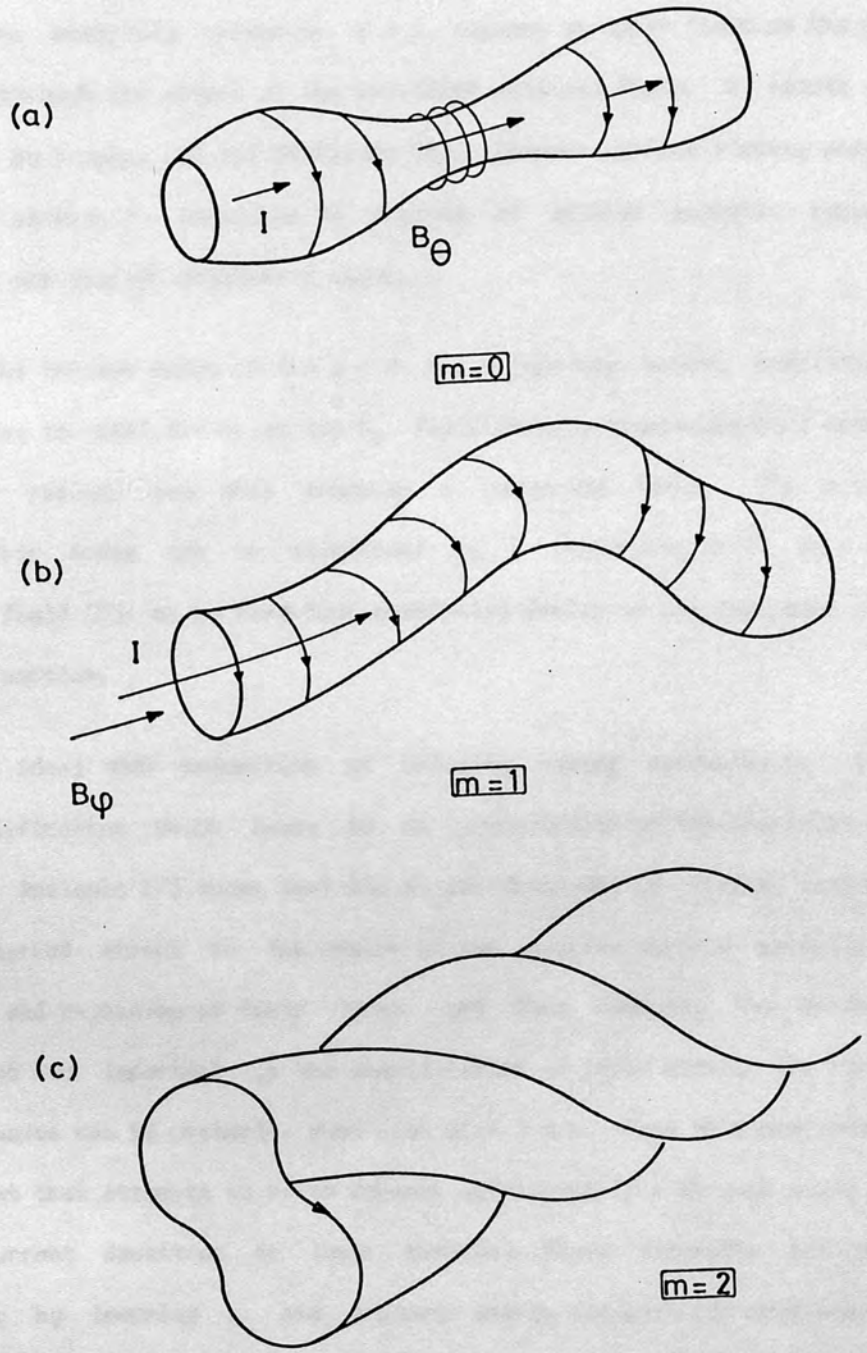

Figure 2.3

Ideal MHD modes in cylindrical geometry

Thus the condition $q(a) > m/n$ (where a is the minor radius) brings about stability by periodicity. If $q(r) < 1$ anywhere, then the $m = 1$ interchange or internal mode becomes strongly unstable, taking the form of an internal kink mode. The stability criterion $q > 1$ imposes an upper limit on the plasma current, through the effect of the resultant poloidal field, a result first obtained by Kruskal [8] and Shafranov [9]. However surface fluting modes can re-appear at high β, localised to regions of adverse magnetic curvature. These are the high-β ballooning modes.

In the tokamak modes of the $m = 0$, $n \neq 0$ type are easily stabilised by the strong toroidal field, as the B_ϕ field becomes compressed by a reduction in minor radius, and this produces a restoring force. The $n = 0$ or axisymmetric modes can be stabilised by a conducting shell, by a shaped vertical field [5], or by feed-back controlled fields as was described in the previous section.

The ideal MHD assumption of infinite plasma conductivity is an oversimplification which leads to an overestimate of the stability of the tokamak. Analysis [7] shows that the proper treatment of finite resistivity has a marked effect in the region of the singular surface, permitting the breaking and rejoining of field lines, and thus removing the periodicity constraint so important in the stabilisation of ideal modes. The resulting tearing modes can be unstable, even with $q(a) > m/n$. From this discussion it is evident that attempts to raise tokamak efficiency (β) through using either higher current densities or lower toroidal field strengths act against stability by lowering q, and a poorer energy and particle confinement may result. A feature common to many tokamaks when operated at low q ($q(a) < 3$) is the sawtooth oscillation. The sequence of events in this oscillation is thought to be as follows [46]. The maximum of the Ohmic heating power on the magnetic axis causes the electron temperature and current density to peak to the extent that the on-axis safety factor falls below unity. This

destabilises the m = 1 tearing mode which grows rapidly with the formation of a magnetic island, that is a current filament with m = 1, n = 1 symmetry. The island provides a route for the rapid transport of energy from the core region to the cooler edge of the plasma profile with the result that temperature and current density fall on axis. This forces q above unity, and the process is ready for another cycle. The cyclic repetition is clearly seen in the plasma soft x-ray emission, as illustrated in figure 3.25, which was recorded by the soft x-ray diagnositic on TOSCA. The lower trace is dominated by emission from the plasma core, and we see the slow rise in signal accompanying the Ohmic heating phase, followed by a sharp fall associated with the rapid growth of the tearing mode. The other signals represent the soft x-ray emission from plasma regions at progressively greater minor radii, and are inverted with respect to the signal from the core, reflecting the outward transport of energy during the sawtooth decay, with peaking of the profile under the effect of Ohmic heating.

2.1.3 ADDITIONAL PLASMA HEATING IN THE TOKAMAK

The combined effects of stability-limited plasma current, together with the adverse scaling of plasma resistivity with electron temperature [10], makes it unlikely that a purely Ohmically heated tokamak plasma will reach thermonuclear ignition temperatures at an acceptable capital cost. A guide to the achievement of a magnetic confinement system is the parameter β, as defined in equation 2.10 when evaluated with the total magnetic field strength, which is a measure of the efficiency of magnetic field utilisation. The on-axis β value achievable in an Ohmically heated tokamak appears to be well described by an empirical scaling law [11], and does not exceed about 1 % for tokamaks of a useful size. The maximum volume-average value of β (β^*) from Ohmic heating alone is even less [23]. To make a commercially attractive power generating tokamak system requires a β^* of 4-5 % [24]. The shortfall in β can be made up by auxiliary heating of the plasma by means other than

Ohmic. Very encouraging heating results have been obtained from the injection of energetic neutral atom beams [12] (NBI). Energetic neutral atoms penetrate the magnetic fields and collisionally heat the bulk plasma ions. This technique has achieved β^* values in excess of 3 % in the ISX B tokamak [28]. NBI is not the complete answer however. To heat the core region of the large tokamaks at present under construction requires beam energies in excess of 100 keV [24], and overall efficiency of the NBI system can then be quite low (2-3%). Improved efficiency is offered by various radio frequency heating schemes which exploit the natural plasma resonances, such as cyclotron, lower and upper hybrid. Experimental results in the field of RF heating have been reviewed by Riviere [13], and can generally said to be encouraging. The RF heating experiments described in this work consist of plasma heating utilising the electron cyclotron resonance. This technique will be discussed at greater length in section 2.2.

2.2 PLASMA HEATING AT THE ELECTRON CYCLOTRON RESONANCE (ECR)

Although the tokamak has proved to be the most succesful plasma confinement device to date, its ultimate success as a power generating reactor depends upon powerful supplementary plasma heating, as discussed in 2.1.3. Neutral beam injection and radio frequency resonance heating are both under intensive development to this end. Recent developments in the efficient generation of high frequency microwaves (described in section 2.2.2) now permit high power heating experiments of tokamak plasmas at the electron cyclotron frequency, and experimental work is now underway on a number of installations around the world. The important features offered by ECRH are:

i) plasma heating, although we note that there exists an intrinsic temperature dependent β -limit due to the density dependent plasma cut-off;

ii) plasma current drive [36], pursuing the goal of a DC tokamak;

iii) current profile control, utilising the localisation of heating, this in turn being a means of controlling the MHD stability of the plasma column.

2.2.1 ECR HEATING SCHEMES IN THE TOKAMAK

The cyclotron resonance condition between plasma electrons in the presence of a magnetic field B, and an electromagnetic (EM) wave of frequency ω is given by

$$\omega - k_{\parallel} v_{\parallel} = n\Omega_B \qquad 2.18$$

where Ω_B is the electron Larmor frequency, and $k_{\parallel}$ and $v_{\parallel}$ are the components of wave vector and electron velocity parallel to the field. Under these conditions energy is transferred from the EM wave field to the electrons. Because of the dominant toroidal field component in a tokamak, and its spatial variation across the torus, the spatial position of resonance with an externally launched EM wave is strongly localised in major radius. In a plasma with a distribution of electron velocities, the width of the resonance zone is determined by broadening through the relativistic dependence of electron mass upon its speed (which influences the Larmor frequency), and by broadening which results from the Doppler shift due to electron motion parallel to the field. Considering first the relativistic effect, for a maxwellian electron speed distribution of the form

$$f(v)dv \simeq A e^{-v^2/2v_{th}} v^2 dv \qquad 2.19$$

the broadening of the Larmor frequency, expressed as

$$\Omega = \Omega_0 \left(1 - \frac{v^2}{c^2}\right)^{1/2} \qquad 2.20$$

in a tokamak field distribution given by

$$B_\phi(x) = B_\phi/(1 + x/R_0) \qquad 2.21$$

where x is measured along the major radius from the magnetic axis, gives rise to a relativistic broadening of the resonance position of

$$\Delta x = 2\left(\frac{v_{th}}{c}\right)^2 R_0\left(1+\frac{x}{R_0}\right) \simeq 0.04 R_0 T_e\,(keV) \qquad 2.22$$

For TOSCA, taking the temperature at the resonant position to be 150 eV, this expression yields a value of 0.2 mm. Turning now to the Doppler effect, assuming a maxwellian distribution of velocities parallel to the external magnetic field

$$f(v_{\parallel})\,dv_{\parallel} \simeq A\,e^{-v_{\parallel}^2/2v_{th}}\,dv_{\parallel} \qquad 2.23$$

where $\Delta v_{\parallel} \sim 2\sqrt{2}\,v_{th}$, the Doppler term gives rise to a broadening of

$$\Delta x = 2\sqrt{2}\left(\frac{v_{th}}{c}\right) R_0 \cos\theta\left(1+\frac{x}{R_0}\right) \simeq 0.0012\cos\theta\, T_e^{1/2}(eV) \qquad 2.24$$

where theta is the angle between the wave vector and magnetic field. Substituting the appropriate values for TOSCA gives a result of 5 mm. The resonance zone width is thus much less than the plasma minor radius. It is this result that leads to the prediction of heating localised in plasma minor radius.

Since the ECR is spatially localised in the tokamak, it is necessary to determine its accessibility to externally launched waves by considering the propagation of the heating wave across gradients in magnetic field and electron density. For this purpose it is sufficient to use cold plasma theory, where for a tokamak heating arrangement of k perpendicular to B, two modes of propagation are identified [14]. These are the ordinary (O) mode whose electric field vector is parallel to the external field, and the extraordinary (X) mode, with E elliptically polarised in a plane perpendicular to B. The X-mode thus has an E component in the direction of propagation and is therefore partly transverse and partly longitudinal or electrostatic in character. The dispersion relationships for the two electromagnetic modes are

$$N_0 = \frac{c^2k^2}{\omega^2} = 1 - \frac{\omega_p^2}{\omega^2} \qquad 2.25$$

for the O-mode, and

$$N_X = 1 - \frac{\omega_p^2\left(\omega^2-\omega_p^2-\omega_{ci}\omega_{ce}\right)}{\left(\omega^2-\omega_{ce}^2\right)\left(\omega^2-\omega_{ci}^2\right)-\left(\omega^2-\omega_{ci}\omega_{te}\right)\omega_p^2} \qquad 2.26$$

for the X-mode, and are illustrated in figure 2.4 for typical tokamak fields and electron densities. The dispersion diagrams display discontinuities, i.e.

there exist regions of propagation, and regions where the wave is evanescent.

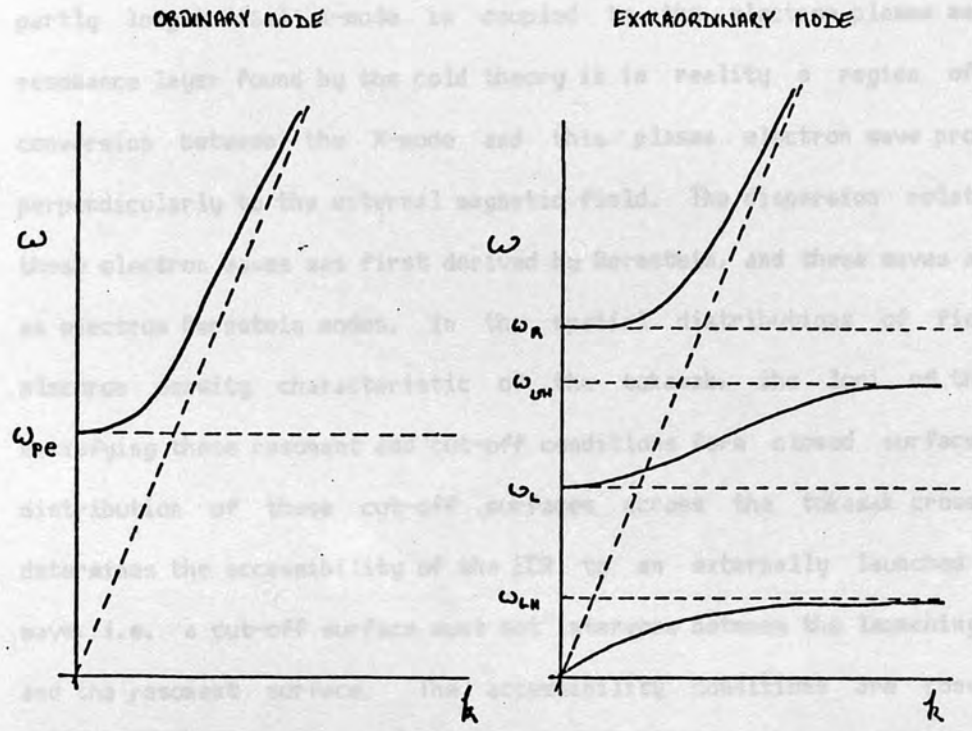

$$\omega_{pe} = \left(\frac{n_e e^2}{\varepsilon_0 m_e}\right)^{1/2}$$

$$\omega_R = \frac{\omega_{ce}}{2} + \left(\omega_{pe}^2 + \frac{\omega_{ce}^2}{4}\right)^{1/2}$$

$$\omega_L = \frac{-\omega_{ce}}{2} + \left(\omega_{pe}^2 + \frac{\omega_{ce}^2}{4}\right)^{1/2}$$

$$\omega_{UH} = \left(\omega_{pe}^2 + \omega_{ce}^2\right)^{1/2}$$

$$\omega_{LH} = \frac{\left(\omega_{pi}^2 + \omega_{ci}^2\right)^{1/2}}{\left\{1 + \frac{\left(\omega_{pi}^2 + \omega_{ci}^2\right)}{\omega_{ce}\,\omega_{ci}}\right\}}$$

Figure 2.4

Dispersion diagram for propagation of an electromagnetic wave perpendicular to a magnetic field for typical tokamak field strength and electron density.

Cold plasma theory is unable to interpret the resonance conditions where $N^2 \to \infty$. It contains no mechanism for wave energy transfer to the plasma. This situation is better described by warm plasma theory, where temperature effects are included in the fluid equations. Then, as the upper hybrid

resonance is appraoched, the transverse O-mode remains distinct whereas the partly longitudinal X-mode is coupled to the electron plasma wave. The resonance layer found by the cold theory is in reality a region of linear conversion between the X-mode and this plasma electron wave propagating perpendicularly to the external magnetic field. The dispersion relation for these electron waves was first derived by Bernstein, and these waves are known as electron Bernstein modes. In the spatial distributions of fields and electron density characteristic of the tokamak, the loci of the points satisfying these resonant and cut-off conditions form closed surfaces. The distribution of these cut-off surfaces across the tokamak cross-section determines the accessibility of the ECR to an externally launched heating wave, i.e. a cut-off surface must not intervene between the launching antenna and the resonant surface. The accessibility conditions are conveniently summarised by replotting on a Clemmov-Mullaly-Allis diagram, shown in figure 2.5.

The various ECRH schemes allowed in a tokamak have been reviewed by Fielding [15]. For large tokamaks the O-mode is utilised, since large absorption at the fundamental ECR permits the use of relatively efficient low frequency sources. The O-mode may also be launched from an antenna on the low-field outside of the torus, which is mechanically very convenient. The X-mode, when launched from the low-field side at fundamental ECR, immediately encounters the low-density cyclotron cut-off. These trajectories are marked O1 and X1 on figure 2.5. Further discussion of ECRH as applicable to large tokamaks [26,27] where there are higher field strengths, temperatures and densities is inappropriate in this work.

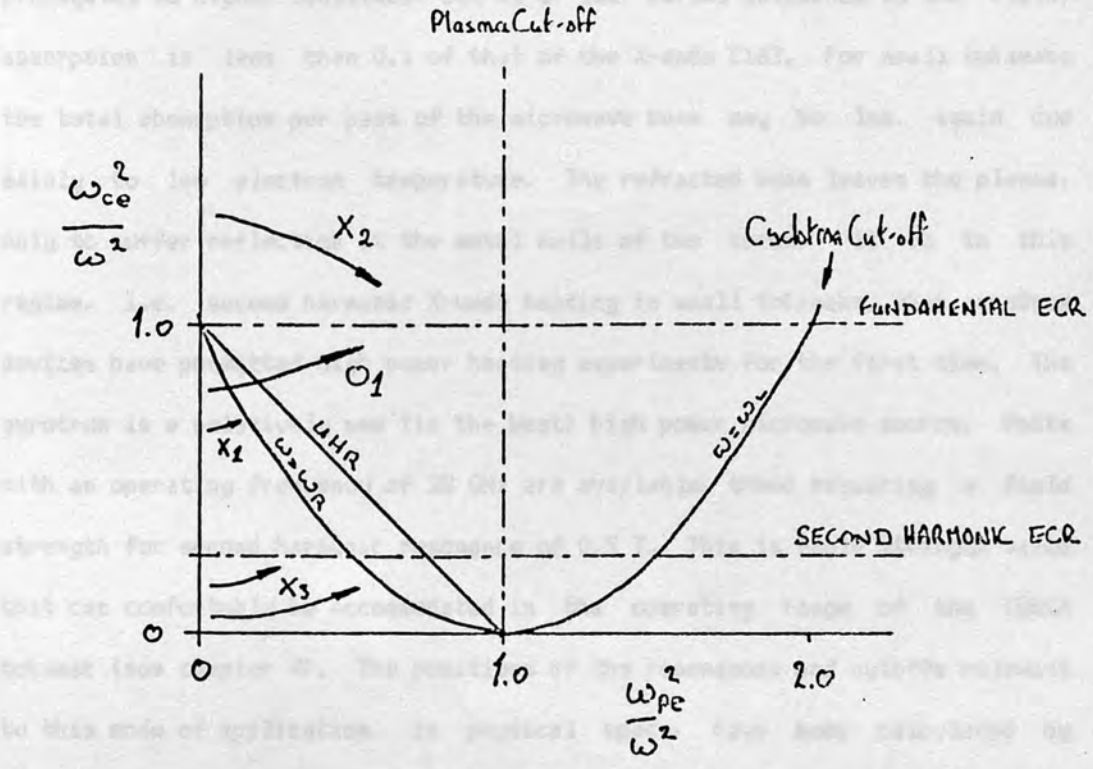

Figure 2.5

High-frequency part of the CMA diagram

In small tokamaks, the heating scheme must be modified since the plasma will generally be optically thin to the O-mode as a consequence of the dependence of the absorption coefficient on electron temperature. At the fundamental ECR, total X-mode absorption remains high due to the electrostatic nature of the wave, which permits linear mode conversion to longitudinal electron Bernstein waves [44,45] at the upper hybrid resonance layer [25]. The Bernstein waves propagate in a direction perpendicular to the field and are heavily cyclotron damped, so much so that runaway electrons may result. It is necessary however to launch the X-mode from the high-field side of the torus, i.e. along a path of the type marked X2 on the CMA diagram, to avoid the low density X-mode cut-off. Because of the (usually) lower fields employed on small tokamaks, heating at the second harmonic of the ECR becomes feasible. The X-mode is still absorbed and can be launched from the low-field side of the torus, along trajectories like X3 on the CMA diagram. The O-mode

propagates to higher densities, but at or near normal incidence to the field, absorption is less than 0.1 of that of the X-mode [16]. For small tokamaks the total absorption per pass of the microwave beam may be low, again due mainly to low electron temperature. The refracted beam leaves the plasma, only to suffer reflection at the metal walls of the torus. It is in this regime, i.e. second harmonic X-mode heating in small tokamaks, that gyrotron devices have permitted high power heating experiments for the first time. The gyrotron is a relatively new (in the West) high power microwave source. Units with an operating frequency of 28 GHz are available, these requiring a field strength for second harmonic resonance of 0.5 T. This is field strength value that can comfortably be accommodated in the operating range of the TOSCA tokamak (see chapter 4). The positions of the resonances and cutoffs relevant to this mode of application, in physical space, have been calculated by Lloyd [152] by assuming a parabolic electron density profile. An example is shown in figure 2.6. This figure illustrates the restrictive conditions imposed by operational density values, in that the low-density X-mode cutoff is present at large plasma radii. The heating profile under this condition has been calculated by Fielding [15], and is shown in figure 2.7. At low densities ($n_{eo} < 3.10^{18} m^{-3}$), below the X-mode cut-off, efficient heating peaked at the ECR is expected to occur. In the prevailing experimental regime of higher density operation ($n_{eo} > 7.5x10^{18} m^{-3}$) where the X-mode cut-off exists, a rapid transition to edge heating is predicted. In either case, the optical depth of the plasma remains substantially below unity, and Fielding concludes that the plasma is immersed in a radiation field which is quite insensitive to the detailed source and antenna characteristics.

One further accessibility condition may be present due to scattering of the heating waves by electron density fluctuations. Significant scattering losses have been predicted [35] for a reactor plasma with 1 % density fluctuations.

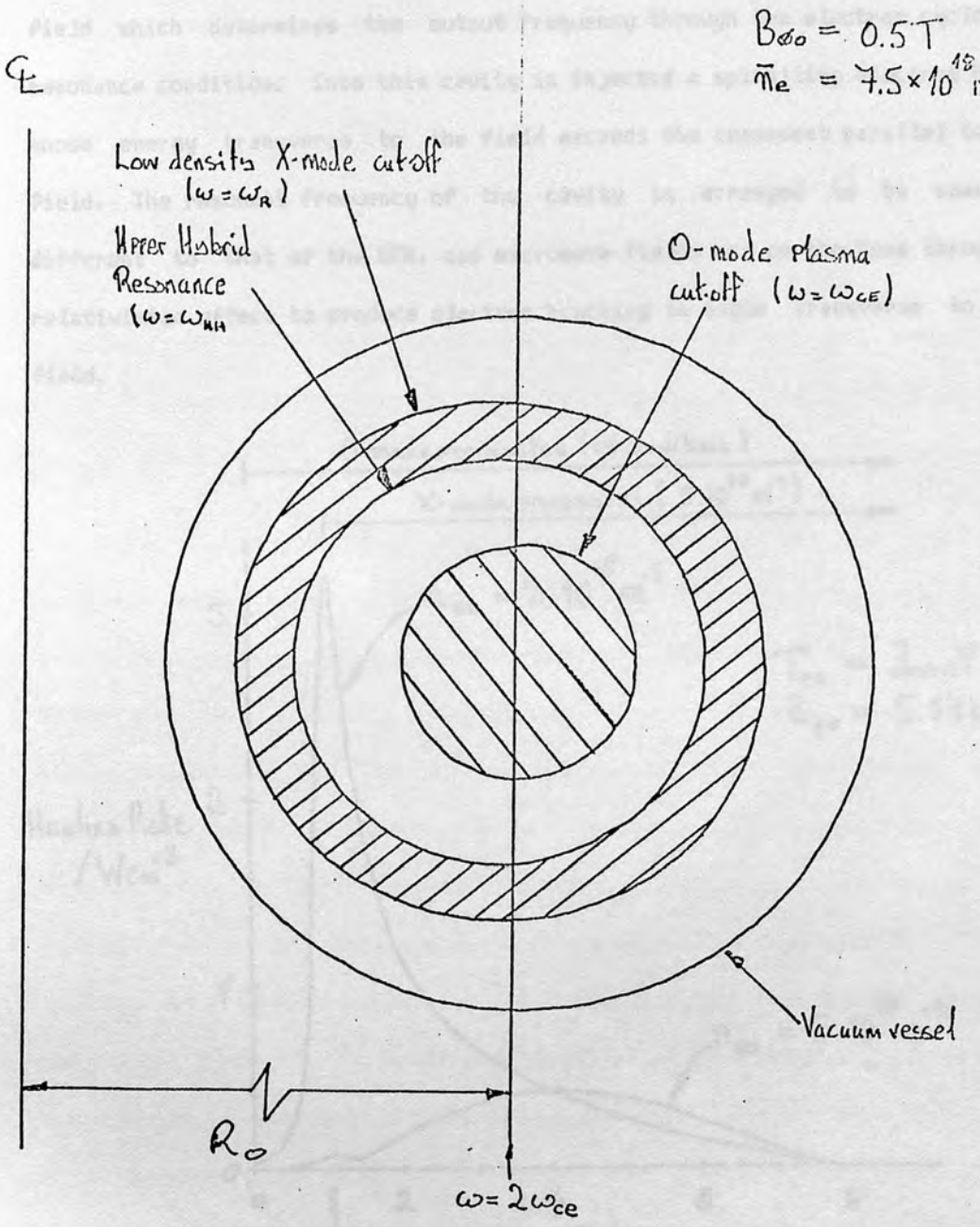

Figure 2.6

ECR accessibility conditions at the second harmonic in TOSCA

2.2.2 GYROTRON MICROWAVE SOURCES

It is the development of the gyrotron [17,18] microwave source that has permitted the study of efficient, high power ECRH in the tokamak. The device consists of a relatively large cavity, containing a longitudinal DC magnetic

field which determines the output frequency through the electron cyclotron resonance condition. Into this cavity is injected a spiralling electron beam, whose energy transverse to the field exceeds the component parallel to the field. The resonant frequency of the cavity is arranged to be somewhat different to that of the ECR, and microwave fields act on the beam through a relativistic effect to produce electron bunching in angle transverse to the field.

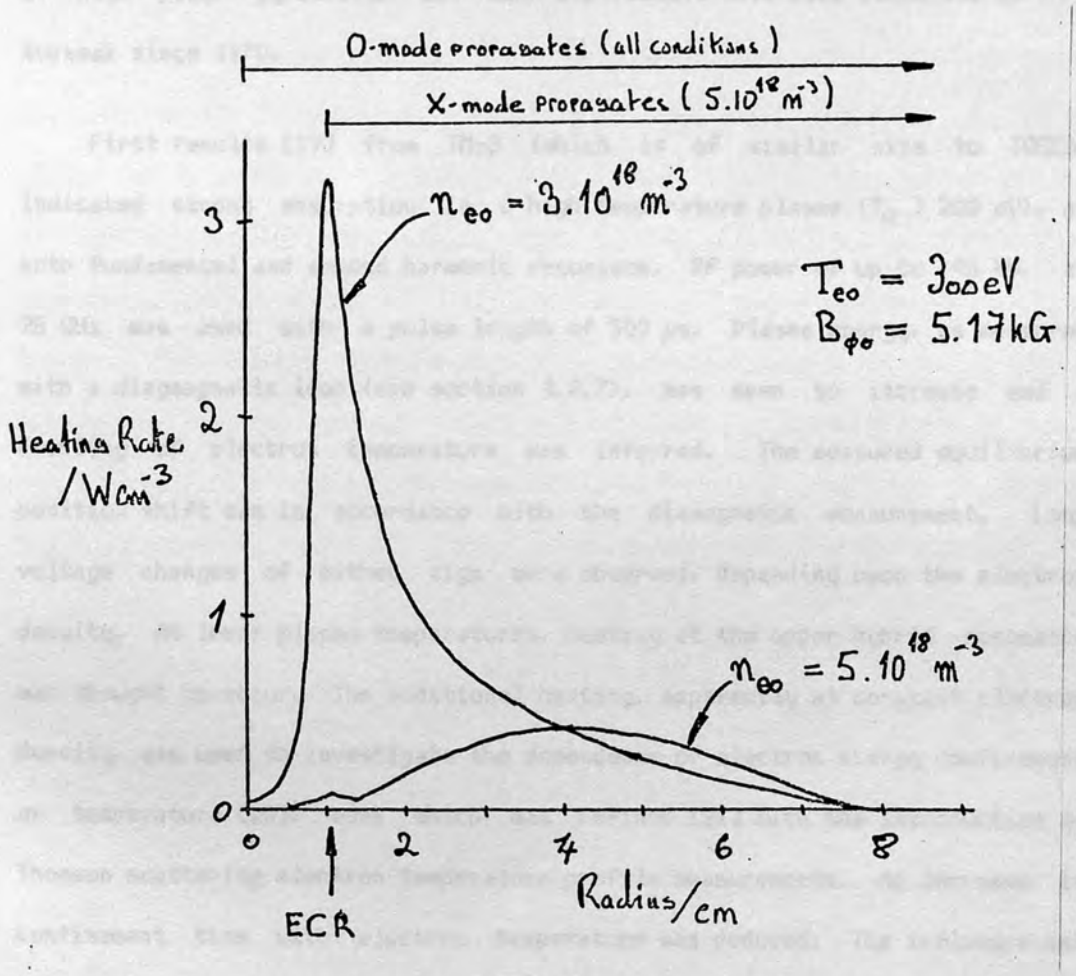

Figure 2.7

The calculated [15] ECRH heating rate profile for TOSCA

As the beam travels through the cavity, the phase between the electron bunches and the microwave electric field is adjusted in such a way that energy is transfered from the electron bunch transverse kinetic energy to the microwave field. The large electron beam amd microwave circuit dimensions allowed by this configuration permit higher power extraction for a given power loading

than was previously possible. The Varian gyrotron installed on TOSCA can produce 200 kW, 2 ms pulses, with a duty cycle of 1 %. Output wave frequency is 28 GHz.

2.2.3 REVIEW OF ECRH EXPERIMENTS

Much work has been done in the USSR, mainly due to the early availability of high power gyrotrons, and ECRH experiments have been conducted on TM-3 tokamak since 1970.

First results [19] from TM-3 (which is of similar size to TOSCA) indicated strong absorption in a high temperature plasma (T_e > 200 eV), at both fundamental and second harmonic resonance. RF power of up to 40 kW, at 28 GHz was used with a pulse length of 500 μs. Plasma energy, as measured with a diagmagnetic loop (see section 4.2.7), was seen to increase and a doubling of electron temperature was inferred. The measured equilibrium position shift was in accordance with the diamagnetic measurement. Loop voltage changes of either sign were observed, depending upon the electron density. At lower plasma temperatures, heating at the upper hybrid resonance was thought to occur. The additional heating, apparently at constant electron density, was used to investigate the dependence of electron energy confinement on temperature [20], work which was refined [21] with the introduction of Thomson scattering electron temperature profile measurements. An increase in confinement time with electron temperature was deduced. The influence and production of run-away electrons was investigated by measurements of the x-ray spectrum [22].

Soviet ECRH experiments have continued with work on the larger T-10 tokamak (R = 1.5 m, a = 0.36 m) [34]. Heating has been performed at the second harmonic ECR, using a 80 GHz gyrotron with RF power of 100 - 200 kW. The heating effect was observed in the soft x-ray intensity, diamagnetic loop signal, loop voltage, and in the high-Z (Z > 20) impurity charge state

population, which was seen to increase. The temporal evolution of the on-axis electron temperature was followed by soft x-ray spectral measurements (see 3.4.1), and an increase from 0.9 to 1.1 keV was observed with a 40 ms heating pulse. The Ohmic power in the discharge (700 - 750 kW) fell during RF heating by 60 - 70 kW due to the fall in loop voltage, so that total heating power was not greatly increased.

ECRH experiments have also been conducted on the ISX-B tokamak at Oak Ridge. Bulk population heating of the plasma electrons has been observed [29,31] while heating at the fundamental ECR (35 GHz), using RF powers of upto 80 kW. The heating waves were launched from the high-field side of the torus, into plasma with T_e of 1 keV on-axis. Predicted absorption per pass was 100 % for the X-mode, and approximately 50 % for the O-mode. The electron temperature evolution was monitored by Thomson scattering, second harmonic electron cyclotron emission (ECE), and by x-ray spectroscopy. The heating effect was found to be linear in RF power, with a heating rate of 6 eV/kW. Non-thermal electron behaviour was not observed.

The ISX group have also performed high-power pre-ionisation studies [30,31] with the gyrotron. The RF power established a cold (10 eV) plasma between the ECR and the upper hybrid resonance, prior to the induction of the plasma current. The technique reduced the initial loop voltage required for gas breakdown by 40 %, reduced initial poloidal flux consumption by 30 %, and permitted a faster rise of the toroidal plasma current. Pre-ionisation by using ECRH has thus the potential for aiding the controlled initiation of the plasma current, and reducing the poloidal field power supply requirements.

CHAPTER 3 SOFT X-RAY DIAGNOSTICS OF TOKAMAK PLASMAS

This chapter describes the status of soft x-ray diagnostics on the tokamak. The subject material is dealt with in four sections:

i) a description of the atomic processes responsible for soft x-ray emission from a plasma,

ii) a description of broad-band soft x-ray flux monitoring diagnostic techniques. This is a detailed section, and develops a full description of the diagnostic equipment used to make the measurements described in chapters 5 and 6 of this work,

iii) a review of the important results obtained from soft x-ray flux measurements on tokamak experiments,

iv) a review of soft x-ray spectroscopic measurements on tokamak experiments.

The readers attention is drawn to the important distinction here made between spectroscopic and flux diagnostics. In the former case the diagnostic instrument attempts to measure the energy of each incident photon. The flux diagnostic however is sensitive to a range of x-ray energies, but provides only a signal proprotional to the x-ray power deposited in the detector.

3.1 RADIATION FROM PLASMAS

The x-ray emission from a plasma consists of a continuum resulting from the free electron states, and of discrete line radiation corresponding to electron transitions between bound states. The two major contributors to the continuum emission are electron/ion bremsstrahlung, and free-bound radiative recombination radiation, where the emitted photon removes the electron kinetic and binding energy. A fourth process that may on occasion give rise to significant x-ray fluxes is that of dielectronic recombination. For the

electron temperatures and impurity species experienced in present-day tokamaks, the bulk of the radiation from these processes falls in the soft x-ray band, i.e. photon energies between 0.1 and 10 keV. These processes are discussed in greater detail below.

Free-Free Radiation

The spectral distribution of the bremsstrahlung radiation from a Maxwellian plasma is given by [89,90]:

$$E\frac{dn}{dE} = 9.6 \times 10^{-20}\, n_e \sum_i n_i\, Z_{iff}^2\, T_e^{-\frac{1}{2}}\, \bar{g}_{ff}\, \exp^{-E/T_e}\, m^{-3} s^{-1} \qquad 3.1$$

where Edn is the power emitted at photon energies in the range E to E+dE, with E expressed in electron volts. n_e and n_i are the electron and ion number densities in units of m^{-3}, Te is the electron temperature in eV, and Z_{iff} is the effective positive ion charge. The effective charge for a fully ionised atom is none other than the nuclear charge, but for partly stripped ions the effective charge is a function of the photon energy, ranging from the nett ion charge at low photon energies (distant electron-ion interactions) to the full nuclear charge at high photon energies, the latter case corresponding to close encounters with energetic electrons. An adequate theory of bremsstrahlung under these conditions is not available, and the exact value of the effective charge is not known for any particular case. The free-free Gaunt factor $\bar{g}_{ff}$ is averaged over the electron energy distribution. This has been calculated in references 91,92, and does not differ substantially from unity except for low-Z ions.

Free-Bound Radiation

The radiative recombination of an electron with an ion of charge state Z_i, ground state ionisation potential χ_i, ground state principal quantum number nq, and number density n_i, in a Maxwellian plasma, gives rise to a spectrum of the form [90]:

$$E\frac{dn}{dE} = 9.6 \times 10^{-20} n_e n_i Z_i^2 T_e^{-\frac{1}{2}} \bar{g}_{fb} \exp^{-E/T_e} \left[\frac{\varepsilon}{n_q^3} \frac{\chi_i}{T_e} \exp \frac{\chi_i}{T_e} + \sum_{\nu=1}^{\infty} \frac{2\chi_H Z_i^2}{T_e (n_q+\nu)^3} \exp \frac{\chi_H Z_i^2}{T_e (n_q+\nu)^2} \right] m^{-3} s^{-1} \qquad 3.2$$

The summation represents recombination to those states with higher principal quantum number. The first term in brackets is an approximation for recombination to the lower states of common ionisation potential χ_i, where $\mathcal{E}$ is the number of vacancies in the last unfilled electron shell, $\bar{g}_{ff}$ is the temperature averaged Gaunt factor, (usually close to unity [91]), and χ_H the ionisation potential of hydrogen. Other symbols are as defined in the previous section. Recombination power has a Z^4 dependence, and recombination radiation power from impurities in a hydrogen plasma may exceed that of the hydrogenic bremsstrahlung.

Line Radiation

Line radiation in the tokamak x-ray spectrum consists predominantly of K, L, and M shell radiation from high-Z (and therefore only partly ionised) impurities from the materials of the confining vacuum vessel, for example iron, molybdenum and tungsten. In lower temperature discharges line radiation from carbon and oxygen may be significant. The identification of observed spectral lines gives useful diagnostic information on the impurity content of the discharge. Transitions within a quantum level ($\triangle$n=0), although due to their high probability an important radiative energy loss mechanism, will occur naturally at very soft x-ray energies except for very high-Z elements. Theoretical predictions are most detailed for the K spectra (see for example reference 93), so experimental work has tended to concentrate on this area. Further details will be given in section 3.4, which deals with tokamak spectroscopy.

Dielectronic Recombination

In this process an electron from the continuum recombines with a partially ionised atom in a two stage process. First, the excess energy of the recombining electron is transfered to another electron on the partly stripped ion. Both electrons then decay radiatively to the ground state ion configuration [94,95]. These emitted photons tend to be of very low energy

and hence usually go undetected by the sort of x-ray diagnostic discussed in this work. However, dielectronic recombination can be an important power loss mechanism for plasmas with a particularly large content of high Z impurities, and is significant in those cases where the mean ionic charge exceeds about eight [96].

Total Radiated Power

In order to assess the importance of radiation in the power balance of a plasma system, the relative importance of the radiative processes must be determined. Appropriate calculations have been performed by most tokamak research groups. The results of one such calculation for an oxygen plasma in coronal equilibrium are shown in figure 3.1, which is taken from reference 97.

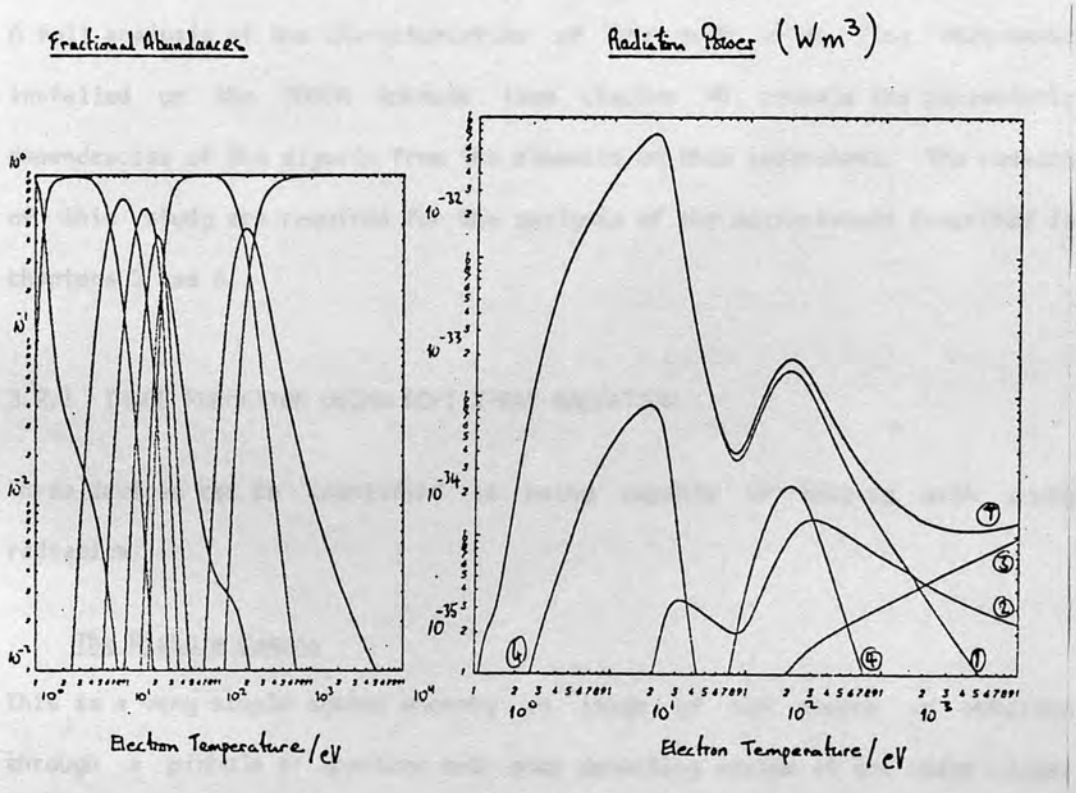

Figure 3.1

Ion fractional abundances (a) & Radiation power (b) from oxygen [97]

1) line radiation, 2) radiative recombination, 3) bremsstrahlung,

4) dielectronic recombination, T) total radiation power.

Figure 3.1a shows the fractional abundances of the nine charge states of the oxygen atom, figure 3.1b the radiated power due to each of the processes

described above, as a function of electron temperature.

3.2 PRINCIPLES OF SOFT X-RAY FLUX MEASUREMENTS

This section deals with soft x-ray flux measurements on the tokamak. For the purposes of this work, an x-ray flux diagnostic is defined as an instrument sensitive to a range of soft x-ray energies, whose output however reflects only the total x-ray power deposited in the sensitive area of the detector. The instrument does not attempt to measure the energy of each incident photon, has thus poor energy resolution, and is employed rather as an imaging device with good spatial and temporal resolution. Discussion topics are image formation, x-ray detectors, and signal analysis as apprpriate to the tokamak. A full analysis of the characteristics of the soft x-ray flux diagnostic installed on the TOSCA tokamak (see chapter 4) reveals the parameteric dependencies of the signals from the elements of this instrument. The results of this study are required for the analysis of the measurements described in chapters 5 and 6.

3.2.1 IMAGE FORMATION USING SOFT X-RAY RADIATION

Three devices can be identified as being capable of imaging with x-ray radiation:

The Pinhole Camera

This is a very simple system whereby an image of the source is obtained through a pinhole or aperture onto some detecting system at the image plane. The pinhole camera has been used for laser-produced plasma diagnostics [54,55], and is the basis of most tokamak soft x-ray flux diagnostics. The spatial resolution of the camera image is determined by the geometry of the camera apertures, the final design being a compromise between that image resolution required for an interesting physical measurement, and signal magnitude requirements, i.e. when used as a fast (80 kHz on TOSCA)

flux monitor, the need to generate a measurable signal in the poor electrical environment of the tokamak. This latter condition is to date always the most restrictive, and dictates that aperture dimensions exceeding a millimetre be used. On these grounds, the significance of the diffracting properties of the pinhole aperture to the soft x-ray radiation diminish to insignificance. For geometries with good spatial resolution and optically thin plasmas (to date always the case in the tokamak), the x-ray power incident upon a detector (and hence the detector signal) may be represented as an integral of the x-ray emission coefficient along the line of sight of the detector. An experimental set-up representative of that used on the tokamak is illustrated schematically in figure 3.2. The assumption is that with sufficiently high spatial resolution, variations in the emission coefficient of the plasma source visible to the detector transverse to the line of sight become very small. One need then only consider the variation of the emission coefficient along the line of sight. The x-ray pinhole camera has been developed into a powerful diagnostic on the tokamak. The analysis of the signals obtained from it is fully described in 3.2.3. The experimental results so far obtained are reviewed in 3.3. The instrument used on TOSCA to perform the measurements described in chapters 5 and 6 is described in chapter 4.

Grazing Incidence Reflection Microscope The GIR microscope [47,48] is capable of high resolution (3 um) for wavelengths greater than 3Å. At shorter wavelength the reflection efficiency drops rapidly. Incident x-rays are refracted by the crystalline structure of the focussing element. As the angle of refracton is a function of the x-ray wavelength, this device is not suitable for the imaging of a spatially extended polychromatic source such as a tokamak plasma. It finds however applications in x-ray astronomy.

Coded-Aperture Arrays, in particular the micro-Fresnel zone plate [49,50]. By interposing the Fresnel zone plate between the source and a photographic film, images of the x-ray emission are recorded. The resultant image can then be used to reconstruct (in first or higher [51] order) in the manner of a

hologram an image with both planar and in-depth resolution, i.e. the technique is tomographic, or more then two dimensional. Ceglio et al [49] have manufactured zone plates with up to 240 zones, with minimum zone widths (which relate to the spatial resolution obtained by defining the wavelength characteristic of the aparatus) in the range 2.6 - 10.2 μm.

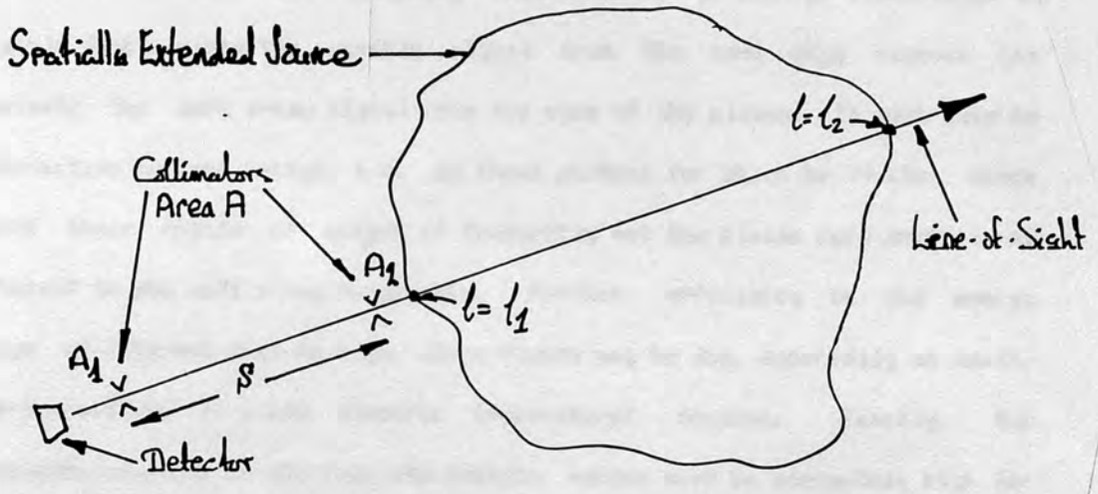

$$I_d \propto \frac{A_1 A_2}{4\pi S^2} \int_{l_1}^{l_2} \varepsilon(l)\, dl \qquad 3.1$$

Figure 3.3

Representation of the signal from an optically thin source as a line integral of the emmisivity in Wm-3

They have achieved a planar (i.e. transverse to the optical axis) resolution of a few microns, with an in-depth (i.e. perpendicular to the optical axis) resolution of 10 μm [52,53]. Optimal use of a zone-plate in this mode requires that the source to be imaged must be smaller than the diameter of the innermost zone. These features may be used to advantage in the diagnostics of laser produced plasmas. Current inertial-confinement fusion studies revolve around the interaction of very high power lasers with small targets containing deuterium and tritium fuel. Intense fluxes of x-rays are produced as the target material is heated and compressed. Zone plate cameras have recorded

high-resolution tomographic images of the thermal (2 - 6 keV) and supra-thermal (12 - 22 keV) emission from laser-compressed D/T filled targets.

3.2.2 X-RAY DETECTORS

For the study of the behaviour of the core region of a tokamak plasma the detector must meet the following requirements. It must be insensitive to visible light, since the visible signal from the cool edge regions can dominate the soft x-ray signal from the core of the plasma. It must also be insensitive to hard x-rays, i.e. to those photons for which $h\nu \gg kT_e$, since again their region of origin is frequently not the plasma core which is of interest to the soft x-ray diagnostic. Further, efficiency in the energy range of interest must be high, since fluxes may be low, especially on small, low-temperature ($\ll$ 1 keV electron temperature) devices. Finally, the frequency response of the complete detector system must be adequately high for MHD instability studies to be succesful. The soft x-ray flux diagnostic has produced some important results in this field, and these are reviewed later in this chapter. For example, the system installed on TOSCA (to be described in chapter 4) has been used to monitor MHD activity with characteristic frequencies of up to 80 kHz. This may be considered as rather restrictivly low for a small tokamak.

Solid state detectors can satisfy these conditions and in addition are relatively easy to use, with good availability in a range of physical shapes and sizes due to their widespread use for the detection of charged particles. The response to high energy photons may be selected by an appropriate choice of the detector thickness. Surface barrier diodes are most often used as they have a minimal non-detecting dead-layer between the energy-sensitive depletion region and the surface of the device. This has a significant effect on the low energy photon sensitivity of the diode (if this layer is too thick, low energy photons are completely absorbed before ever reaching the sensitive

depletion region), and is important in low-temperature plasma applications such as TOSCA. The question of sensitivity is dealt with further in section 3.2.3. The surface barrier diode works in the manner of any other semi-conductor detector. The metal contact establishes a Schottky [164] barrier junction. The depth of the associated depletion region is determined at the time of manufacture of the device by the thickness of the substrate material. Free charge carriers generated in this layer by the absorption of photons through the photoelectric effect (Compton scattering and pair production being unimportant at the low energies under discussion here) are swept out by the electric field of the junction, and appear as a current at the output of the device. In general, the output current is small (~1nA on TOSCA), and a current to voltage preamplifier is therefore required. The experimental arrangement used on TOSCA is described in section 4.2.2. Figure 3.3 gives a schematic view of the reverse-biased diode structure. Figure 3.4 gives a cross-section of the complete detector.

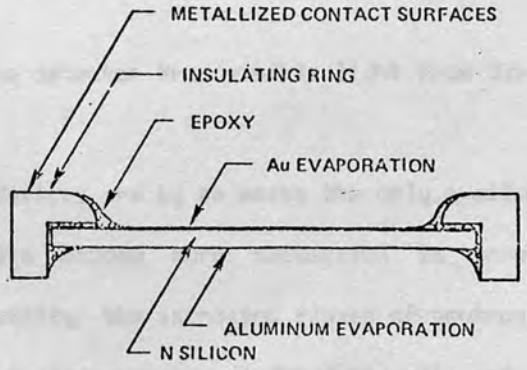

Figure 3.3

Schematic view of a reversed bias diode

The detector disc is packaged in a metal can, with a coaxial connector on the rear. Detectors of this type are used for flux measurements on all major tokamak experiments. In addition to the unavoidable metal contact on the front of the detector, thin layers of absorbers may be used to filter the x-ray spectrum received by the detector in order to:

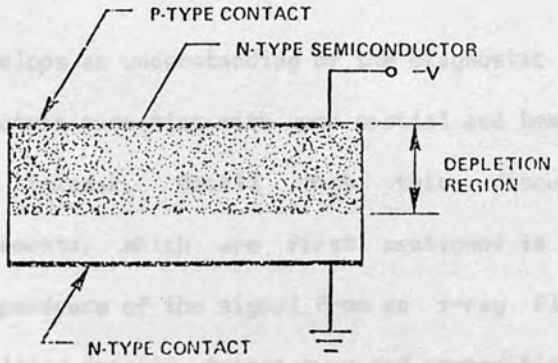

Figure 3.4

Cross-section of a surface barrier diode x-ray detector

- o modify the response of the detector to fluctuations in the plasma electron temperature [56], as discussed fully in the following section,
- o make a direct measurement of Te using two differently filtered detectors (discussed in section 3.3.3),
- o shield the detector from visible light from the plasma.

Solid state devices are by no means the only available detector systems. Indeed as tokamaks become more successful in terms of confined plasma temperature and density, the increased fluxes of neutrons and hard x-rays make the operation of surface-barrier diodes difficult, and alternative methods of x-ray detection become attractive. Scintillators used with photomultipliers, ionisation chambers, thermopiles, photoelectric and film detectors have all been considered for use in the JET experiment [56].

3.2.3 SOFT X-RAY FLUX MEASUREMENTS ON THE TOKAMAK

This section develops an understanding of the diagnostic information that soft x-ray flux detectors operating with good spatial and temporal resolution can provide on the tokamak. Recall that this discussion excludes spectroscopic measurements, which are first mentioned in section 3.4. An expression for the dependence of the signal from an x-ray flux detector is derived in terms of plasma density, temperature and composition. To solve the temperature dependent equation requires a detailed knowledge of the response of the detector to x-rays as a function of energy. The response function for the surface-barrier detectors and filters employed on TOSCA is calculated from tabulated data. Two models of the calculated response, one analytic, one numeric, are used to solve for the temperature dependence of the x-ray signal. A further numerical treatment is used to calculate the effect of the spatial distributions of electron density and temperature typical of the tokamak upon this result. Other data processing techniques applied in this field, though not used in this work, are reviewed toward the end of this section.

3.2.3.1 Parametric Dependence of Flux Signal

It has been shown in section 3.1 that the x-ray emission from a plasma is a function of several plasma variables. When studying a time varying plasma x-ray emission, then to changes in which variable does one attribute the observed behaviour? Developed here is a calculation of the relative influence of the primary plasma parameters (i.e. density, temperature and ionic composition) on the detected broad-band x-ray flux signal from the TOSCA diagnostic described in chapter 4.

It is necessary first to assess the effect of impurity ions in a tokamak hydrogen plasma. Following von Goeler [90], considering an ion of charge state Z_i, with unit Gaunt factors, and setting Ziff to the nuclear charge Zn, equation 3.2 may be rewritten as

$$\left(E\frac{dn}{dE}\right)_{RR} = (\gamma-1)\left(E\frac{dn}{dE}\right)_{B} \qquad 3.4$$

where:

$$(\gamma-1) = \left(\frac{Z_i}{Z_{iN}}\right)^2\left[\frac{\varepsilon}{n^3}\frac{\chi_i}{T_e}\exp\frac{\chi_i}{T_e} + \sum_{\nu=1}^{\infty}\frac{2\chi_H Z_i^2}{T_e(n+\nu)^3}\exp\frac{\chi_H Z_i^2}{T_e(n+\nu)^2}\right] \qquad 3.5$$

The enhancement of recombination radiation over bremsstrahlung is thus expressed in terms of a quantity (gamma) which can be calculated for each charge state of the ion. Considering the TOSCA tokamak in more detail, where the plasma comprises of hydrogen from the filling gas and oxygen as a dominant impurity from adsorbed water vapour, the factor by which the bremsstrahlung exceeds that of a hydrogenic plasma is (from equation 3.1)

$$\xi' = \frac{n_e}{n_e n_H}\sum_i n_i Z_i^2 \equiv Z_{eff} \qquad 3.6$$

where nH is the number density of hydrogen atoms, and Z_{eff} is the mean, or so-called effective, plasma ionic charge, an important measure of the purity of a tokamak plasma. Substituting relation 3.6 into equation 3.1 gives

$$\left(E\frac{dn}{dE}\right)_{TOTAL\ B} = 9.6 \times 10^{-20} n_e^2 Z_{eff} \bar{g}_{ff} T_e^{-\frac{1}{2}} \exp^{-E}/T_e \qquad 3.7$$

From equation 3.4, the total continuum radiation from oxygen in this plasma may be expressed as

$$\left(E\frac{dn}{dE}\right)_{TOTAL} = \gamma\left(E\frac{dn}{dE}\right)_{TOTAL\ B} \qquad 3.8$$

where gamma-effective is the weighted gamma-value over all contributing charge states of the oxygen ion:

$$\gamma_{EFF} = \frac{\sum_i \gamma_i n_i}{\sum_i n_i} \qquad 3.9$$

Considering now a surface barrier diode detector viewing an extended plasma as depicted in figure 3.2, the power received at the detector is calculated by integrating equation 3.8 over photon energy, and over the plasma volume visible to the detector. This is written as:

$$P \cong G\iint_0^{\infty} An_e^2 Z_{eff} T_e^{-\frac{1}{2}} \exp^{-E}/T_e f(E) r(E) dE d\ell \qquad 3.10$$

where the volume integral is reduced to a line integral, as explained in

section 3.2.1, G is the factor expressing the geometry of the x-ray camera (area of detector, area of collimating aperture) from relation 3.1, and A represents the collected constant terms of equations 3.7 and 3.8. The additional terms in this equation are now defined as f(E), the transmission function to x-rays of the materials between the plasma and the x-ray sensitive depletion region of the detector (taking values from zero for materials opaque to soft x-rays, to one for fully transparent materials), and r(E), which is similarly the response function of the detector, which takes values also in the range zero to unity. Details of f(E) and r(E) follow. The expression is integrated over the line of sight of the detector, and over photon energy E. The sensitivity of the signal to variations in the plasma parameters is investigated by writing

$$P = A\ G \int P'.d\ell \propto I_s \qquad 3.11$$

where I_s is the signal curent from a surface barrier detector (written as proportional to the x-ray power rececived by it), and P′ expresses the functional dependence of the emitted x-ray power on the plasma temperature, density and composition:

$$P' = n_e^2\ Z_{eff}\ F(T_e) \qquad 3.12$$

$$F(T_e) = \int T_e^{-\frac{1}{2}} \exp(^{-E}/_{T_e}) f(E) r(E) dE \qquad 3.13$$

For a homogeneous plasma where the line of sight integral of equation 3.12 reduces to P′ times a constant, analysis proceeds by taking the total differential of equation 3.12:

$$\delta I_s \propto \delta P' = \frac{\partial P'}{\partial n_e}\ \delta n_e + \frac{\partial P'}{\partial Z_{eff}}\ \delta Z_{eff} + \frac{\partial P'}{\partial F}\ \frac{\partial F}{\partial T_e}\ \delta T_e \qquad 3.14$$

which for finite differences becomes:

$$\frac{\Delta I_s}{I_s} \cong \frac{2\Delta n_e}{n_e} + \frac{\Delta Z_{eff}}{Z_{eff}} + \frac{T_e}{F}\ \frac{\partial F}{\partial T_e}\ \frac{\Delta T_e}{T_e} \qquad 3.15$$

From this expression it is seen that the signal is twice as sensitive to electron density changes as it is to Z-effective changes. The dependence on electron temperature is however not yet clear. Let gamma, a temperature sensitivity coefficient for the x-ray detector system, be defined as:

$$\gamma(T_e) = \frac{T_e}{F} \frac{\partial F}{\partial T_e} \qquad 3.16$$

Two approaches to the solution of equation 3.16 are presented below.

For the surface-barrier detectors in use on TOSCA, the response function of equation 3.10 may be considered to be uniform with photon energy up to some energy determined by the thickness of the depletion layer of the diode. This is written as

$$\begin{cases} r(E) = 1, & E < 10 \text{ keV} \\ r(E) = 0, & E > 10 \text{ keV} \end{cases} \qquad 3.17$$

The calculation is simplified by including the effect of the non-photon sensitive layers of the device (front electrical contact, dead layer) together with that of the filter material employed into f(E). Note that for central electron temperatures of 200 - 300 eV, the power emitted at photon energies greater than 10 keV forms a negligible fraction of the total power, as can be seen from equation 3.10. The transmission of soft x-rays through thin layers of absorbers is described by an exponential law:

$$I(x,E) = I_o(E)\exp[-\mu(E)x] \qquad 3.18$$

where I(x,E) is the flux at photon energy E in photons per second, after passing through a thickness x of absorber. $\mu(E)$ is the absorption coefficient, which is in general a very sensitive function of the photon energy. X-ray absorption has been measured by many groups for the materials and energy range of interest to this work. The results are usually presented in terms of the mass absorption coefficient, μ/ρ, where ρ is the density of the material. A comprehensive review of these data is given in reference 60. The transmission function of the absorbers may be calculated from published mass-absorption coefficient data [59,61,62]. For the apparatus on TOSCA, the combined filter transmission of the front contact of the surface barrier detector and additional visible filter have been thus calculated, and are plotted as the thick line in figure 3.5.

Analytic Solution

As a first approach to the solution of equation 3.16 for the case of a detector viewing a homogeneous plasma, we try to use an analytic model of the filter transmission function f(E) in order to obtain an analytic solution of equation 3.13. The model chosen is

$$\begin{cases} f(E) = 0, & E < E_o \\ f(E) = 1 - \exp -\lambda(E-E_o), & E > E_o \end{cases} \qquad 3.19$$

This function has two defining parameters, lamda and E0. It is chosen because values for the two paramters can be selected to give a reasonable fit to the calculated transmission below 1 keV. Three such models, characterised by the lamda values indicated in the figure, are also shown in figure 3.5. Then, substituting this analytic filter function model into 3.13, and solving,

$$F(T_e) = \int_{E_o}^{10\ keV} T_e^{-\frac{1}{2}} \exp^{-E/T_e}(1-\exp -\lambda(E-E_o))dE = \frac{\lambda T_e}{1+\lambda T_e}^{3/2} \exp^{-E_o/T_e} \qquad 3.20$$

and by substituting this result into 3.16 and solving, the coefficient of temperature sensitivity of the x-ray signal is obtained as

$$\gamma(T_e) = \frac{E_o}{T_e} + \frac{3}{2} - \frac{\lambda T_e}{1+\lambda T_e} \qquad 3.21$$

The reciprocal of gamma is plotted in figure 3.6. The lamda parameter values of the three lower curves in figure 3.6 correspond to the filter functions shown in figure 3.5. It is concluded from these curves that the coefficient gamma is rather insensitive to the precise form of the filter model. In some experiments we observe very large changes (>50%) in the x-ray signal. The differential formulation of equation 3.14 is then inapplicable, and to analyse these events in terms of a change in electron temperature a calculation of the power equation 3.10 is necessary. F(Te) is therefore plotted, as given by equation 3.20, in figure 3.7.

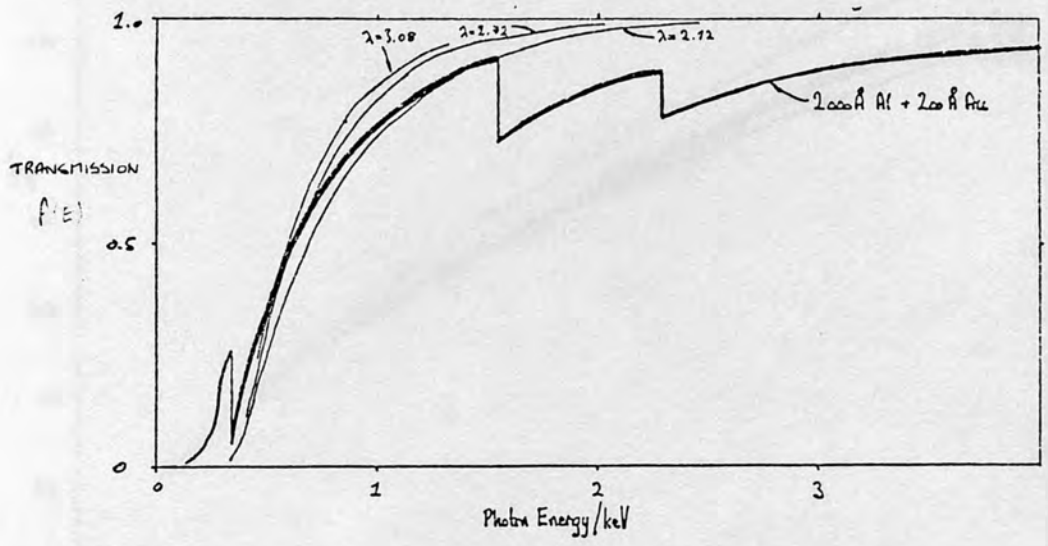

Figure 3.5

Calculated (thick line) and three modelled (defined by equation 3.19 and the indicated lamda values) transmissions of the soft x-ray filtering materials of the TOSCA diagnostic, consisting of 2000 A aluminium visible light filter, and a 200 A gold electrode Absorption coefficient data is taken from references 59, 61, 62.

Numerical Solution

Equation 3.16 was also solved computationally. The program was given the filter function (displayed in figure 3.8) calculated from the published mass-absorption coefficient data. This differs from the calculated filter function of figure 3.5 in that the effect of the small silicon dead layer of the surface barrier device has been included. F(Te) was then evaluated in 1 eV steps by numerical integration of equation 3.13, and is plotted in figure 3.10. From this result, the temperature sensitivity coefficient (equation 3.16) was calculated by numerical differentiation, and is shown in figure 3.9. Figure 3.10 displays F(Te) and therefore shows the temperature dependence of the signal Is (from equations 3.11, 3.12).

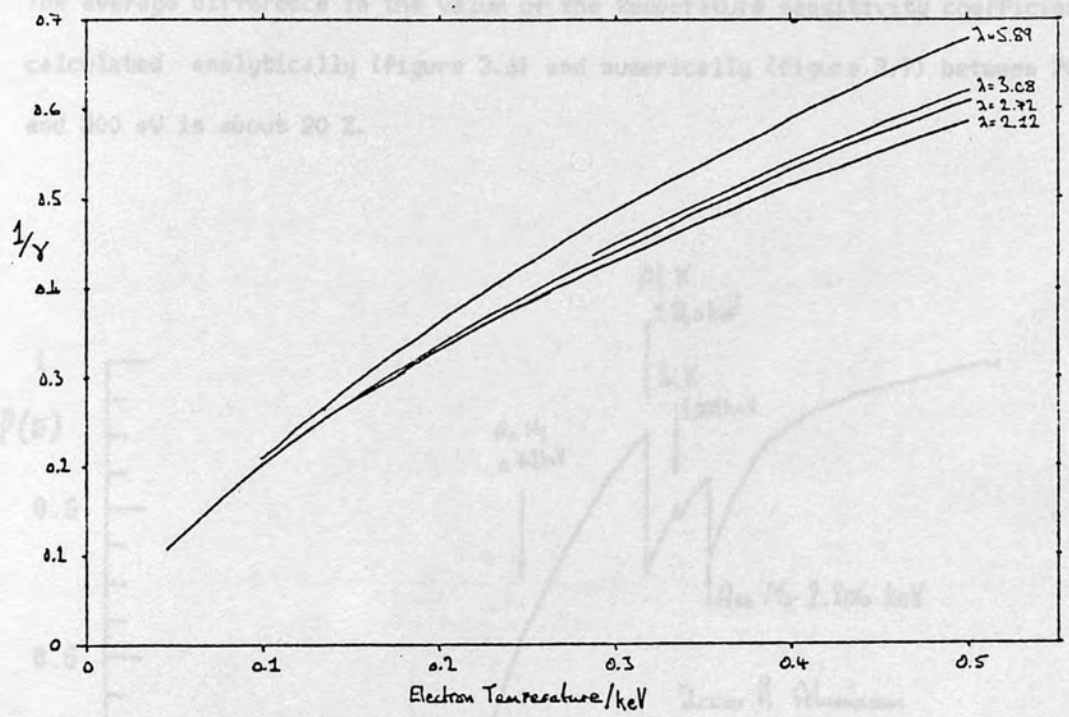

Figure 3.6

Reciprocal of the temperature sensitivity of the TOSCA soft x-ray diagnostic, as calculated from the analytic model of the filter function

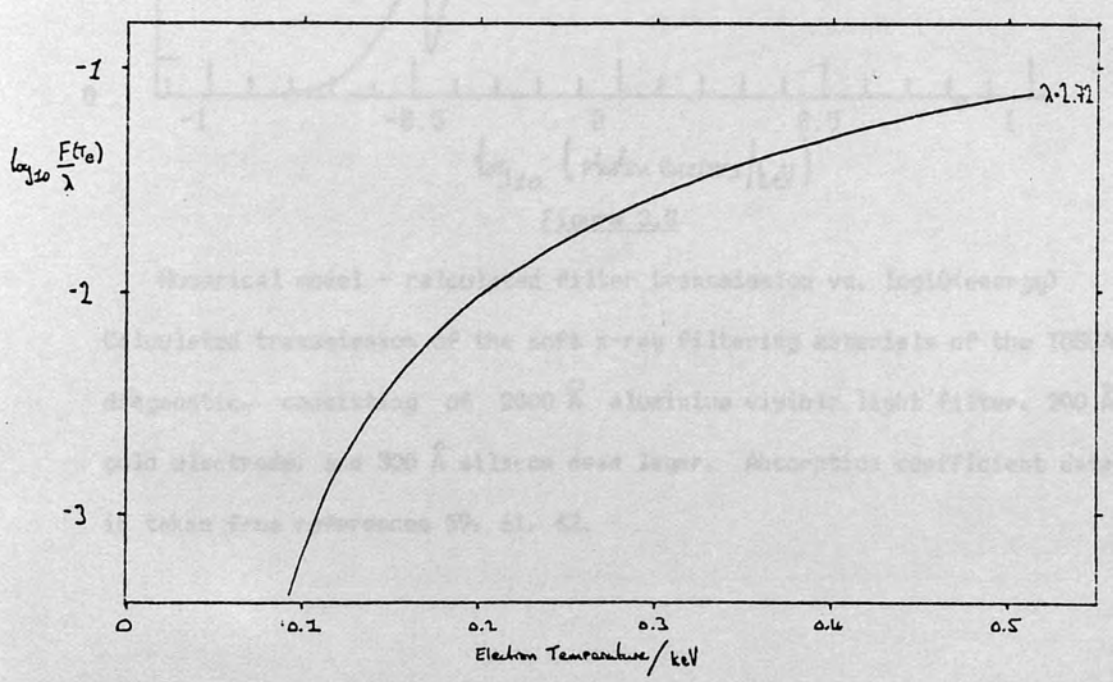

Figure 3.7

X-ray signal dependence on temperature calculated from analytic model

The average difference in the value of the temperature sensitivity coefficient calculated analytically (figure 3.6) and numerically (figure 3.9) between 200 and 300 eV is about 20 %.

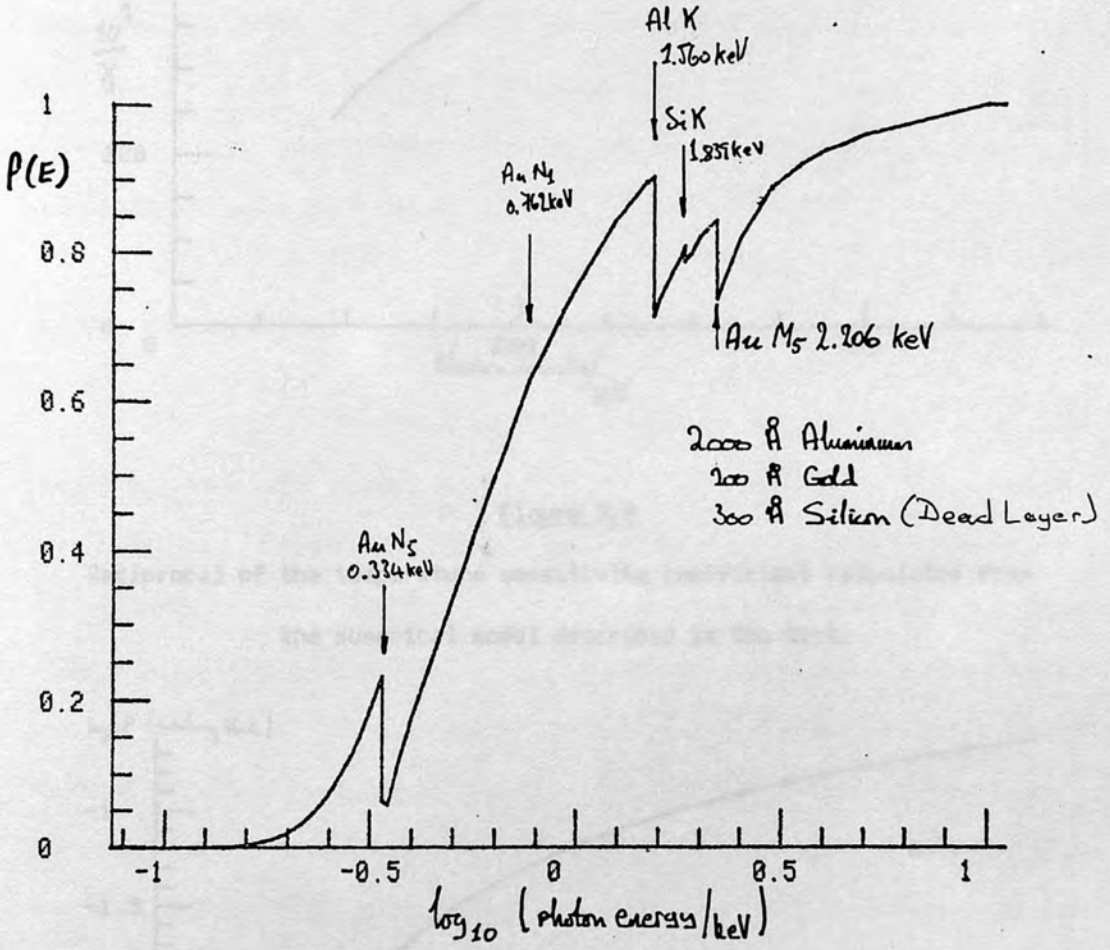

Figure 3.8

Numerical model - calculated filter transmission vs. log10(energy)

Calculated transmission of the soft x-ray filtering materials of the TOSCA diagnostic, consisting of 2000 Å aluminium visible light filter, 200 Å gold electrode, and 300 Å silicon dead layer. Absorption coefficient data is taken from references 59, 61, 62.

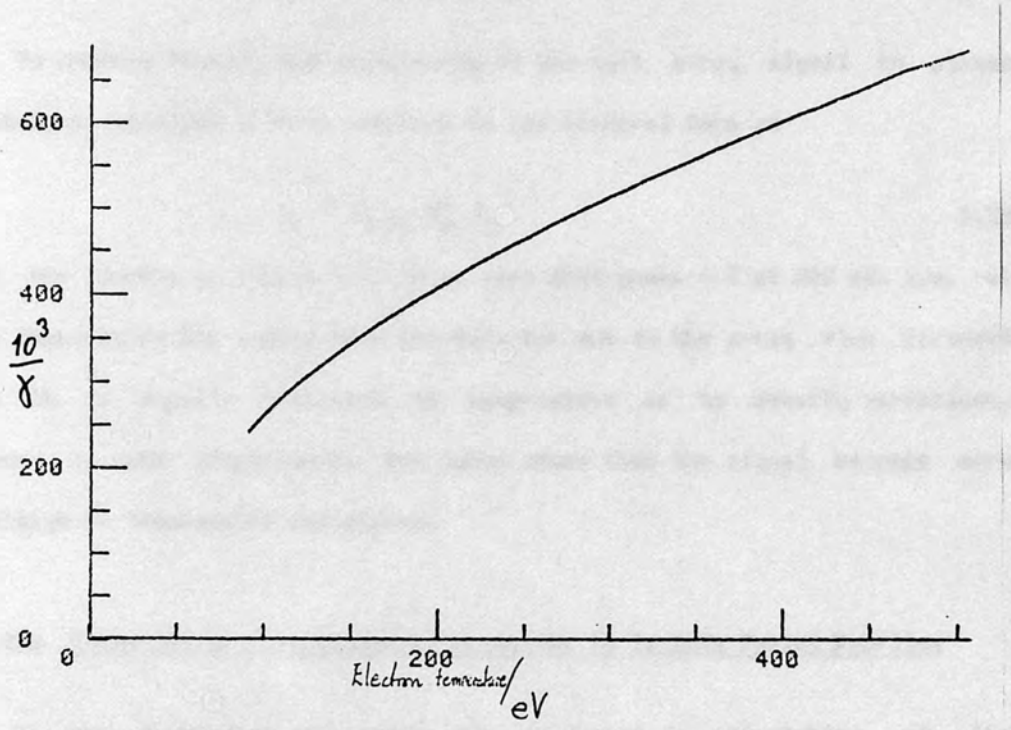

Figure 3.9

Reciprocal of the temperature sensitivity coefficient calculated from the numerical model described in the text.

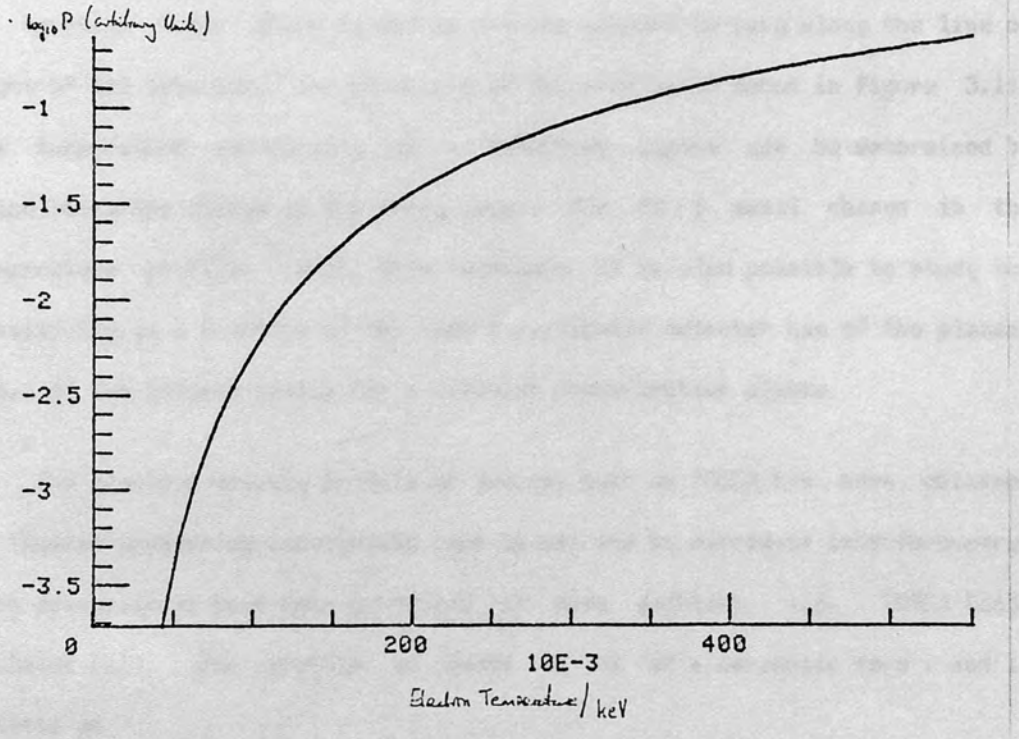

Figure 3.10

Power function vs electron temperature calculated from numerical model

To compare finally the sensitivity of the soft x-ray signal to plasma parameters, equation 3.14 is returned to its integral form as

$$I_s \propto Z_{eff} . n_e^2 . T_e^{\gamma} \qquad 3.22$$

From the curves of figure 3.9, it is seen that gamma = 2 at 300 eV, i.e. at this temperature the signal from the detector due to the x-ray flux incident upon it is equally sensitive to temperature as to density variations. However, at lower temperatures, the curve shows that the signal becomes more sensitive to temperature variations.

3.2.3.2 Extension of Sensitivity Calculations to Include Radial Profiles

In the preceeding paragraph was developed a calculation of the sensitivity of the signal from a soft x-ray detector to changes in the parameters of a homogeneous plasma. Included in the following paragraphs are the effects of the radial profiles of temperature and density characteristic of toroidal confinement systems. This is achieved by the numerical evaluation of equation 3.10, where Te and ne are now allowed to vary along the line of sight of the detector. The structure of the problem is shown in figure 3.11. The temperature sensitivity of a detecting system can be determined by calculating the change in the x-ray signal due to a small change in the temperature profile. With this technique, it is also possible to study the sensitivity as a function of the view a particular detector has of the plasma, i.e. of the tangent radius for a circular cross-section plasma.

The electron density profile of devices such as TOSCA has been obtained by Thomson scattering experiments (see below) and by microwave interferometry. Such measurements have been performed on many machines, e.g. TOSCA [66], PULSATOR [67]. The profile is found to be of a parabolic form , and is written as

$$n_e(r) = n_{eo}(1 - r^2/a^2) \qquad 3.25$$

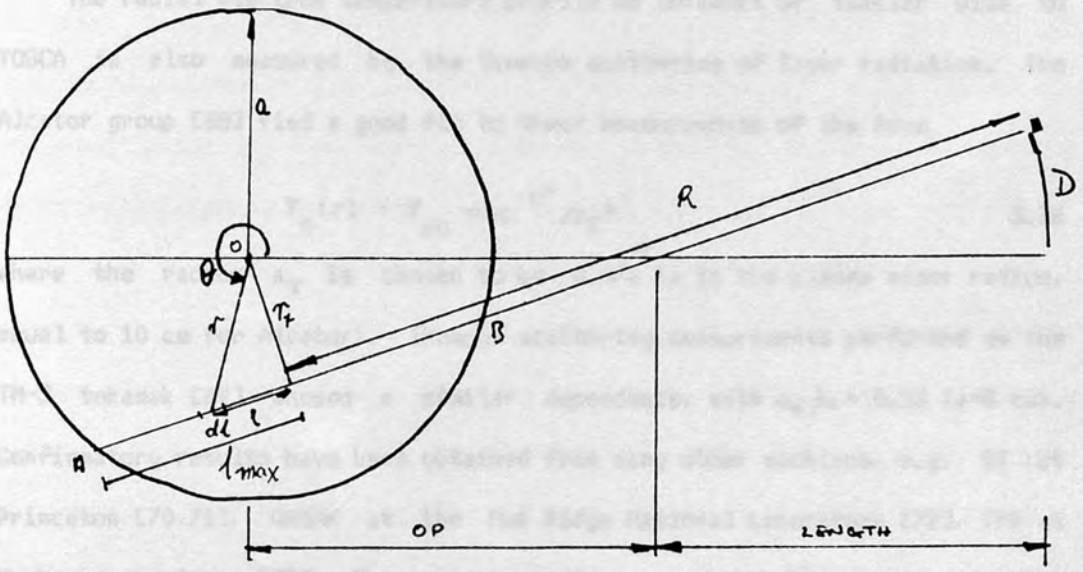

D - detector position in array module.

LENGTH - size of array module.

OP - distance from axis of plasma to entrance aperature of detector arrays.

AB - the line-of-sight chord of a detector.

r_t - chord tangent radius. $f(D, \text{LENGTH}, OP)$

a - plasma minor radius

l_{max} - chord half-length. $f(r_t, a)$

$$I_d(r_t/a) \propto \int_{-l_m}^{l_m}\int_0^{\infty} n_e^2(r,\theta)\, T_e(r,\theta)^{-1/2}\, \frac{\exp\left[-E/T_e(r,\theta)\right]}{(R-l)^2}\, F(E)\, r(E)\, dE\, dl$$

$$r = r(r_t, l) \qquad \theta = \theta(r_t, l)$$

$r(E)$ is the detector response

$F(E)$ is the filter transmission

Figure 3.11

Calculation of the x-ray signal from a surface barrier detector

where r is the distance from the plasma minor axis, and a is the plasma minor radius.

The radial electron temperature profile on tokamaks of similar size to TOSCA is also measured by the Thomson scattering of laser radiation. The Alcator group [68] find a good fit to their measurements of the form

$$T_e(r) = T_{eo} \exp^{-r^2}/a_T^2 \qquad 3.26$$

where the radius a_T is chosen to be 0.47a (a is the plasma minor radius, equal to 10 cm for Alcator). Thomson scattering measurements performed on the TM-3 tokamak [69] showed a similar dependence, with $a_T/a = 0.53$ (a=8 cm). Confirmatory results have been obtained from many other machines, e.g. ST at Princeton [70,71], ORMAK at the Oak Ridge National Laboratory [72], TFR at Fontenay-aux-Roses [73]. Measurements on larger machines have yielded results that are not dissimilar. See for example the results from the PLT tokamak at Princeton, where the temperature profile has been deduced from Thomson scattering [74], and from x-ray energy pulse height analysis measurements [61]. For TOSCA, a value for the temperature radius a_T of 0.5a is chosen, this being the value measured on the most similar machine. Three other temperature profiles are included for study in these calculations. These are:

$$\text{linear:} \quad T_e(r) = T_{eo}(1-r/a) \qquad 3.27$$

a tokamak profile recommended by the Culham DITE group, and;

$$\text{parabolic:} \quad T_e(r) = T_{eo}(1-r^2/a^2) \qquad 3.28$$

$$\text{flat:} \quad T_e(r) = T_{eo} \qquad 3.29$$

The latter two are not tokamak-like profiles, but are included for comparison, and may additionally have some relevence to the profiles found in reverse field pinch experiments.

Figure 3.12 shows the resulting calculated temperature sensitivity of the signal from the TOSCA soft x-ray flux diagnostic for the three profiles given above, together with that calculated for the homogeneous (flat) profile, for a detector viewing the plasma axis of the system. It can be seen that the sensitivity increases with the steepness of the profile. This is to be expected since as the profile gradient increases, the detector views a relatively larger volume of plasma whose temperature is less than that of the core. As was seen in the homogenous case calculations, the signal is more sensitive at low temperatures, so the inclusion of this low temperature region raises the mean sensitivity along any particular chord. Figure 3.13 shows a plot of the temperature dependence of the power received by a detector (in arbitrary units, as details of the detector and aperture geometry need not be introduced here) as a function of the central electron temperature for all four profiles.

Figure 3.14 shows the temperature sensitivity of the soft x-ray signal of four different chords through a circular cross-section plasma with a gaussian temperature profile. The effects of profile shape and central temperature can be seen here. As the line of sight moves off axis, then the maximum temperature along that line falls leading to enhanced sensitivity. This new higher sensitivity could be read from the on-axis curve were it not for the fact that the effective profile along the line of sight broadens as we move off axis. It was shown previously that broadening the temperature profile acts on the sensitivity in the opposite direction to the reduction of chord-maximum temperature, so the change is less than that calculated in terms of Te alone.

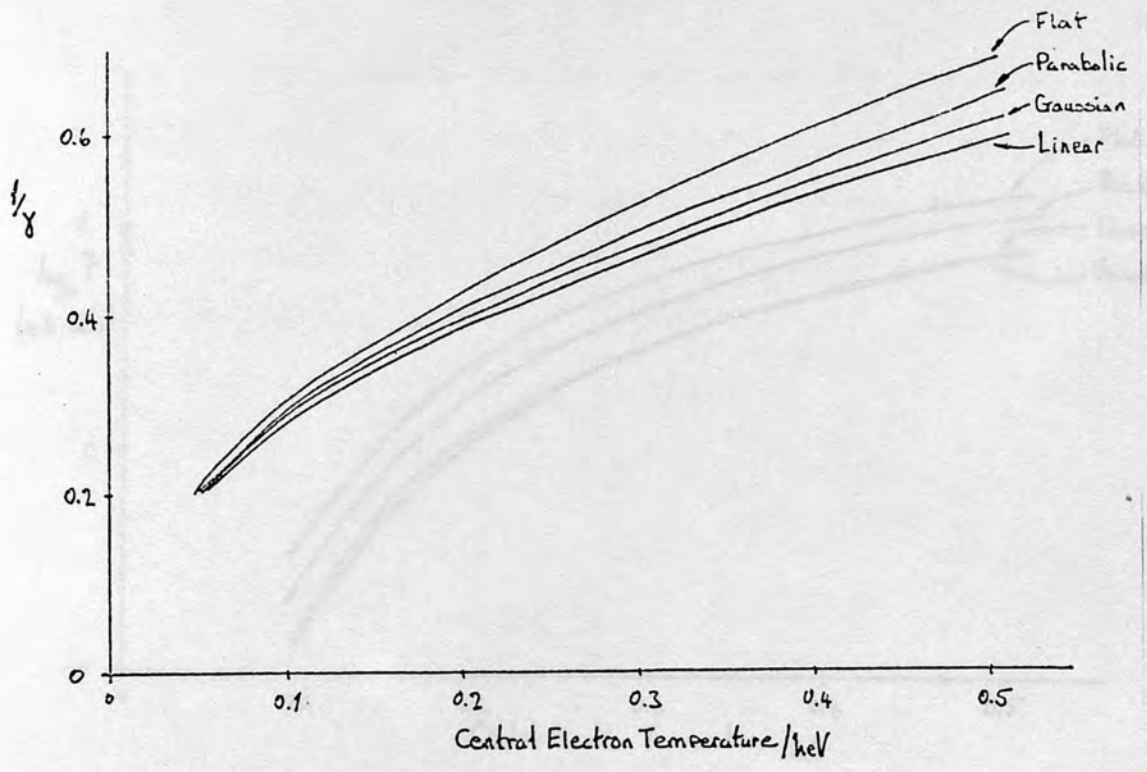

Figure 3.12

Reciprocal of the temperature sensitivity coefficient of the TOSCA soft x-ray diagnostic to four different plasma electron temperature profiles for a detector viewing the plasma axis

3.2.3.3 Form of the Emission Profile

The results of the calculations described in the previous section also give the form of the radial x-ray emission profile to be expected from a given distribution of plasma electron temperature and density. For a given plasma temperature profile, the dependence on on-axis temperature, of the x-ray emission profile shape might from inspection of the dominant term of equation 3.10 be expected to be of the form:

$$R = (\exp^{-E}/T_{o}\ \ )/(\exp^{-E}/T_{1}\ \ ) \qquad 3.30$$

where R is the ratio of the soft x-ray signal from a detector viewing the plasma axis where T = T0 to that of a detector viewing at a tangent radius r=r′ where T = T1, some fraction of T0. Then from equation 3.30

$$R = \exp \frac{\alpha E}{T_o} \qquad 3.31$$

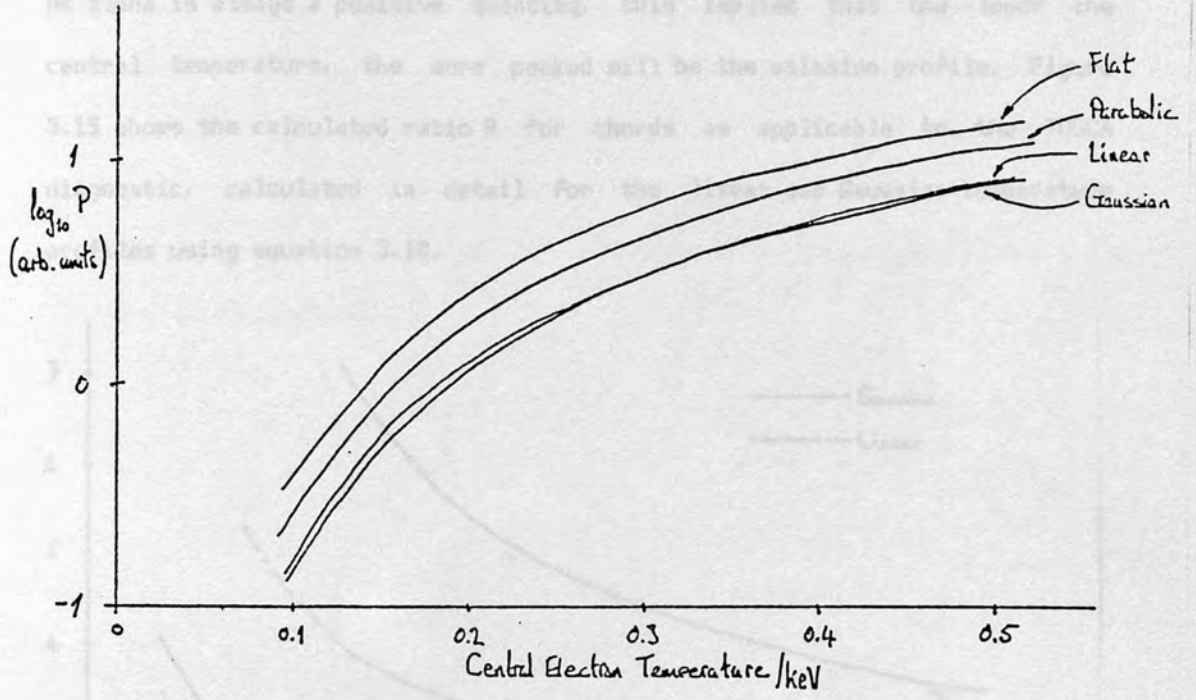

Figure 3.13

Soft x-ray power received by the sensitive region of a detector for four different plasma electron temperature profiles. The curves for the linear and Gaussian cases cross.

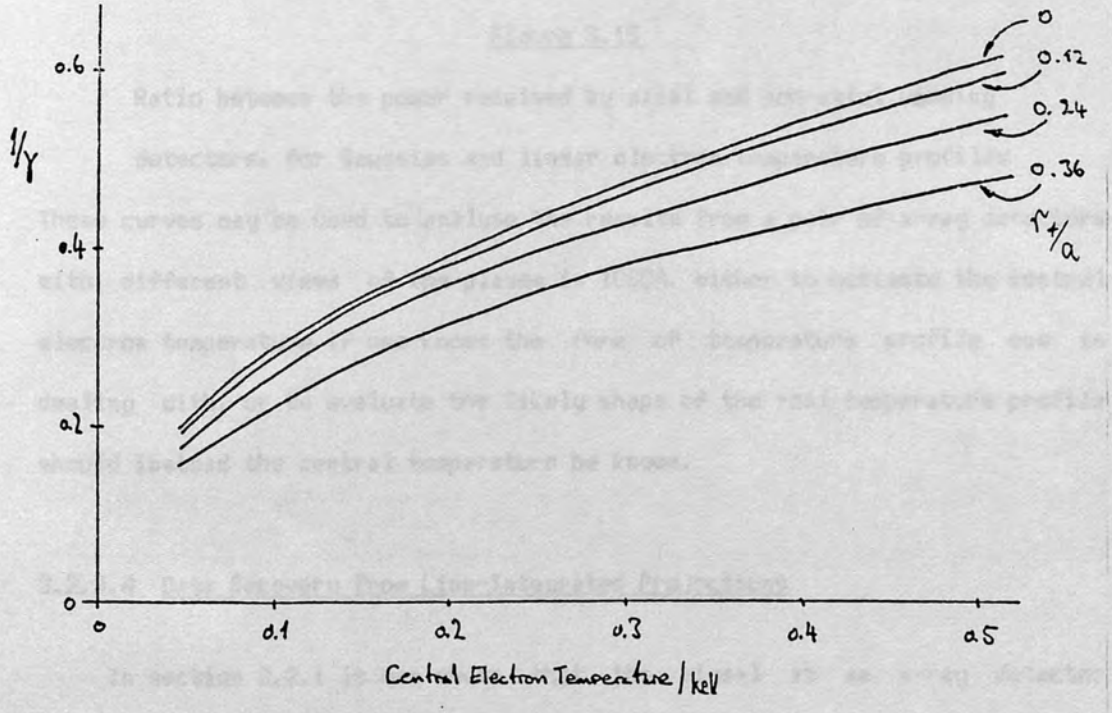

Figure 3.14

Radial variation of reciprocal temperature sensitivity: gaussian profile

As alpha is always a positive quantity, this implies that the lower the central temperature, the more peaked will be the emission profile. Figure 3.15 shows the calculated ratio R for chords as applicable to the TOSCA diagnostic, calculated in detail for the linear and Gaussian temperature profiles using equation 3.10.

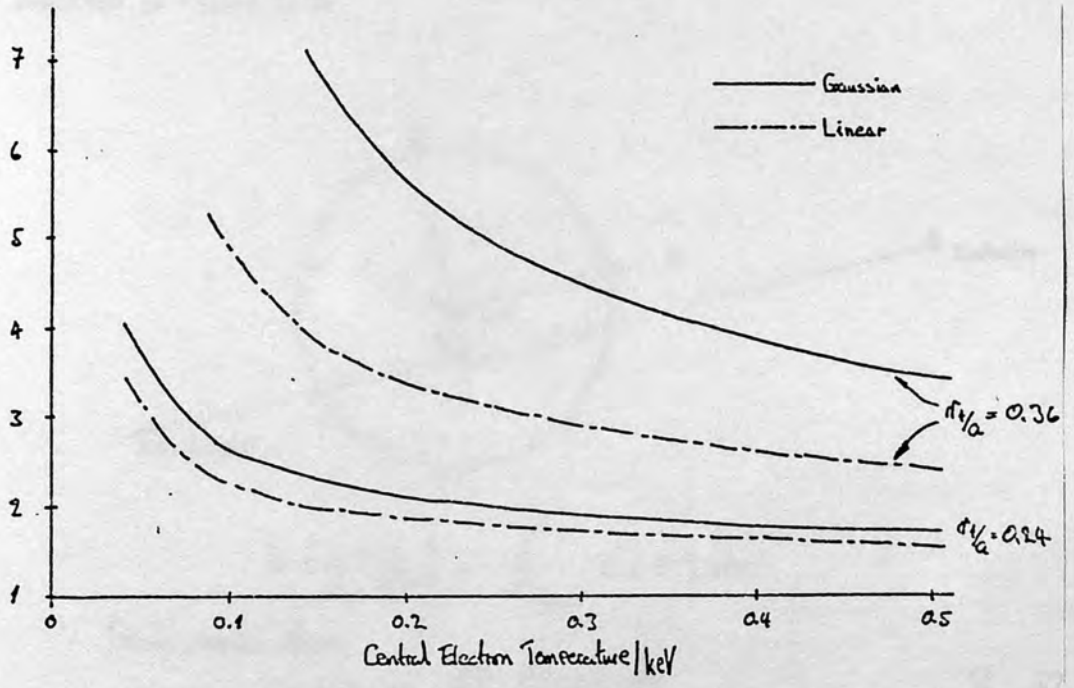

Figure 3.15

Ratio between the power received by axial and non-axial viewing detectors, for Gaussian and linear electron temperature profiles

These curves may be used to analyse the results from a pair of x-ray detectors with different views of the plasma in TOSCA, either to estimate the central electron temperature if one knows the form of temperature profile one is dealing with, or to evaluate the likely shape of the real temperature profile should instead the central temperature be known.

3.2.3.4 Data Recovery from Line-Integrated Projections

In section 3.2.1 it was shown that the signal at an x-ray detector viewing a region of optically thin plasma with good spatial resolution could be represented by a line integral of the the plasma x-ray emission coefficient

over the line of sight of the detector. If such a detector is viewing a cross-section of a tokamak or RFP, then the emission coefficient will vary along the line of sight as the plasma composition varies. Discussed here are some inversion techniques used to recover the local emission from the measured signals. The particular case of a plasma with cylindrical symmetry is depicted in figure 3.16.

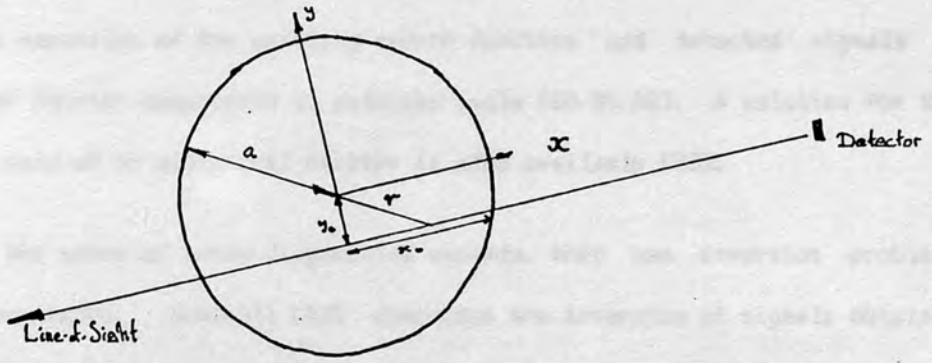

$$I(y=y_0) = \int_{-x_0}^{x_0} \varepsilon(r)\,dx$$

Circular symmetry allows:-

$$I(y) = \int_y^a \frac{\varepsilon(r).r.dr}{(r^2-y^2)^{1/2}} \quad . \quad . \quad . \quad 3.32$$

Figure 3.16

Detector viewing a cylindrically symmetric plasma

If the set of signals I(y) is available, then the local emission coefficient may be obtained from the Abel transform of equation 3.32 [75]:

$$\varepsilon(r) = \frac{-1}{\pi}\int_r^a \frac{I'(x)dx}{(x^2-r^2)^{\frac{1}{2}}} \; ; \quad I'(x) = \frac{dI(x)}{dx} \qquad 3.33$$

Due to the presence of the differential term, the numerical evaluation of the Abel inversion is prone to errors and noise in the usually sparse experimental data, to an extent which depends upon the shape of the emission distribution. These errors are accentuated by the presence of very steep profile gradients, and by hollow profiles, where the central local emissivity is less than that at some outer radius. As a result of this behaviour, numerical techniques for

the inversion abound in the literature, e.g. references 76,77,78.

Attempts have been made to extend the scope of the Abel inversion beyond the simple case described above, by making allowance for the effect of the spatial resolution of the detecting system [79], by giving consideration to observations of asymmetric sources [100], and to the effect of non-circular plasma cross-sections. This latter point is of significance in view of the trend toward tokamaks of non-circular cross-section. The technique is based upon the expansion of the emitting source function and detected signals in terms of Fourier components in poloidal angle [80,81,82]. A solution for the simpler case of an elliptical emitter is also available [83].

As the scope of x-ray diagnostics expands, then new inversion problems are encountered. Schivell [82] discusses the inversion of signals obtained from tangential views perpendicular to the major axis of a toroidally confined plasma, as opposed to the more usual case where the views are in a plane containing the major axis. Such a detector system is in operation on the Doublet III tokamak [104].

The Fourier series expansion of circular cross-section source functions has been pursued by Sauthoff [84,85]. The oscillating x-ray emissivity is represented as an expansion of the type:

$$\varepsilon(r,\theta,\phi,t) = \sum_m \sum_n \sum_\omega \varepsilon_{m,n,\omega}(r)\cos(\omega t - m\theta - n\phi - \Phi); \quad \Phi=\Phi(r,m,n,\omega) \qquad 3.34$$

Analytic solutions for the $\varepsilon(r)$ can then be found. This approach has yielded useful information on the radial structure of MHD modes in the PLT tokamak (see section 3.3). A copy of this code has been developed for the solution of inversion problems on TOSCA.

Direct image reconstruction has been attempted on the Alcator tokamak at MIT, by a group from American Science & Engineering, Inc., using techniques closely allied to those of medical computerised tomography [98,99,101,138]. This is a method for the production of two dimensional images resembling a

slice through a three dimensional object. The necessary data processing algorithms are well developed for use with the x-ray whole-body scanner. They have produced soft x-ray 'photographs' from the signals obtained from arrays of detectors [86,87,88]. However, resolution is limited by the available number of independent views of the plasma. On Alcator, a few tens of views are available, whereas a medical CT scanner uses several hundred thousand projections in the reconstruction of the cross section image.

Most of the procedures described here depend to an extent upon a model of the source function. The validity of the inversion then clearly depends upon the correctness of the model employed. Those procedures which seek to step around this difficulty by attempting a direct reconstruction of the source using only the measured data lose the information content of the model. Such techniques then require many more views of the source (in terms of viewing angles through the plasma to be imaged). The access limitations imposed by the tokamak configuration make this a difficult requirement to satisfy, and thus far images of only a very poor resolution have been obtained.

3.2.3.5 Temperature Measurement from X-ray Flux Ratios

Another situation that gives rise to the need of a close calculation of the signal from a x-ray detector is in the measurement of the electron temperature by the ratio of signals from two detectors viewing the plasma through different filters [57,58]. As the filter effects only the spectrum received by the detector, and the spectral form of the plasma emission is a function of temperature only, the ratio of the signals from two differently filtered detectors is a function of electron temperature only. For an accurate measurement the complete filter transmission must be taken into account, along with the spatial profiles of plasma electron temperature and density, and the spatial and charge-state distributions of impurity species. These calculations have been developed most fully by the TFR group [58,121],

whose results are in good agreement with measurements by Thomson scattering.

3.3 MULTI-CHORD SOFT X-RAY FLUX MEASUREMENTS

This section discusses the important results obtained to date from soft x-ray flux diagnostics of the tokamak. The readers attention is once again drawn to the distinction made between flux diagnostics, which monitor the x-ray power output in a broad x-ray band, and spectroscopic measurements which are first discussed in section 3.4.

3.3.1 REVIEW OF EXPERIMENTAL RESULTS

In tokamak diagnostics, the most important application of soft x-ray flux measurements has been to the study of the stability properties of the tokamak. In the section 3.2.3 it was shown that the x-ray flux signal was a sensitive function of the macroscopic plasma quantities. This was a consequence of the atomic processes responsible for the x-ray emission. Furthermore, the x-ray signal is dominated by the contribution from the relatively hot, dense plasma core. Under these conditions, the soft x-ray diagnostic may be seen to be a sensitive probe to the core plasma conditions.

The technique was first applied to the study of MHD behaviour on the ST tokamak [102,103]. The Princeton group were able to discover the structure and symmetry of various types of MHD activity, by comparison of the phases of the signals from detectors viewing the plasma at different toroidal and poloidal positions around the torus. In particular, they identified the $m = 0$, $n = 0$ internal (or sawtooth) disruption and its associated $m = 1$, $n = 1$ precursor; a continous $m = 2$, $n = 1$ mode; and evidence of a magnetic island structure in the large $m = 2$ mode preceeding major disruptions of the plasma column. Similar results were obtained from the ORMAK tokamak at Oak Ridge [105,106,107], using an array of nine detectors viewing across half the minor radius of the torus. These experiments provided data, which, for the

first time, could be compared with the predictions of tearing mode theory [108]. The results were in fair agreemamt with the model of the internal disruption as the growth of a tearing mode. Figure 3.17 shows a series of minor disruptions in the x-ray flux from the TOSCA tokamak, recorded during this course of this work using the instrument described in section 4.2.2. The figure shows the radial structure of the sawtooth oscillation as resolved by measurements along four chords in the minor cross-section. Figure 3.18 gives a similar view of continous m = 2 activity in a high current discharge in TOSCA.

Since the early work on ORMAK and ST, soft x-ray flux measurements have developed into an important diagnostic for the study of MHD behaviour. Multi-detector arrays, viewing the plasma in cross-section give good radial resolution; arrays positioned in more than one toroidal and poloidal location allow the measurement of the toroidal and poloidal mode numbers of the observed MHD activity. Such systems are operational on every large tokamak today, for example ISX [109,110], Doublet III [104], TFR [113,114,139], and Alcator [86]. This particular tokamak diagnostic has perhaps been brought to the highest state of development on PLT [111], and more recently PDX [112]. Signal analysis techniques have been developed (discussed in section 3.2.3.4) to separate the poloidal harmonic components of the measured flux. The radial functions of phase and amplitude can then be inverted, under a set of assumptions, to yield the local emission coefficient. Figure 3.19 shows the combined equilibrium (m = 0) and perturbed (m = 2 in this case) x-ray emissivity contours obtained from measurements on PLT. The island structure of the tearing mode is clearly visible. Local x-ray emission reconstruction has also been attempted on Alcator, using the techniques discussed in the previous section. The resulting distribution of the m = 1 and m = 2 components of x-ray emissivity is shown in figure 3.20.

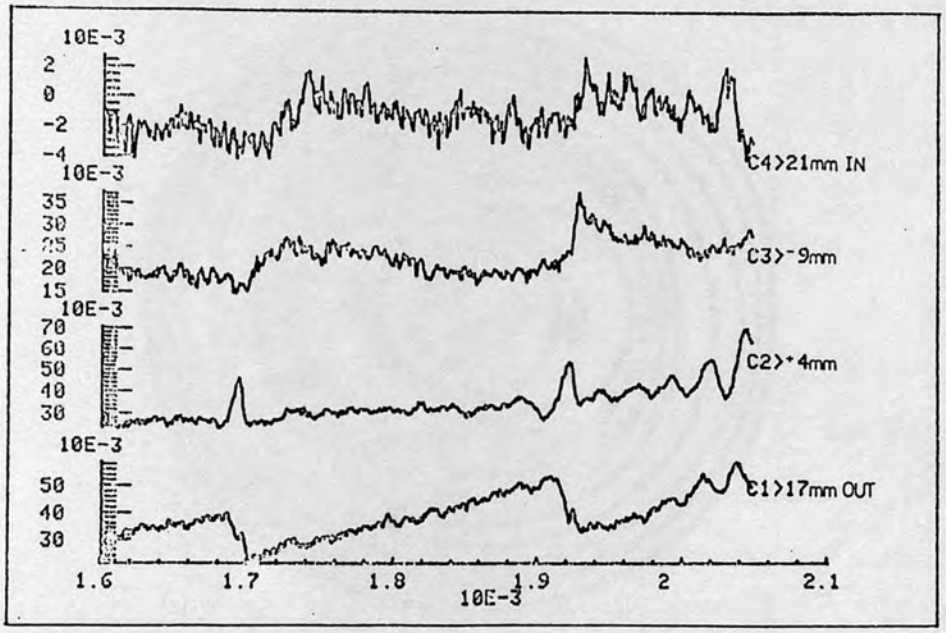

Figure 3.17

Sawtooth oscillations in the soft x-ray flux from TOSCA

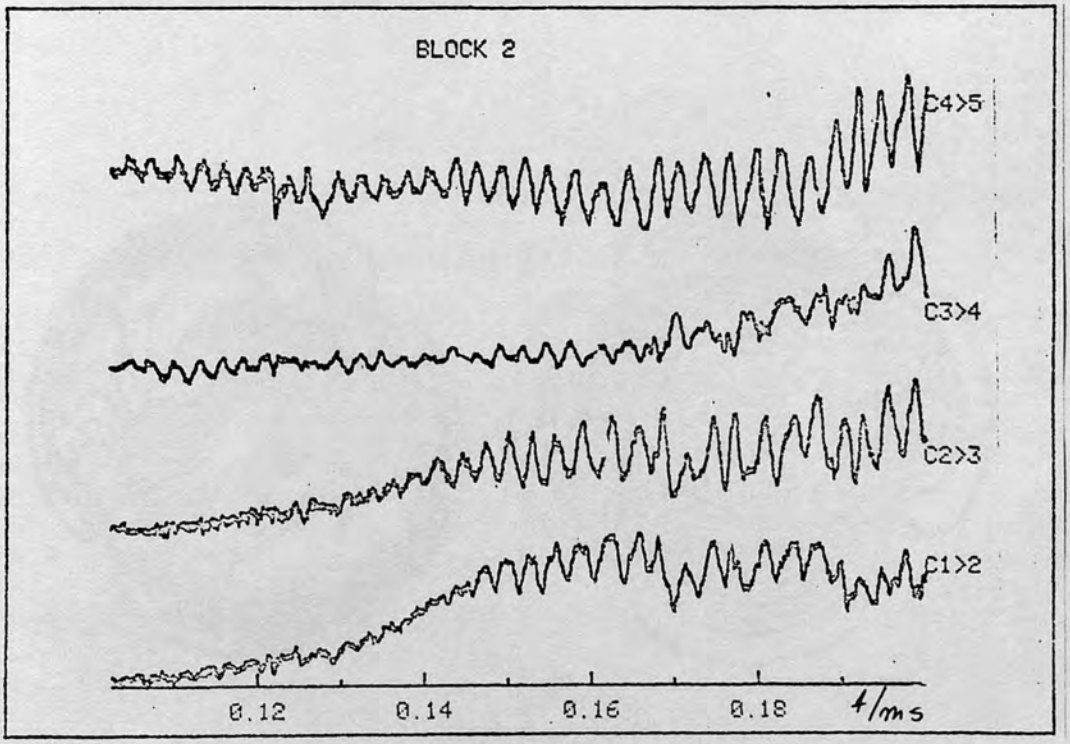

Figure 3.18

Continuous m = 2 mode observed with an array of soft x-ray detectors on TOSCA

Figure 3.19

Soft x-ray emission contour plot from PLT [111]

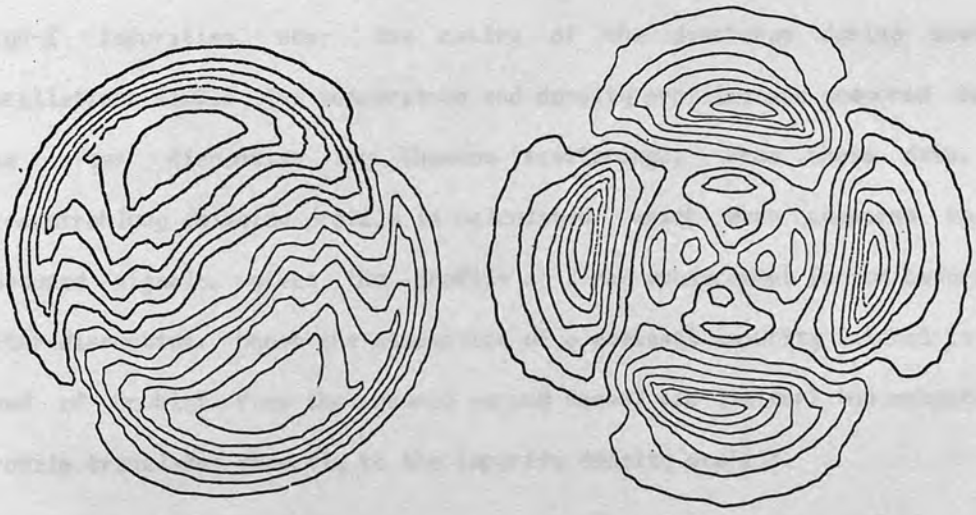

Figure 3.20

Soft x-ray emission contour plot from Alcator [86]

3.3.2 NUMERICAL SIMULATION OF X-RAY SIGNAL PROFILES

Although the reconstruction of the m = 2 mode, in terms of its x-ray emission characteristics has been quite succesful, difficulties are encountered in extending the technique to the study of the other features of a tokamak plasma. In particular, accurate measurements across the profile of tearing mode islands with weaker x-ray emission gradients have yet to be achieved, and there limits to the applicability of the inversion procedure (see remarks in section 3.2.3.4). An alternative in these cases is the calculation of the x-ray signal profile from some model of the mode magnetic (and hence temperature and density) structure and its evolution in time. Differences between these simulated signals and the experimental measurements are then minimised by adjustments to the parameters characterising the model. This technique has been applied to the study of m = 1 islands associated with the internal disruption on the PLT [115], TFR [116,117], and Doublet III [118] tokamaks, and to the W VII stellarator [120].

The Doublet team have used such an approach to determine the behaviour of high-Z impurities near the centre of the discharge during sawtooth oscillations [120]. The temperature and density profiles are measured before and after disruption (by Thomson scattering). From these data, the bremsstrahlung emission profile is calculated, which when compared to the measured signals, gives the profile of x-ray enhancement factor before and after disruption. Under the assumption of a dominant impurity (nickel in the case of Doublet, from the inconel vacuum vessel and limiter) the enhancement profile translates directly to the impurity density profile.

The simulation approach has been adopted in this work for the analysis on TOSCA, where the lack of ports restricts the number of data channels so as to preclude accurate numerical reconstruction. The models developed will be discussed later.

3.4 SOFT X-RAY SPECTROSCOPY

Discused here for the first time in this work are spectroscopic measurements, where individuals photons are detected and their energy measured.

3.4.1 SOFT X-RAY CONTINUUM SPECTRUM MEASUREMENTS

Measurements of the form of the continuum emission spectrum give direct information on the electron velocity distribution function. The emission from a thermal plasma, where the electrons adopt a Maxwellian velocity distribution, is given in section 3.1. The characteristic electron temperature is then simply determined from a semi-log plot of the emission power against photon energy, the temperature being proportional to the inverse of the gradient of the plot. Departures of the distribution function from Maxwellian are then evident as deviations from this simple spectrum. At first sight, the experimental requirements for this measurement would appear to be easily met, a scan with some energy resolving detector being the only requirement. In practice however, the total emission spectrum contains line features, and if these are viewed with poor energy resolution, incorrect conclusions may be drawn as to the nature of the measured spectrum. With this in mind, the most suitable detectors for this measurement have been found to be semiconductor detectors, in particular the lithium-drifted silicon detector, which can have a resolution of 160 eV or better at 5.9 keV. The Si(Li) detector combines the characteristics of good energy resolution with a wide sensitive range, operating with good efficiency for photon energies from less than 1 to 60 keV [122]. Operationally very similar, but with inherently poorer resolution is the gas filled ionisation chamber [123]. A germanium detector has also been used for tokamak spectroscopy [124]. At the high energy end of the emission spectrum ($h\nu \gg kT$, hard x-ray spectra) detector resolution is less important, and NaI scintillators may be used.

The semiconductor detector and ionisation chamber operate in a similar manner, each giving an output pulse upon the detection of an incident photon. The height of this pulse is proportional to the energy of the detected photon. The measured x-ray spectrum is obtained from the pulse-height spectrum of the detector output, the operation being performed by some pulse-height analysis system. This operational feature leads to a limitation on the photon counting rate, for if each pulse is to be accurately measured then it must not overlap with any other pulse. The overall counting rate is then determined by the time taken for the amplifier and pulse measuring system to process each pulse. The significance of the count rate is that it determines the time necessary to accumulate a spectrum with acceptably small statistical errors (the number of counts in any analysis channel following a Poisson distribution). This in turn sets the time resolution of a spectrum measurement, which may then have to be accumulated over several plasma shots. This situation of overlap of pulses in the electronics of the system is known as pile-up. It is important that the system should detect and reject these pulses, since they do not represent true photon energies, and would otherwise distort the measured spectrum [125]. This distortion naturally occurs at the high energy end of the spectrum, where the true count rate may already be very small. A detailed analysis of the electronics of, and the data obtained from, these systems is given in chapter 4 of this thesis, where the system employed on TOSCA for the measurements described in chapters 5 and 6 is described.

The pulse-height analysis system described above yields the photon number spectrum, in the form of $\Delta n/\Delta E$ as a function of the photon energy E, where Δn is the number of counts in a channel of width ΔE. The x-ray power spectrum is obtained by multiplying the number of counts in a channel by the energy of the channel, so a good energy calibration of the system is important. The channel width and spacing may be chosen to suit the particular experiment. If one is working in a region of the spectrum free of line features, then 8 - 10 separated channels may suffice for a Te measurement [126,127,128]. Where it

is necessary to resolve lines in the spectrum, as is usually the case, then continuous energy analysis is necessary , using adjacent energy channels, and channel widths appropriate to the detector resolution.

After some years of development, pulse height analysis systems have reached a considerable degree of sophistication. On the larger fusion plasma experiments integrated systems under the control of a local computer have been implemented. The computer can acquire and store spectra recorded at several time intervals during the discharge. Using multi-detector systems, a satisfactory spectrum can be recorded from one shot, the computer being used for the synthesis of the total spectrum from the data collected by several detectors, each filtered differently to view a different energy region of the spectrum. In between shots the detector may be moved to make a radial scan of the plasma. Radial profiles of various plasma parameters may be then deduced, by an Abel inversion of the analysed spectral data. Tokamak parameters which have been evaluated in this way [61] are the electron temperature (and from it the q-profile, by calculation of the plasma resistivity, as discussed in section 5.2), and electron energy confinement time. The input of information from other basic tokamak diagnostics allows further the estimation of the streaming parameter (the ratio of electron drift to thermal speed), impurity ion density (from emission line strength), and effective ionic charge (from x-ray enhancement factor). Some of these measurements will be discussed further in this text.

3.4.2 OTHER SOFT X-RAY SPECTROSCOPIC RESULTS

Spectroscopy plays an important role in the determination of the identity and spatial distribution of impurity ion concentrations and charge-states. Visible and ultra-violet spectroscopy [129] yields information on the relatively cool edge region of a tokamak plasma; the x-ray spectrum has its origin in the hot core region.

Spectroscopic measurements have shown the significance of impurity line radiation as a power loss mechanism in the overall tokamak energy balance. A result of particular note was the effect of tungsten radiation on the performance of the PLT tokamak. In this machine a tungsten rail limiter was in use for a time. Measurements with a grazing incidence spectrometer [130] revealed strong radiation in three bands, and that in the centre of the discharge the radiation power exceeded the Ohmic input power. Not surprisingly, these discharges were characterised by a hollow temperature profile.

Spectral studies allow the determination of the impurity charge state distribution, an example being the measurement [131] of the iron K line transition fine-structure. Measurements have been performed on the iron spectrum [132], as described in section 3.1. Very high resolution ($\lambda/\Delta\lambda$ = 15 000) curved-crystal spectrometers [132,133,134] are used for this work.

Ion temperature measurement, by the Doppler broadening of line radiation, is likely to become important on the larger tokamaks under construction today. The existing technique of neutral-atom energy analysis becomes inappropriate with increasing plasma minor radius and decreasing neutral particle mean free path due to higher plasma temperature and density.

Further diagnostic applications have been proposed, regarding the electron density-dependent observation of forbidden x-ray lines in tokamak plasmas [135]. An up to date review of the state of advanced spectroscopic diagnostics of tokamak plasmas is given in reference 136. The wider field of laboratory plasma spectroscopic diagnostics is reviewed in reference 137.

CHAPTER 4 THE TOSCA TOKAMAK

TOSCA is a small tokamak (major radius R = 0.3 m, minor radius a = 0.08 - 0.1 m), built to study the effects of minor cross-section shaping and compression on plasma confinement and stability [140]. The machine was modified in 1979 to allow access for the injection of microwave power from two 28 GHz gyrotron devices. The first of these gyrotrons has been in operation since September 1980, delivering RF power of up to 170 kW to the toroidal chamber.

The confined plasma is enclosed by a stainless steel toroidal vacuum vessel, of 180 μm thick bellows construction. Immediately outside the vessel are sixteen single-turn axisymmetric E windings, which follow the vacuum vessel in major circumference. These windings may be connected serially, in parallel, or separately to capacitor banks, and are used as the primary windings, i.e. for the induction of the plasma current, and for providing the poloidal shaping field.

The toroidal field is generated by twenty four series-connected single turn windings, which enclose the vacuum vessel and E-windings in minor circumference. The vertical equilibrium field component is provided by four single turn series connected axisymmetric coils, situated outside the toroidal field coils. The principle parameters of the TOSCA machine are summarised in table 4.1.

4.1 ENGINEERING SUBSYSTEMS

4.1.1 VACUUM SYSTEM

The absolute necessity of impurity control for successful tokamak operation sets stringent vacuum system requirements. The torus is pumped directly by two 500 l/s turbo-molecular pumps. Diagnostic and other assemblies are initially pumped by one of several available 100 l/s TMP rigs

before being opened to the main machine vacuum. A torus base pressure of 10^{-8} torr is achieved.

Standard TOSCA Parameters

R	30 cm
a	8.5 cm
I_p	<25 kA
B_ϕ	0.3 - 1.3 T
q(a)	$\gtrsim$ 1.4
$\bar{n}_e$	0.5 - 3.10^{19} m^{-3}
$T_e(0)$	100 - 400 eV
$T_i(0)$	100 eV
T_σ	30 -100 eV
τ_{Ee}	200 - 1200 µs
V_L	1 - 4 V
P_{OH}	20 - 60 kW

Parameters for ECRH Experiments

I_p	6 - 8 kA
V_L	$\sim$ 2 V
B_ϕ	4.5 - 5.5 kG
$\bar{n}_e$	< 1.10^{19} m^{-3}
T_{e0}	~250 eV
T_{i0}	30 - 40 eV
$Z_{eff}(r)$	$\sim$ 2

Table 4.1

TOSCA parameters

4.1.2 POWER SUPPLIES

All the machine field windings are energised by capacitor banks. The capacitor banks are fired and crowbarred by ignitron circuits.

Toroidal Field

The 24 turn toroidal field coil is powered by six 2 840 μF, 8 kV modules, giving a maximum stored energy of about 600 kJ. An additional module may be used to provide a fast rise of field during the plasma pulse, or alternatively to maintain a more constant toroidal field. The field ripple between coils has been measured, and was found to be less than 1% on the minor axis, and less than 3% at the limiter radius. The maximum field obtainable on axis is 13 kG. The toroidal field system circuit is shown, as an example of a capacitor power system, in figure 4.1.

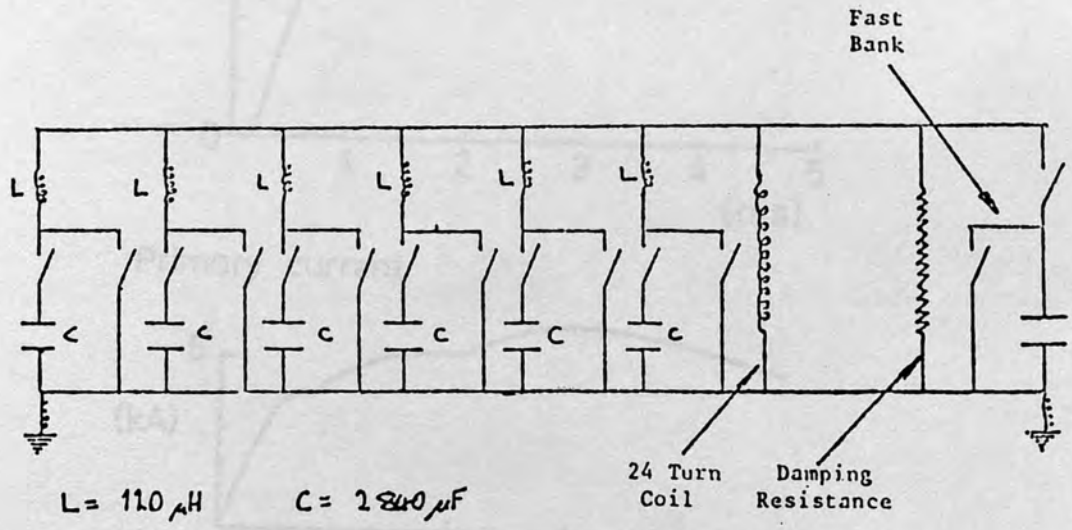

Figure 4.1

TOSCA toroidal field circuit

Ohmic Heating System

With respect to the Ohmic heating function, E windings are selected so as to minimise stray fields inside the vacuum vessel whilst maximising the generated poloidal flux. The E bank consists of two 8 kV/86 kJ modules. Fine control of the shape of the plasma current is achieved by the forward or

backward firing of additional 'boost' banks.

Vertical Field

The vertical field system is powered by two 1 368 μF/8 kV banks, and three 1 260 μF/300 V electrolytic banks. The bank voltages and timings must be carefully selected to compensate position shifts due to changes in plasma current, internal inductance, and $\beta\theta$, all of which are directly affected by ECRH.

Some typical power supply current waveforms are illustrated in figure 4.2.

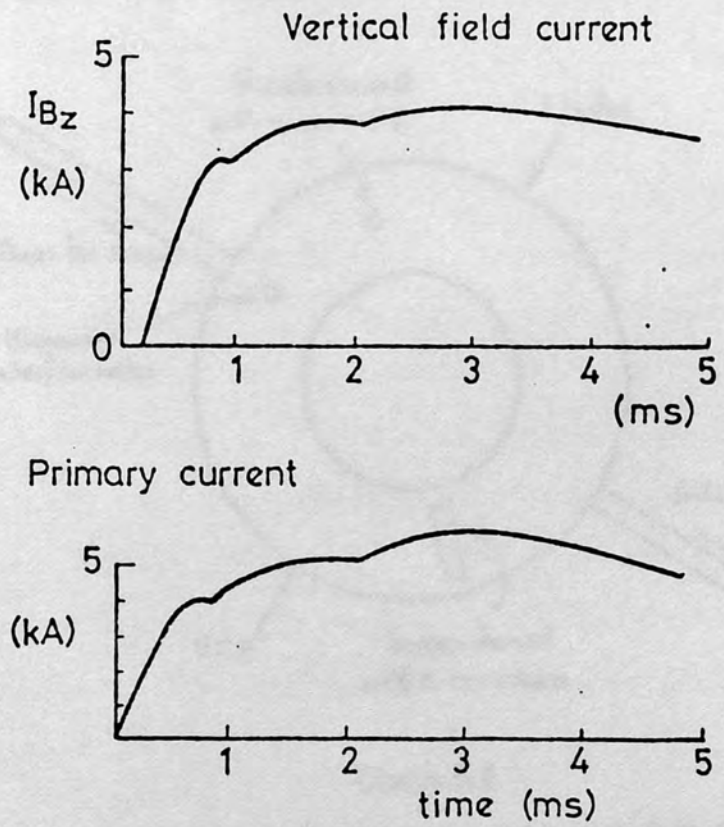

Figure 4.2

Typical waveforms for the primary and vertical field circuits

4.2 PLASMA DIAGNOSTICS ON TOSCA

This section describes the plasma diagnostics available on TOSCA. As the bulk of the work presented in this thesis consists of soft x-ray measurements, particular attention is given to the soft x-ray diagnostics. The division of soft x-ray diagnostic techniques has been discussed in chapter 3. The soft x-ray diagnostics available on TOSCA consist of a Si(Li) detector and pulse-height analysis system, a seven element array of surface barrier diodes (monitoring the flux in a band from less than 1 to 10 keV, at seven chords through the minor cross-section), and a single probe-mounted surface barrier detector, with an angled collimator.

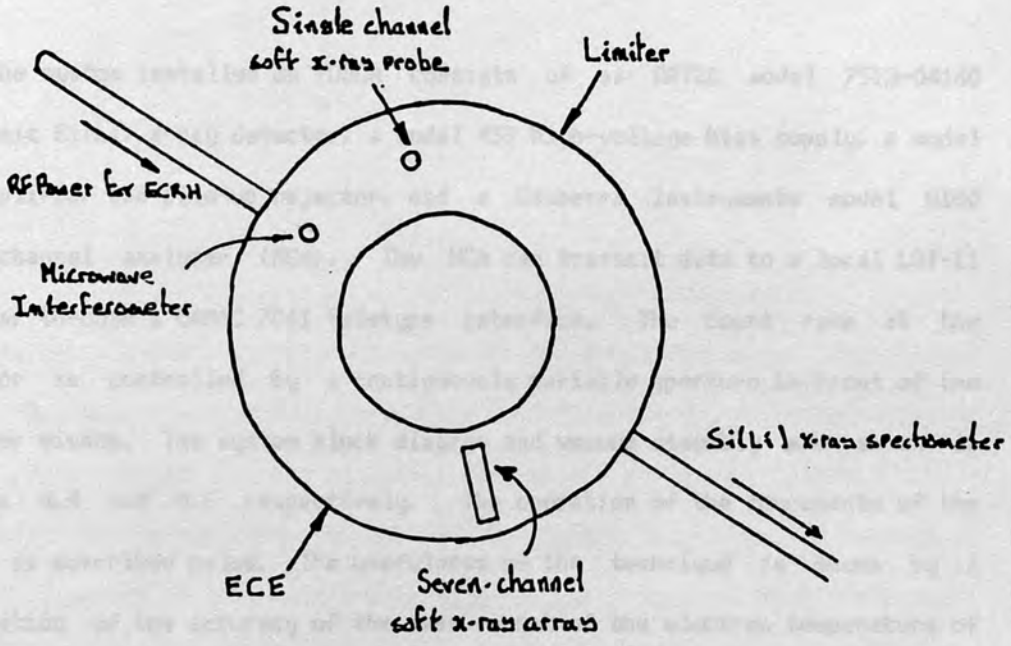

Figure 4.3

Layout of the TOSCA diagnostics: plan view from above.

A number of the other standard tokamak diagnostics [141] are available on TOSCA for the routine measurement of the basic plasma parameters. Those relevant to this work are also briefly described below. These are the microwave interferometer, magnetic pick-up coils, loop voltage monitor and diamagnetic loop. The distribution of these diagnostics around the torus is

shown in figure 4.3.

4.2.1 THE X-RAY ENERGY PULSE-HEIGHT ANALYSIS SYSTEM

The pulse-height analysis (PHA) system used on TOSCA employs a lithium-drifted silicon [Si(Li)] diode to detect individual x-ray photons. The energy of each detected photon is converted into an analogue voltage pulse by the system electronics. An x-ray flux incident upon the detector results in a stream of such pulses, which are analysed according to their amplitude by a multi-channel pulse-height analyser (MCA). The resulting pulse height spectrum is the convolution of the x-ray spectrum of the observed source, and the instrumental function of the detecting system.

The system installed on TOSCA consists of an ORTEC model 7513-04160 cryogenic Si(Li) x-ray detector, a model 459 high-voltage bias supply, a model 572 amplifier and pile-up rejector, and a Canberra Instruments model 8100 multi-channel analyser (MCA). The MCA can transmit data to a local LSI-11 computer through a CAMAC 7061 teletype interface. The count rate at the detector is controlled by a continuously variable aperture in front of the detector window. The system block diagram and vacuum assembly are shown in figures 4.4 and 4.5 respectively. The operation of the components of the system is described below. The usefulness of the technique is shown by a calculation of the accuracy of the measurement of the electron temperature of a Maxwellian plasma.

4.2.1.1 <u>The Detector and Basic Electronics</u>

The detector diode is shown schematically in figure 4.6. The diode is constructed from a cylindrical piece of p-type silicon. Lithium is carefully diffused through the crystal in order to act as an interstitial donor species which almost exactly compensates the fixed acceptors. This lithium compensation permits the construction of a large depth of

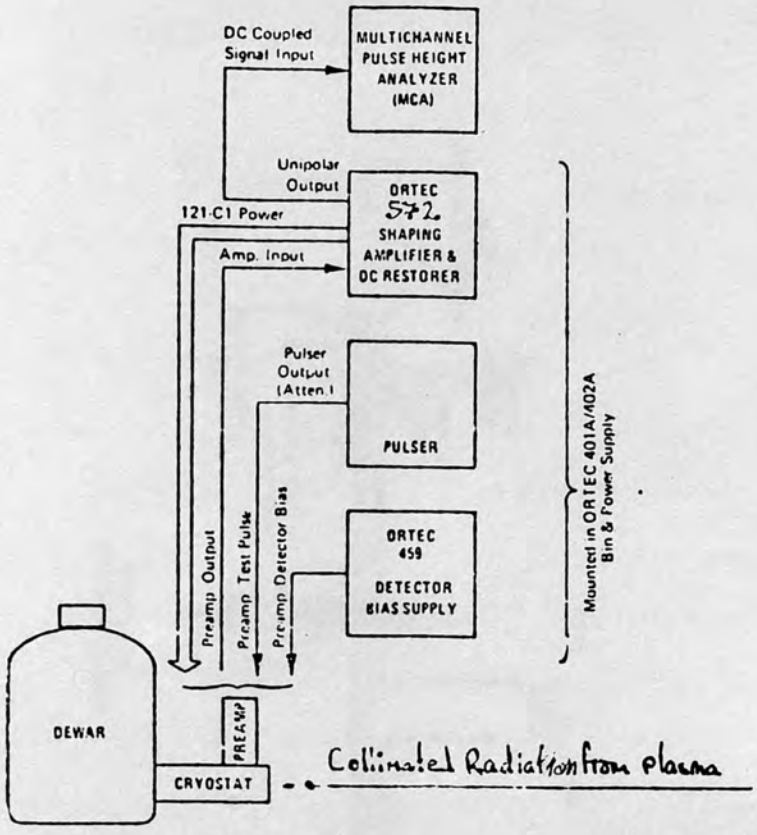

Figure 4.4

X-ray energy pulse height analysis system block diagram

high-resistivity intrinsic silicon, which in the completed device corresponds to a deep photon-sensitive layer. Upon completion of the drifting process a gold surface barrier junction is established at the end of the crystal, thus completing the diode structure [143]. The formation of the gold contact is thought to result in a thin (approximately 0.1 μm) p-type silicon dead-layer adjacent to the contact. By applying a reverse bias of about 1 kV to the diode, most of its volume is depleted of remaining free charge carriers. An x-ray photon entering the diode through the front contact (0.02 μm of gold plus approximately 0.1 μm of silicon dead layer) interacts by the photo-electric effect to produce electron-hole pairs. The Compton effect and pair production are unimportant at the low energies of interest here. The number of electron-hole pairs produced, n, is proportional to the photon energy E:

$$n = \frac{E}{\epsilon} \qquad 4.1$$

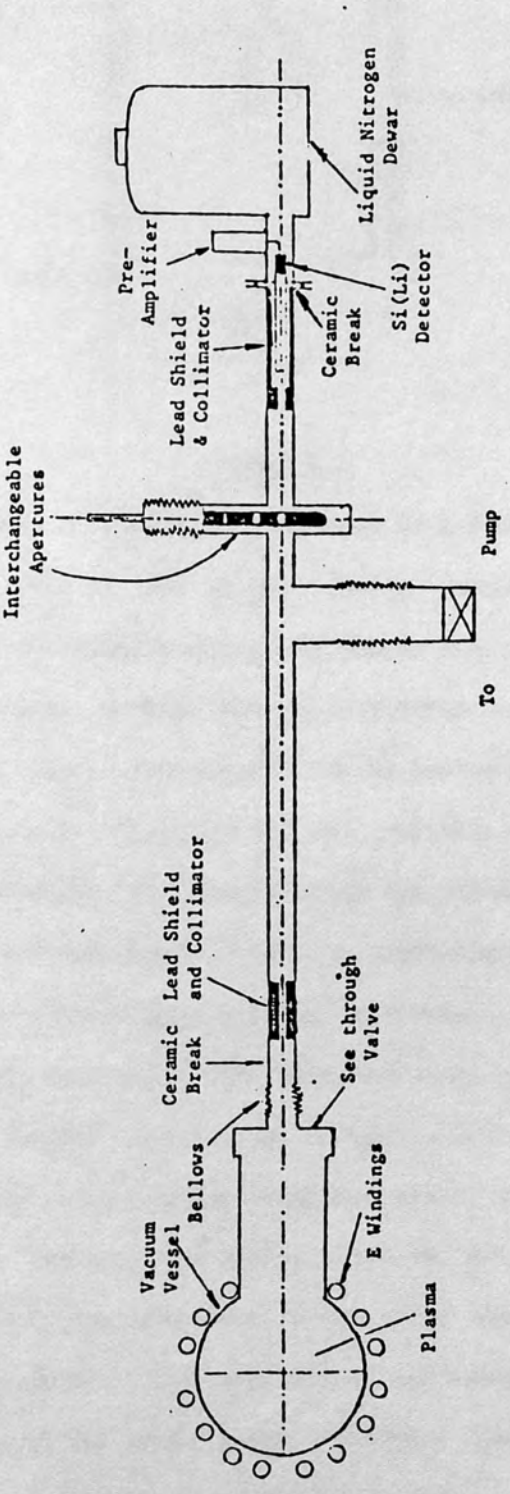

Figure 4.5

Silicon (lithium) x-ray detector vacuum assembly

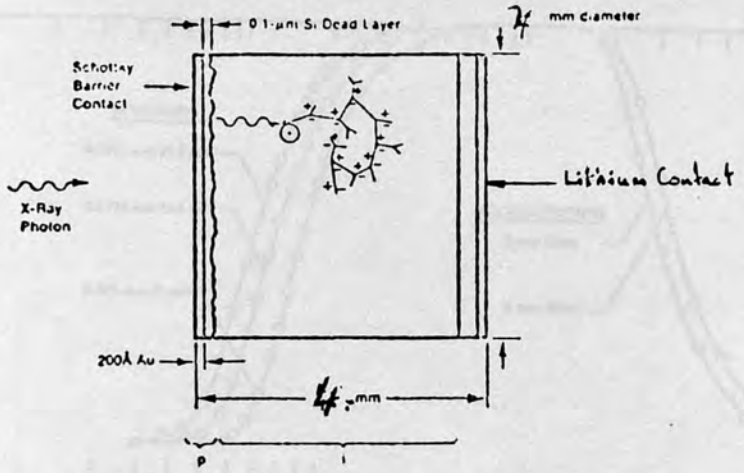

Figure 4.6

Schematic view of the mode of operation of a Si(Li) detector.

where $\mathcal{E}$ = 3.8 eV, and is the average energy required to produce an electron-hole pair in cooled silicon. The charge thus produced is swept from the diode by the bias voltage and is collected by a charge-sensitive pre-amplifier. The output pulse produced by the pre-amplifier is proportional to n and hence also to E. To restrict lithium mobility in the diode, and to minimise electronic noise, the detector diode and pre-amplifier front-end are operated at liquid nitrogen temperatures. A light-tight combination vacuum cryostat and liquid nitrogen Dewar are used to provide a clean environment for the Si(Li) diode, and to prevent light generated noise in the detector. X-ray photons from the plasma pass through an 8 μm beryllium window to reach the detector. Figure 4.7 shows the calculated full-energy detection efficiency as a function of of the beryllium window thickness, and of detector sensitive depth. The curve gives the probability of measuring the full energy of a normally incident photon. This does not include events that result in less than the full energy of the photon being recorded. Low efficiency at low energies is due to absorption in the entrance window i.e. the beryllium front window, gold contact and silicon dead layer. At high energies limited detector depth reduces the detector response. A bias voltage for the Si(Li) diode is supplied by a low-noise, low-current high-voltage supply (ORTEC model 459) through filters in the pre-amplifier.

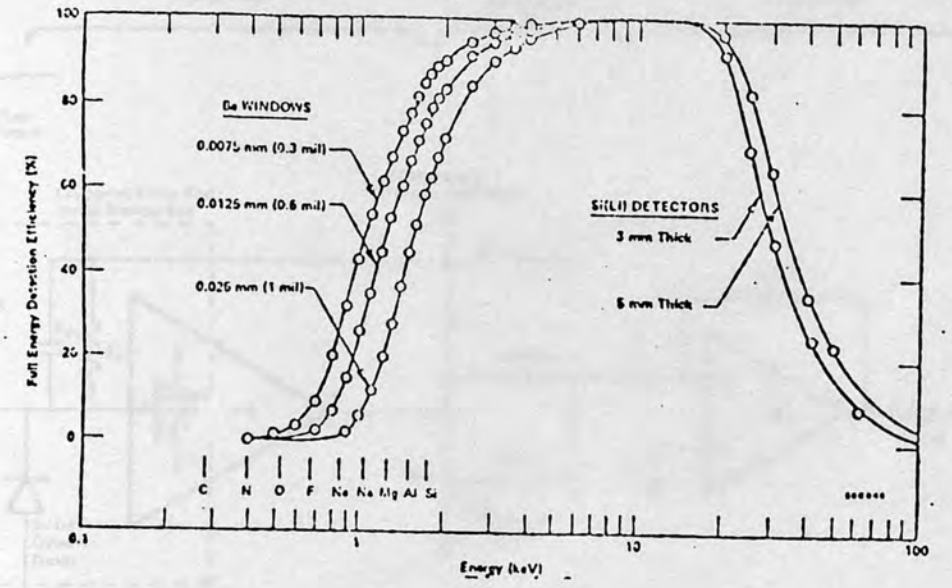

Figure 4.7

Full-energy detection efficiency of Si(Li) detectors.

The Pre-Amplifier consists of three sections, shown schematically in figure 4.8. The charge-loop is an operational integrator that forms a charge sensitive amplifier. The FET gate input is held at ground potential by a DC feedback element, represented by the resistor R_F, which prevents the charge-loop output voltage from drifting to the supply voltage by slowly removing the charge stored on the capacitor C_F. However, the time constant R_FC_F appears as an exponential decay of the charge-loop output pulse. Since the charge from the detector must flow through the feedback resistor, there exists a mean DC voltage at the charge loop output. This mean level is proportional to the rate of production of charge in the detector, and effectively limits the count-rate when the mean voltage reaches the level of the power supply. The pole-zero-cancelled differentiating network is employed to preserve the count-rate capability by replacing the long decay-time of the charge-loop output with a much shorter (50 μs) decay, thus reducing the mean voltage level by $R_FC_F/50\ \mu s$, and permitting furthur amplification before power supply voltages again limit the counting rate. The operation of the network is illustrated in figure 4.9. The output driver

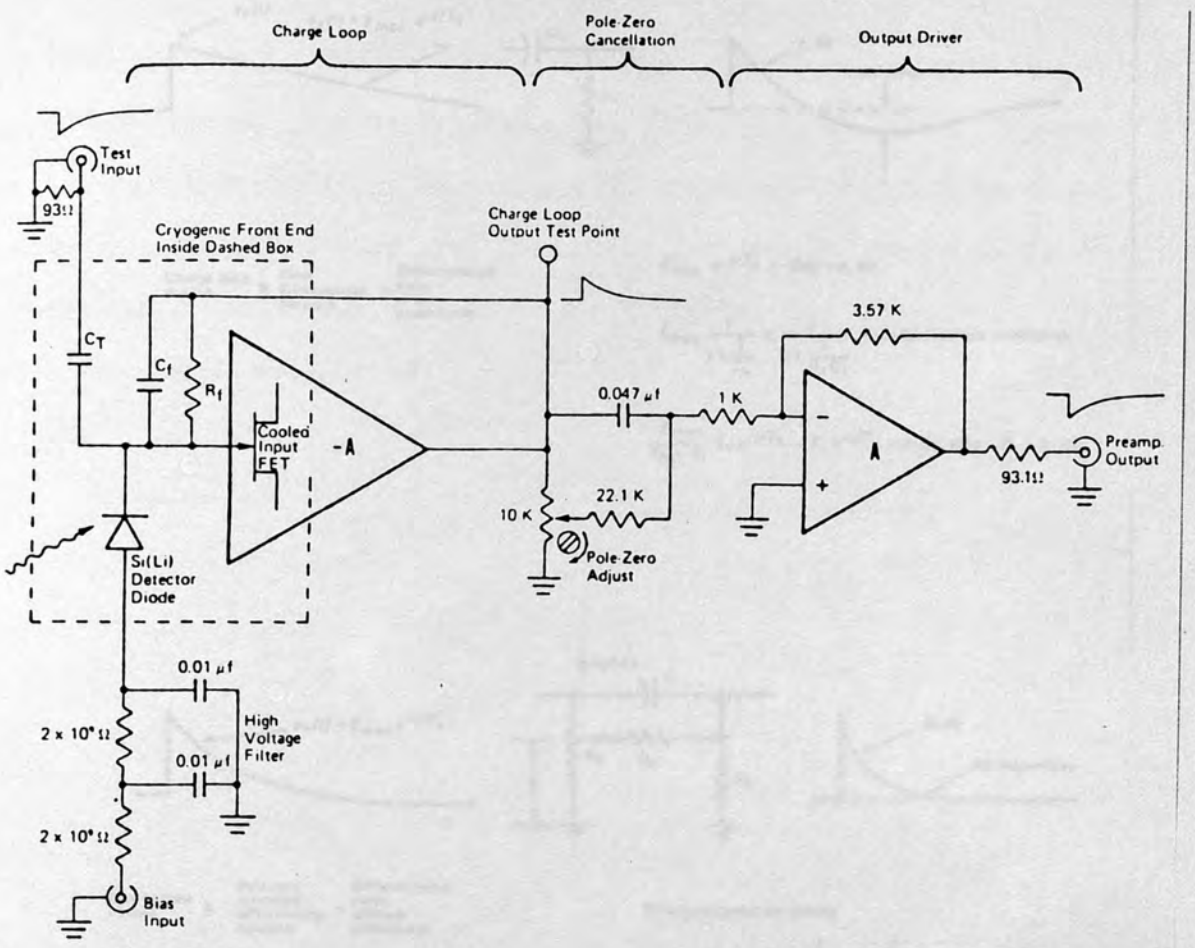

Figure 4.8

Schematic diagram of ORTEC 117B pre-amplifier

is an inverting amplifier with a gain of 3. The output is matched for 93Ω co-axial cable.

A Shaping Amplifier [156] (ORTEC 572) is employed to amplify the signal to a measurable level for processing by a multi-channel pulse-height analyser. The amplifier block diagram is shown in figure 4.10. Band-pass limiting filters improve the signal-to-noise ratio by rejecting low and high frequency components. A further pole-zero-cancelling differentiator is used to remove the low frequency (50 μs) decay of the pulse from the pre-amplifier. High frequency noise (e.g. FET gate and drain thermal noise) are removed by a 4-pole active integrator.

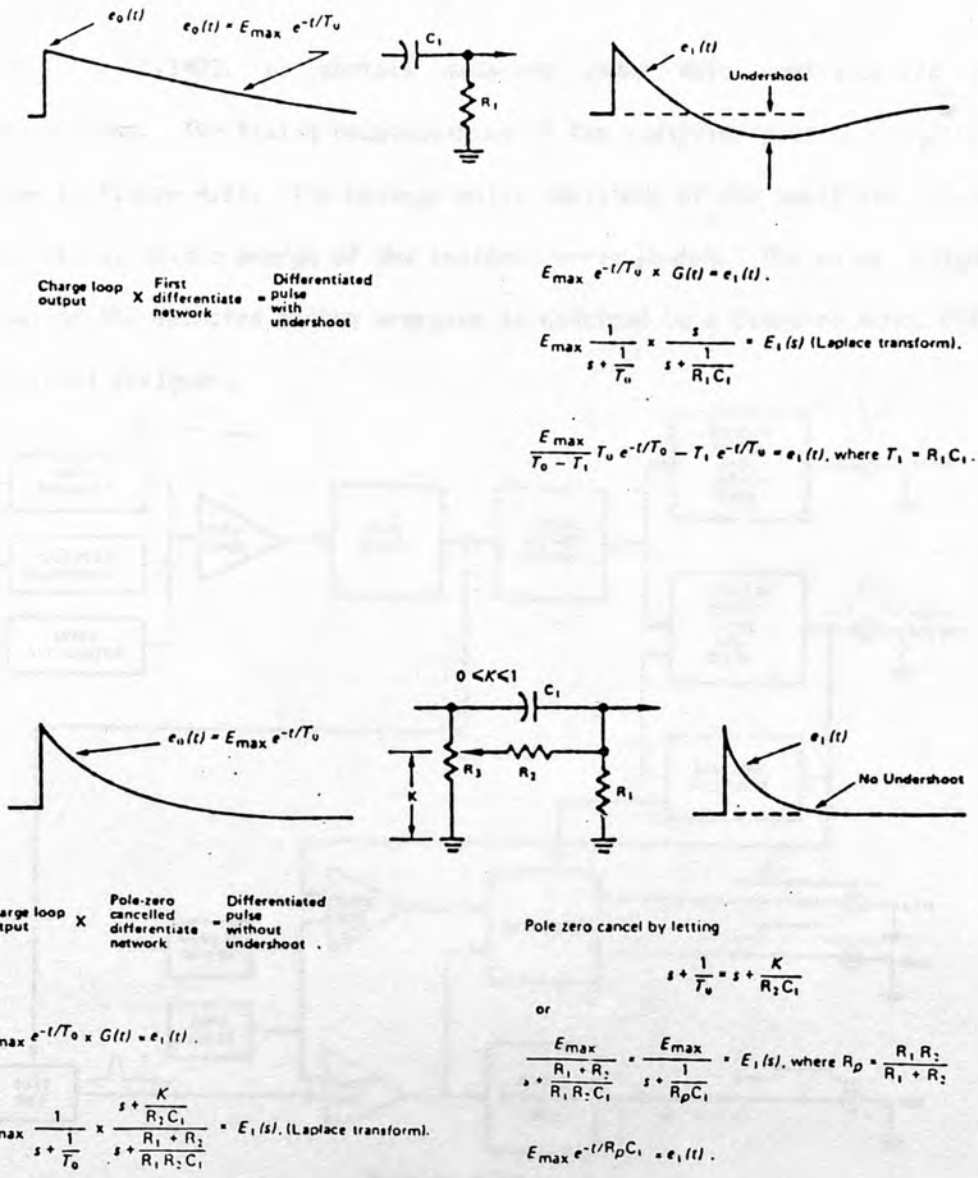

Figure 4.9

Differentiation in a pole-zero cancelled amplifier

The time constants of the differentiating and integrating stages may be varied (together) in the range 0.5 - 10μs. The ORTEC 572 amplifier incorporates a baseline restorer, which maintains the output DC level between pulses to ground potential, to as high a count rate as possible. This is necessary since the MCA measures pulse height with respect to ground potential, so a shift in the amplifier baseline would result in a shift in the recorded spectrum. The amplifier also detects the arrival of more than one photon at the detector within the period required by the amplifier to process one pulse, a condition known as pulse pile-up. Pulse pile-up distorts the recorded

spectrum [122,125,142], so photons detected under this condition are not further analysed. The timing relationships of the amplifier/pile-up rejector are shown in figure 4.11. The voltage pulse amplitude of the amplifier output is proportional to the energy of the incident x-ray photon. The pulse height spectrum of the detected photon energies is obtained by a Canberra model 8100 multi-channel analyser.

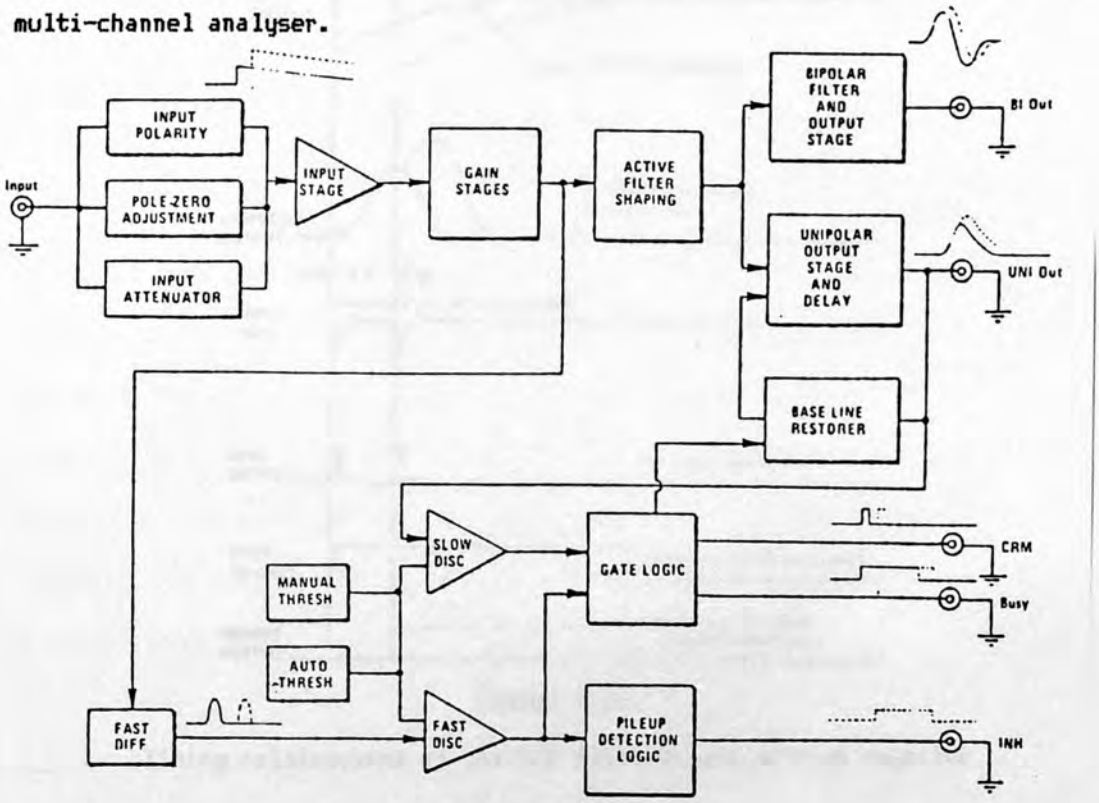

Figure 4.10

Shaping amplifier block diagram

Multi-Channel Analyser The MCA obtains the pulse-height spectrum of the shaping amplifier output. This signal is DC coupled to the analogue-to-digital convertor (ADC) of the MCA. The A/D conversion is carried out by precisely charging a capacitor to the amplitude of the input, then discharging the capacitor at a constant rate. During the discharge, crystal-controlled clock pulses are counted in a register. When the capacitor is discharged to ground potential, the number in the register represents the height of the signal. This number is used to select a location in the memory of the instrument, the contents of which are then incremented by one. Total count rates are mainly determined by the duration of the shaped pulse from the

main amplifier [126]. For usage on TOSCA, the shaping time constant is approximately 1 μs, and count rates of 100 K s^{-1} can be realised.

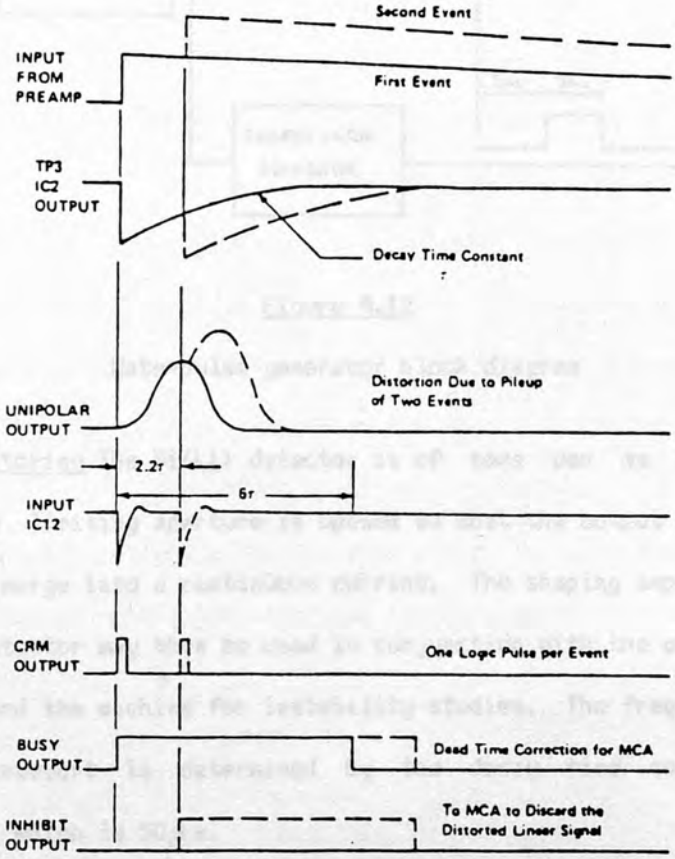

Figure 4.11

Timing relatioships in the 572 amplifer and pile-up rejector

A Simple Gating Unit , acting on the gate of the MCA, allows the spectrum to be recorded only during a selected time interval. The gating unit also furnishes an end-of-shot pulse which may be used to end the collection of data, and to initiate the transfer of data from the analyser memory to a local computer for permanent storage and analysis. This facility allows for the automatic transfer of data to the computer after each shot. The gate-pulse generator block diagram is shown in figure 4.12. It was simply constructed from standard 74-series TTL integrated circuits. A single dual-monostable chip is suffices to produce a variable duration, variable delay signal of the type of GATE.

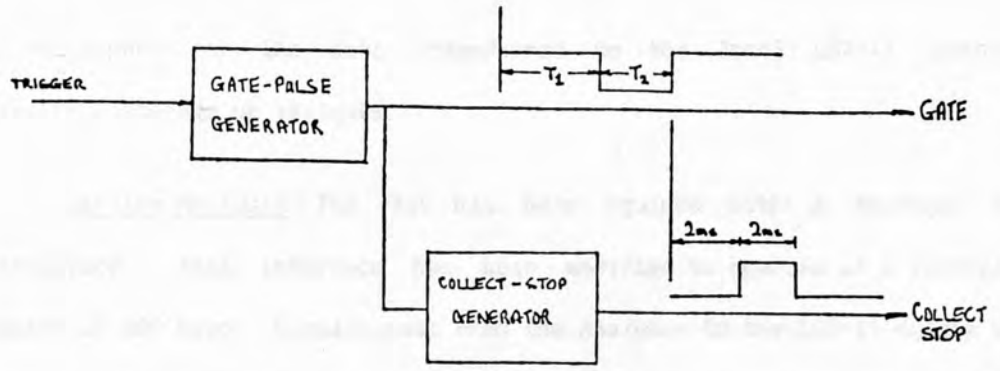

Figure 4.12

Gate-pulse generator block diagram

Flux Monitoring The Si(Li) detector is of some use as an x-ray flux monitor. The limiting aperture is opened so that the output pulses from the pre-amplifier merge into a continuous current. The shaping amplifier is not used. The detector may then be used in conjunction with the other soft x-ray detectors around the machine for instability studies. The frequency response of this arrangement is determined by the decay time constant of the pre-amplifier, which is 50μs.

4.2.1.2 Data Display and Storage

The data system offers a number of storage, analysis and display options.

Oscilloscope and Camera The raw output from the amplifier may be displayed on an oscilloscope and recorded by a camera. This may be the most convenient method when operating the detector in the intensity monitoring mode. Pulse height analysis of the photographed signal from the shaping amplifier may be done 'by hand', but this is a rather tedious process.

PHA with a Multi-Channel Analyser Automatic pulse height analysis of the x-ray signal is performed by a Canberra Instruments model 8100 MCA. The spectrum is recorded under timing control, and the results of a sequence of shots are accumulated in the analyser memory. When sufficient data has been collected (usually several tens of shots), the analyser display may be

photographed, or the data transferred to the local LSI-11 computer for listing, storage or analysis.

On-line Analysis The MCA has been equiped with a teletype output interface. This interface has been modified to operate at a transmission speed of 600 baud. Signals pass from the analyser to the LSI-11 system via a model 7061 teletype interface located in the computer CAMAC crate. For continuous analysis the spectrum of each shot is recorded in the analyser and transferred to the LSI-11 at the end of each shot. This process takes some 10-20 seconds, depending on the number of data channels selected. When the transfer is complete, the data is stored on a magnetic disc file, and the analyser memory is reset ready for the next shot. The accumulated results of the current series of shots are processed for display on the monitor screen.

4.2.1.3 System Software Components

The collection, storage, processing and display of the soft x-ray spectrum data may be broken down into a number of separate tasks. These tasks have been coded so that each is performed by one call to a subroutine. The resultant subroutines are linked to produced two programs. The first is mainly concerned with the collection and storage (on magnetic disc files) of the raw data from each shot (or group of shots, if operated manually). However some pre-programmed analysis of the data accumulated over a series of shots is performed. The displayed results then serve as a monitor of the progress of the experiment. A second program permits a selective analysis of previously recorded data, by allowing the user to interactively create a list of data files, the cumulative contents of which are then processed. Since the spectrum of each shot may be stored in its own identifiable data file, this feature allows for the rejection of known atypical shots, thus eliminating their influence on the measured spectrum.

4.2.1.4 Measurement of Electron Temperature

In chapter 3 it was shown that the electron temperature of a plasma with a Maxwellian electron velocity distribution function could be obtained by fitting an exponential function to the continuous soft x-ray emission spectrum, regardless of the impurity content of the plasma. Furthermore, the strongly peaked spatial profiles of temperature and density characteristic of the tokamak imply a strong peaking of the spectral intensity. This intensity peaking, together with the fact that the minimum measured photon energy is much greater than the mean electron thermal energy (at least in TOSCA), generally results in the measurement of the peak electron temperature along the line of sight of the spectrometer [124]. The factors which influence the accuracy of the temperature measurement obtained from the PHA system in use on TOSCA are discussed below.

Accuracy of the Spectrum Measurement

Three factors may be identified as influencing the accuracy of the measurement of the continuum emission by a Si(Li) detector and PHA system. These are:

i) the necessity of maintaining a clean environment around the detecting diode results in soft x-ray photons having to pass through a window to reach the detector. The x-ray transmission of this window is strongly dependent on photon energy, the transmission being less than 50% for photon energies of less than about 1 keV, which is very significant for the plasma temperatures under study in this work. The Schottky contact and silicon dead-layer also make a small contribution in this respect. The effect of these photon absorbers is to filter the spectrum. The modified spectrum, as received at the detector, is illustrated in figure 4.13.

ii) the energy resolution of the detector system, which must be sufficiently high to record the detail of the peaked form of the filtered spectrum at the detector.

iii) the pulse-height analysis of the recorded spectrum into energy channels of a finite width. The significance of finite channel width is evident when one attempts to correct the measured spectrum for the effect of absorbers, for at low energies the correction factor may change significantly across the width of a channel.

The interplay of these three features is conveniently studied numerically. The procedure adopted is as follows. First, a virtually continuous spectrum (1 eV steps) is calculated. The spectrum at the detector is obtained by multiplying each spectral estimate by the appropriate filter absorption value, i.e.

$$S_D(E) = S_P(E).F(E) \qquad 4.2$$

where S_D and S_P are the spectral intensities at the detector and plasma respectively, and F is the filtering as a function of the photon energy E. The measured spectrum S_M is then given by the convolution of the instrumental function I with S_D:

$$S_M(E) = \int_0^\infty S_D(E')I(E'-E)dE' \qquad 4.3$$

The instrumental function is a Gaussian, characterised by the full width at half maximum height (FWHM). The FWHM is refered to as the resolution of the system, which for Si(Li) detectors is about 200 eV, depending upon the amplifier characteristics used. To simulate the operation of the MCA, the measured spectrum is summed over energy channels to give the analysed form S_A

$$S_A(E_i) = \sum_{j=ni}^{n(i+1)} S_M(E_j) \qquad 4.4$$

The plasma emission is reconstructed by removing the effect of the absorbers from S_A, creating S_P'

$$S_P'(E_i) = S_A(E_i)/F(E_i^*) \qquad 4.5$$

where E_i^* is some weighted energy representative of the analysis channnel. From S_P' we estimate the electron temperature, using the subroutines described in 4.1.4.3, as a function of the lower bound of the energy range of photons used in the fit, and of the energy weighting scheme employed in the correction procedure. Two weighting schemes were used in these calculations, as extreme examples of the effect of energy channel width upon the reconstruction, by fixing the value of E_i^* as that of the minimum and maximum energies included in the channel i. These are refered to as low and high energy weighting respectively. The effect of these two weightings is illustrated in figures 4.13 and 4.14. The results are explicable in terms of the distribution of measured photons across the width of a channel. At low photon energies (E (1 keV) where the filter is most significant, the measured spectrum is an increasing function of photon energy. Low energy weighting is then an underestimate of the mean energy of the photons grouped in a channel, and so the effect of the filter is overestimated, resulting in an overcorrection. The converse is true for the case of high energy weighting.

The results of this investigation are summarised in figure 4.15. The curves show that accuracy improves as one moves away from the spectral region influenced by the filtering effect of the absorbers. The partition of the high and low weighted curves about the x-axis may be used to estimate a more appropriate value for the energy weighting. This value can be seen to be a function of the electron temperature however, through the influence of the temperature on the gradient of the measured spectrum. In conclusion, an analysis of the data processing procedure shows that errors in the measurement of the electron temperature from the soft x-ray spectrum may be minimised by using narrow energy analysis channels, and by counting high energy photons. Both requirements result in an increased data collection time, since photon collection statistics then become more important.

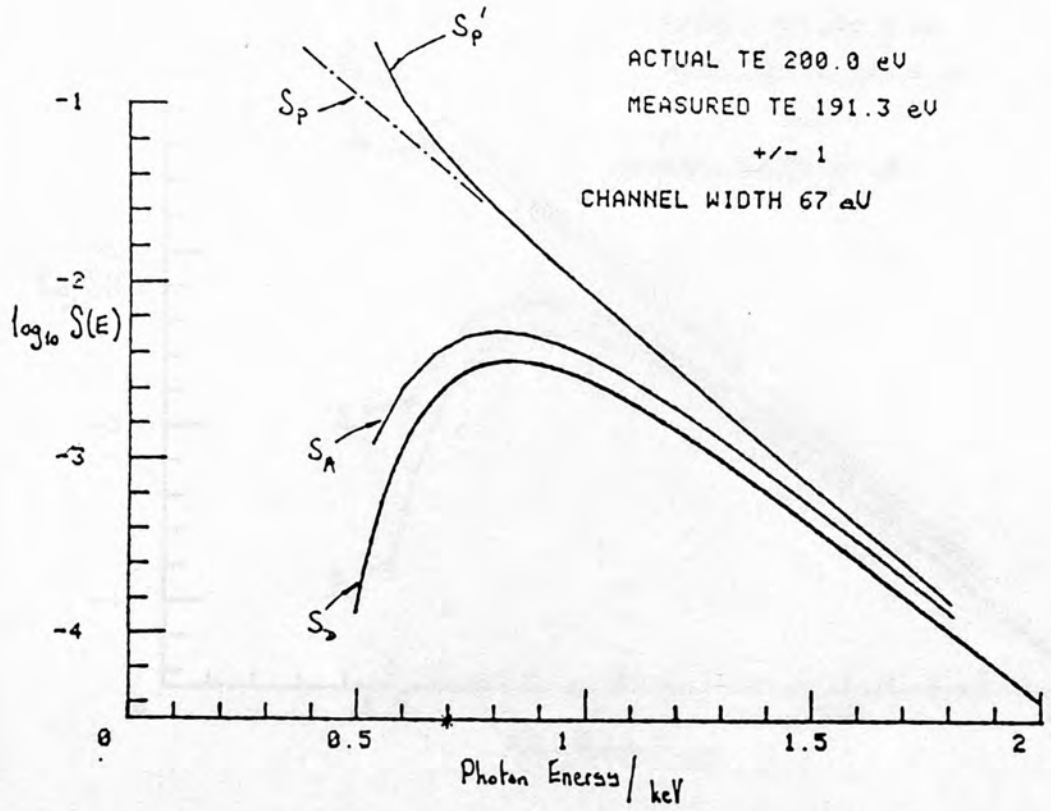

Figure 4.13

Reconstruction of the plasma sof x-ray emission spectrum with low energy weighting. S_D is the filtered spectrum as received by the detector. This is convolved with the detector instrumental function and pulse height analysed to give the spectrum S_A. The reconstructed plasma spectrum S_P' is obtained from S_A by correction for the effect of the absorbers between the detector and the plasma, using a low energy weighting scheme as described in the text. The star on the x-axis indicates the lower bound of the photon energies included in the calculation of the displayed electron temperature from the spectrum S_P'.

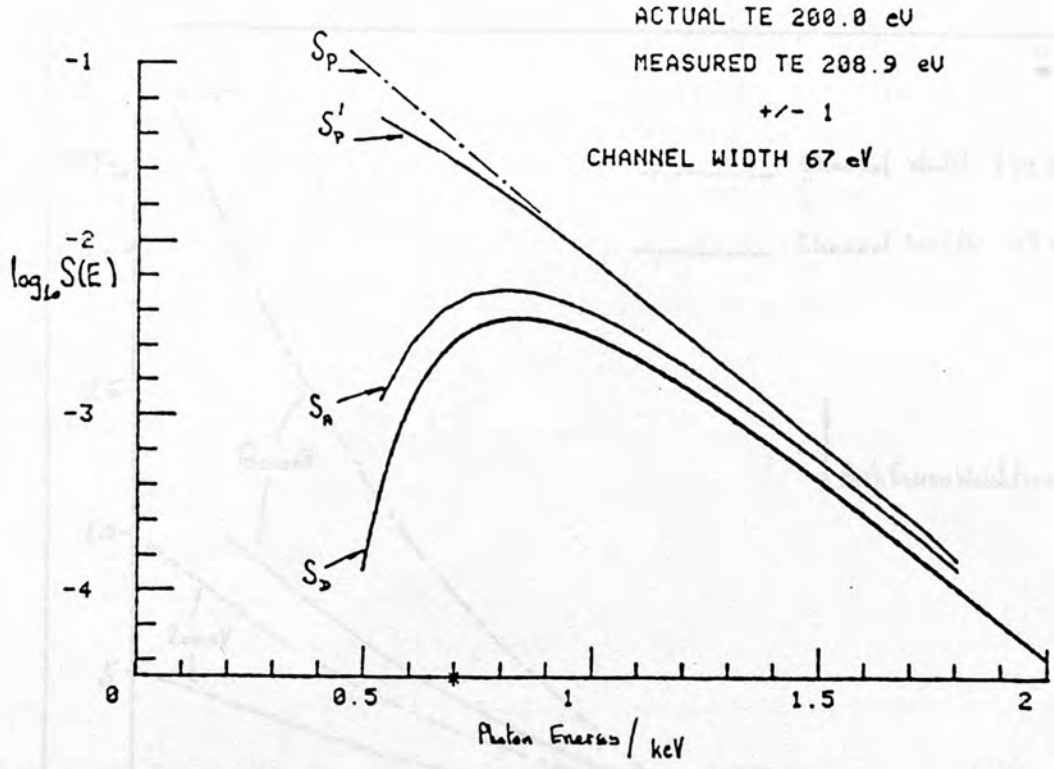

Figure 4.14

Reconstruction of the soft x-ray spectrum with high energy weighting

Calculation of Errors in the Measured Spectrum

The corrected x-ray power spectrum, as presented by the graphic display, is given by

$$\log_{10} S(E) = \log_{10} \frac{E.N(E)}{F(E)} \qquad 4.6$$

where $N(E) = \Delta m / \Delta E$ is the number of counts per channel, and F is the filter transmission function. Equation 4.6 may be written as

$$\log_{10} S(E) = \log_{10} E + \log_{10} N(E) - \log_{10} F(E) \qquad 4.7$$

From section 3.2.3

$$\log_{10} F(E) = \log_{10} [\exp -(x.\rho.\frac{\mu(E)}{\rho})] \qquad 4.8$$

At the energies of interest, the mass absorption coefficient of beryllium is given by the empirical relationship [60]

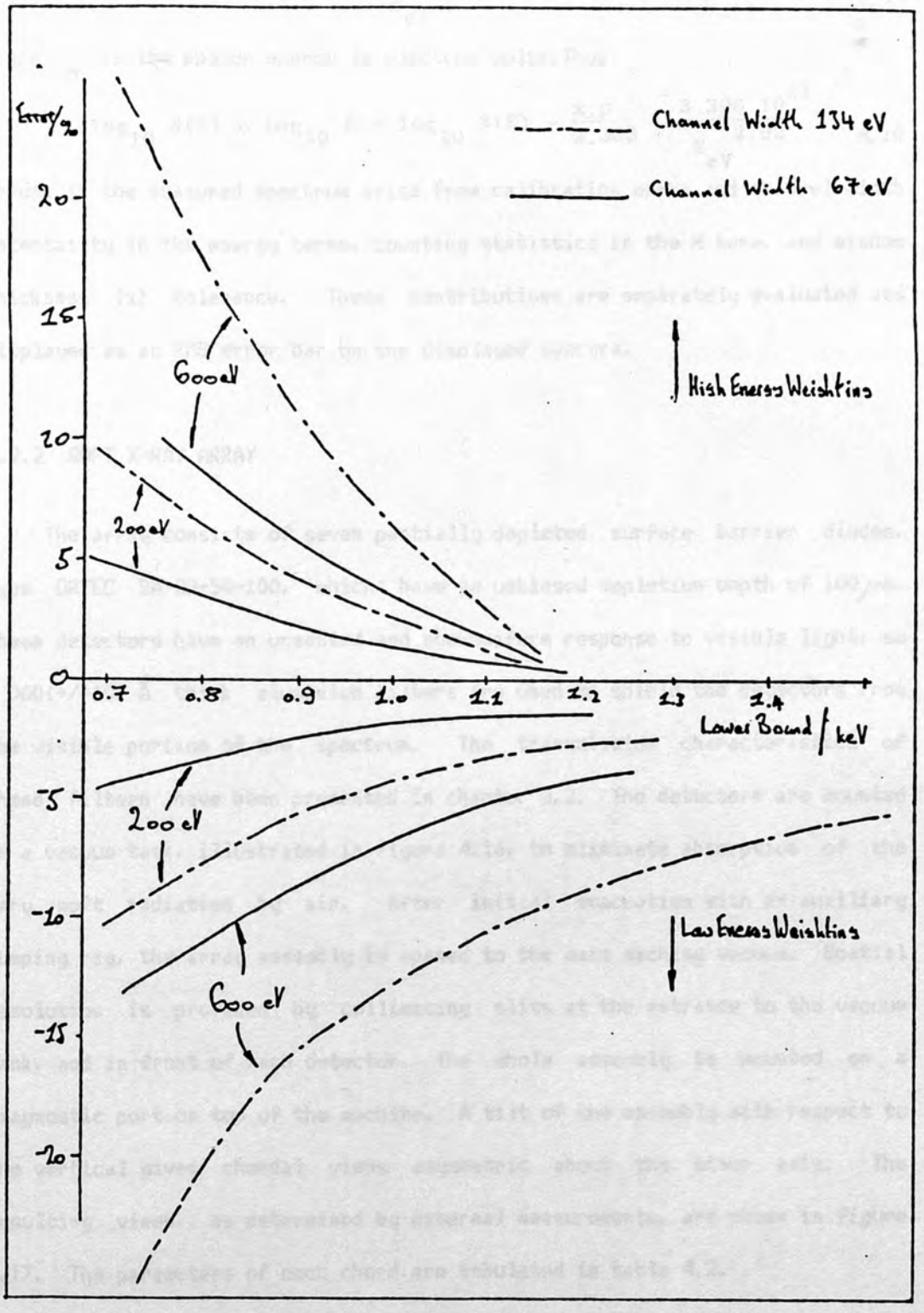

Figure 4.15

Soft x-ray temperature measurement - summary curves

The curves describe the accuracy of the reconstruction of the soft x-ray spectrum as a function of the lower photon energy bound, and of analysis channel width.

$$\frac{\mu(E)}{\rho} = \frac{3.396.10^{11}}{E_{eV}^{2.92}} \quad cm^2.g^{-1} \qquad 4.9$$

where E_{eV} is the photon energy in electron volts. Thus

$$\log_{10} S(E) = \log_{10} E + \log_{10} N(E) + \frac{x.\rho}{2.303} \cdot \frac{3.396.10^{11}}{E_{eV}^{2.92}} \qquad 4.10$$

Errors in the measured spectrum arise from calibration error and channel width uncertainty in the energy terms, counting statistics in the N term, and window thickness (x) tolerance. These contributions are separately evaluated and displayed as an RMS error bar on the displayed spectra.

4.2.2 SOFT X-RAY ARRAY

The array consists of seven partially depleted surface barrier diodes, type ORTEC BA-23-50-100, which have an unbiased depletion depth of 100 μm. These detectors have an unwanted and non-uniform response to visible light, so 2 000(+/-10) Å thick aluminium filters are used to shield the detectors from the visible portion of the spectrum. The transmission characteristics of these filters have been presented in chapter 3.2. The detectors are mounted in a vacuum tank, illustrated in figure 4.16, to eliminate absorption of the very soft radiation by air. After initial evacuation with an auxiliary pumping rig, the array assembly is opened to the main machine vacuum. Spatial resolution is provided by collimating slits at the entrance to the vacuum tank, and in front of each detector. The whole assembly is mounted on a diagnostic port on top of the machine. A tilt of the assembly with respect to the vertical gives chordal views asymmetric about the minor axis. The resulting views, as determined by external measurements, are shown in figure 4.17. The parameters of each chord are tabulated in table 4.2.

Signals from the detectors are fed to high gain (approximately 1 mV/nA) current to voltage amplifiers, situated as close as possible to the detectors. The voltage signals are then routed away from the machine area for recording, either by oscilloscopes, or after further amplification, by analogue to digital converters. In the latter case, Lecroy 8210 4-channel ADC's were

used, controlled by an LSI-11/CAMAC system.

The sensitivity of the x-ray signal from these detectors to variations in the plasma electron temperature and density, and to plasma ionic composition, has been fully discussed in section 3.2.

Detector	Major Radius at Equatorial Plane/cm	Chord Tangent Radius/cm
1	32.9	2.9
2	31.7	1.7
3	30.4	0.4
4	29.1	-0.9
5	27.9	-2.2
6	26.5	-3.4
7	25.2	-4.5

Table 4.2

Soft x-ray array parameters

4.2.3 SINGLE CHANNEL SOFT X-RAY PROBE

The radial information on soft x-ray flux distribution available from the array may be supplemented by that from an additional probe-mounted detector. The probe can be inserted through one of several diagnostic ports around the vacuum vessel, to within a few millimetres of the plasma. The collimator is such that the line of sight to the detector is at an angle to the probe axis, so that a scan across the plasma is afforded by rotation of the probe shaft. The probe head design is sketched in figure 4.18.

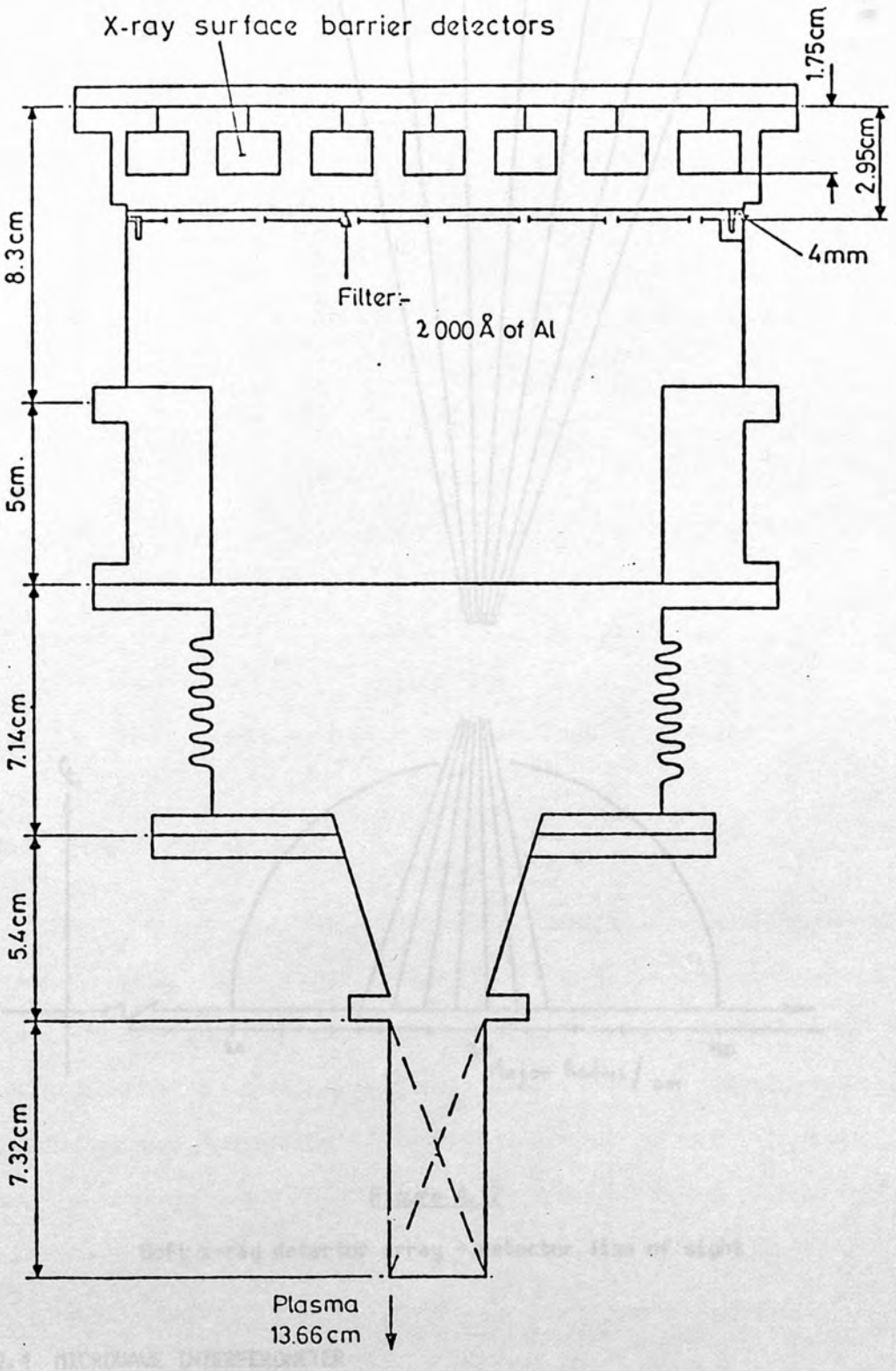

Figure 4.16

Soft x-ray detector array - vacuum assembly

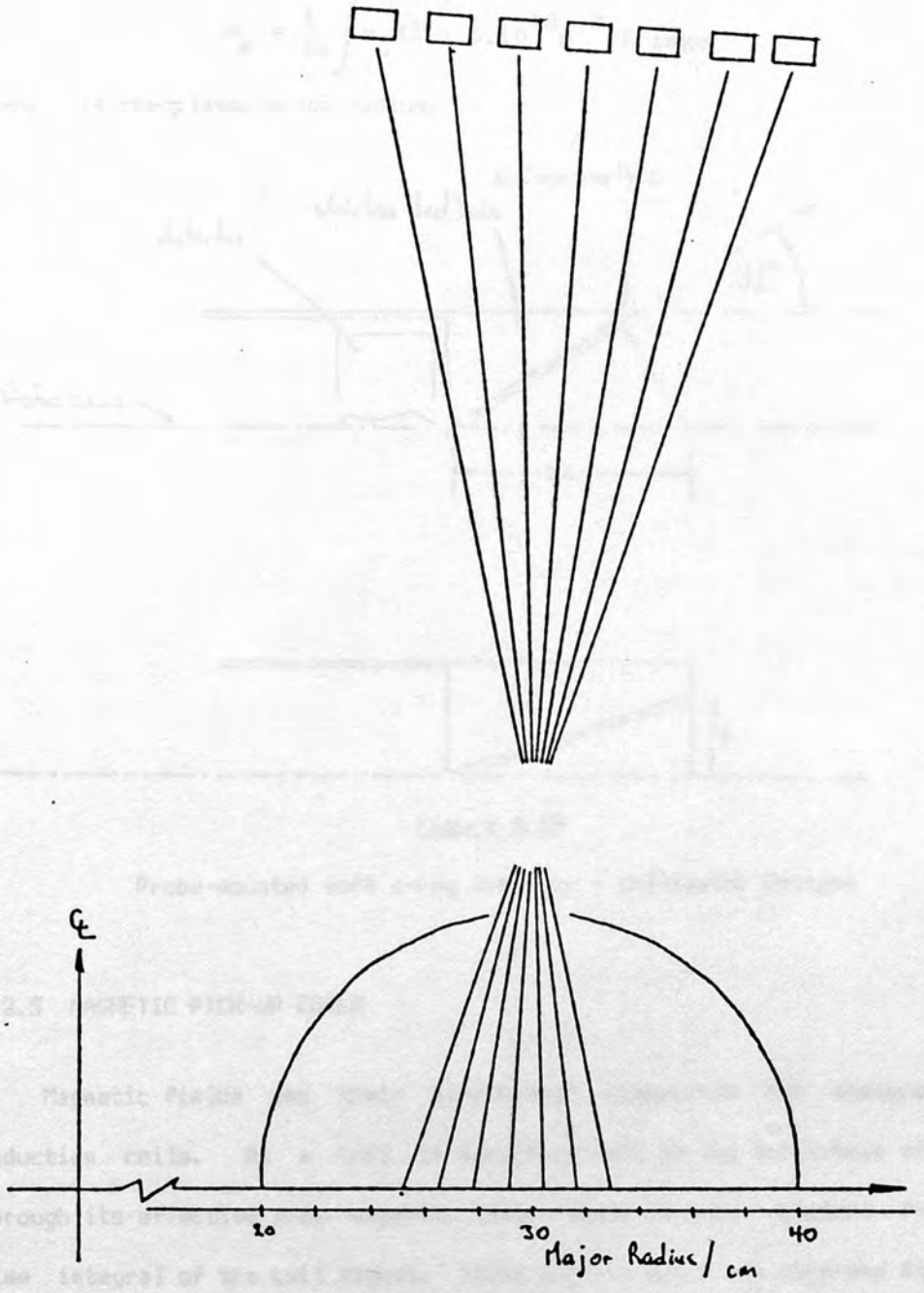

Figure 4.17

Soft x-ray detector array - detector line of sight

4.2.4 MICROWAVE INTERFEROMETER

Mean line-of-sight electron density is measured using a 1.4 mm microwave Michelson interferometer. The microwave beam travels along a vertical chord in the minor cross-section, through the minor axis, and has a calibration of

$$\bar{n}_e = \frac{1}{2a}\int n_e \, d\ell = 5.10^{18} m^{-3}/\text{fringe} \qquad 4.11$$

where a is the plasma minor radius.

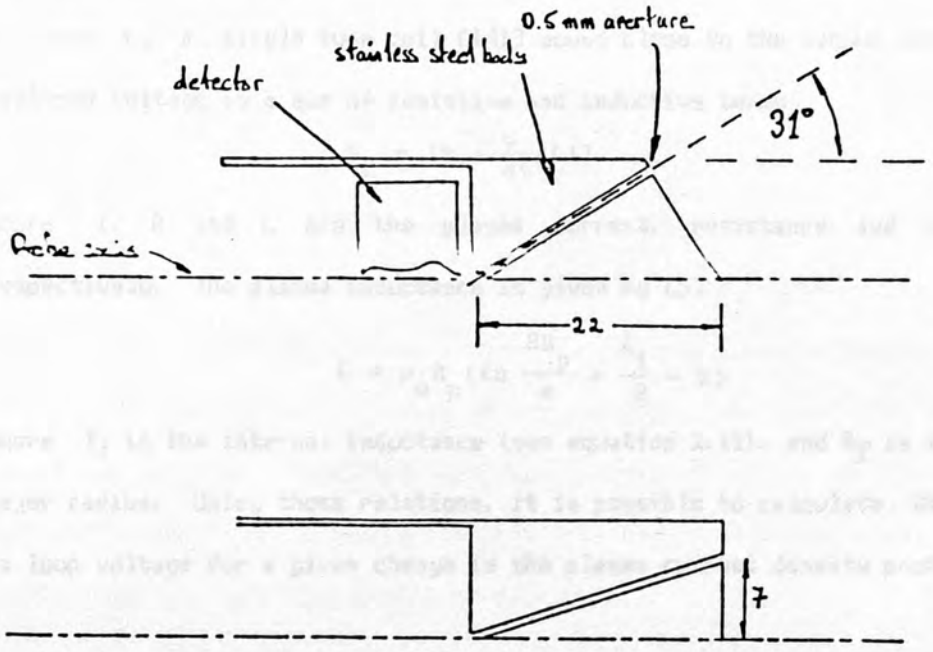

Figure 4.18

Probe-mounted soft x-ray detector - collimator designs

4.2.5 MAGNETIC PICK-UP COILS

Magnetic fields and their directional components are measured with induction coils. As a coil is sensitive only to the derivative of a flux through its effective area, magnetic field values must be obtained from the time integral of the coil signal. Those signals which are recorded digitally may be integrated numerically, but often a passive RC network integrator is used, the output of which is displayed on a scope. The output voltage from an RC integrator is given by

$$V_{OUT} = \frac{1}{RC}\int V_{IN}\, dt - \frac{1}{RC}\int V_{OUT}\cdot dt \qquad 4.12$$

and thus a correction term arises.

4.2.6 PLASMA LOOP VOLTAGE

The loop voltage is the induced voltage per toroidal turn, which may be measured by a single turn coil [141] wound close to the vacuum vessel. The measured voltage is a sum of resistive and inductive terms:

$$V_L = IR + \frac{d}{dt}(LI) \qquad 4.13$$

where I, R and L are the plasma current, resistance and inductance respectively. The plasma inductance is given by [5]

$$L = \mu_o R_p \left(\ell n \frac{8R_p}{a} + \frac{\ell_i}{2} - 2\right) \qquad 4.14$$

where l_i is the internal inductance (see equation 2.11), and R_p is the plasma major radius. Using these relations, it is possible to calculate the change in loop voltage for a given change in the plasma current density profile.

4.2.7 DIAMAGNETIC LOOP

A direct measure of the plasma energy in motion perpendicular to the main field component is given by the so-called diamagnetic loop. The tokamak pressure balance equation in cylindrical geometry is [5]

$$\langle p \rangle = \frac{B_\theta^2}{2\mu_o} + \frac{B_{\phi o}^2}{2\mu_o} - \frac{\langle B_{\phi i} \rangle^2}{2\mu_o} \qquad 4.15$$

$B_{\phi o} - B_{\phi i}$ is the difference in the toroidal field in the presence of a plasma, due to plasma para/dia-magnetism, and $\langle p \rangle$ is the mean plasma pressure. Since the difference in the toroidal field is small, equation 4.15 can be written

$$B_{\phi o}^2 - \langle B_{\phi i} \rangle^2 \cong 2B_{\phi o}\langle B_{\phi o} - B_{\phi i} \rangle = 2B_{\phi o}\frac{\delta\Phi}{\pi a^2} \qquad 4.16$$

where $\delta\Phi$ is the change in toroidal flux in the presence of a plasma. Then

$$\beta_\theta = \frac{2\mu_o \langle p \rangle}{B_\theta^2(a)} \qquad 4.17$$

and

$$\frac{2\mu_o \langle p \rangle}{B_\theta^2(a)} = 1 + \frac{2B_{\phi o}\,\delta\Phi}{B_\theta^2(a).\pi a^2} \qquad 4.18$$

giving

$$\beta_\theta = 1 + \frac{10^{14}}{2\pi}\frac{B_{\phi o}}{I_p^2}\,\delta\Phi \qquad 4.19$$

This is, however, a difficult measurement to make, as $\delta\Phi$ is rather small, and

must be measured in the presence of relatively large fields and voltages.

4.3 THE ECRH SYSTEM

The ECRH system as currently implemented consists of a single gyrotron tube, manufactured by the Varian Corporation of the USA, who claim a performance of up to 200 kW for 10 ms at 28 GHz, with a duty cycle of 1% and a bandwidth of 0.1%. The microwave power is routed to the torus in a circular copper waveguide of 2.5" diameter, where the principle mode of propagation is TE_{01}. Mode conversion at changes in the waveguide direction (with subsequent power loss through breakdown) has been found to be a problem in the past [155], and the RF power is routed to the torus via two straight waveguide sections and a single right-angle bend.

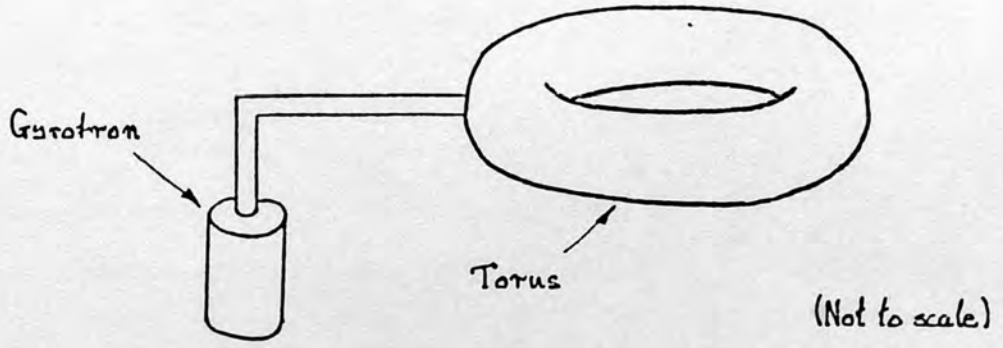

Figure 4.19

RF power feed to the torus

The torus vacuum is maintained by use of a re-entrant probe type antenna, with beryllia windows at both gyrotron cavity and probe ends of the waveguide. The open-ended antenna is merely an extension of the waveguide, and is inserted so as to be flush mounted with the wall of the vacuum vessel. The emergent wave vector is essentially perpendicular to the plasma magnetic field. The nature of the resulting power distribution in the torus has been calculated by Fielding [15], as discussed in section 2.2.1.

4.4 SUMMARY

The status of the TOSCA tokamak may be summarised as follows. The vacuum vessel of the machine has been modified to permit the injection of very high power microwaves from a gyrotron device, launched from an open ended waveguide flush with the vacuum vessel wall. The maximum gyrotron output power exceeds the normal Ohmic heating rate in TOSCA by more than a factor of ten. The 28 GHz operating frequency of the gyrotron thus allows high power electron cyclotron resonance heating experiments at the second harmonic of the ECR. Plasma diagnostics are available for the study of the effects of ECRH on both the local and integral plasma conditions, and on the electron velocity distribution function.

CHAPTER 5 THE ELECTRON TEMPERATURE DISTRIBUTION IN TOSCA

The principles of electron cyclotron heating in the tokamak have been discussed in chapter 2, where it was shown that appreciable heating rates might occur. In particular, the method of applying second harmonic ECRH to TOSCA was described, with the necessary hardware arrangement being outlined in chapter 4. Before examining the heating results obtained, it is first necessary to describe the measurements made on the ohmically heated TOSCA plasmas. These data are used in an evaluation of the electron temperature spatial profile, an approach which provides a basis for a discussion of the ECRH results presented in the next chapter. Profile related measurements were made as follows:

- o measurement of the plasma electric and magnetic properties,
- o measurement of the soft x-ray emission spatial profile,
- o measurement of the soft x-ray emission energy spectrum.

Using the information from these measurements, an electron temperature profile was determined with the aid of calculations of:

- o the principal electrical and magnetic properties of the discharge,
- o the soft x-ray flux signal profile.

This procedure of a combined experimental and calculational nature is necessary for the determination of a two-dimensional distribution from measurements using diagnostics with resolution in at best one dimension. Of the diagnostics available on TOSCA, only the soft x-ray measurements were able to provide any spatially resolved measurements across the plasma profile. Consequently, it was necessary to take profile information from measurements performed on other tokamaks of similar size and performance. With these profiles as likely representations of the spatial distributions in TOSCA,

temperature and density profiles can be determined by comparing the calculated with observed performance as determined by measurements of plasma current, density, poloidal-beta and other quantities, as described in section 5.1.

5.1 MEASUREMENTS TO DETERMINE SPATIAL PROFILES

In view of the expected localisation of the ECRH, and the spatially resolved nature of the soft x-ray measurements, it became of interest to determine the plasma profiles of temperature and density in minor cross-section, both with and without supplemental heating.

Some information is available from previous measurements on TOSCA. Thomson scattering experiments in relativly high current (12 kA) discharges indicated a peak temperature in excess of 300 eV [66]. No previous Z-effective profile measurements have been conducted on TOSCA, but crystal spectrometer studies revealed a complete absence of metallic (high-Z) impurities [144], indicating that low values of effective ionic charge were to be expected.

5.1.1 MEASUREMENT OF THE PLASMA ELECTRICAL AND MAGNETIC PROPERTIES

The following sections of this chapter report the results of measurements, under ohmic heating, on that portion of the TOSCA plasma where ECRH experiments were carried out. Basic electrical and magnetic characteristics (e.g. V_L, I_p, B_ϕ) are routinely measured on TOSCA, using the diagnostics described in 4.2. The following ohmic plasma parameters apply to all the following measurements, unless otherwise stated to the contrary.

$V_L = 2$ V

$I_p = 7.5 - 8$ kA

$B_\phi = 0.5 - 0.55$ T

$t = 1.5 - 2.0$ ms, timed from primary E-bank firing

$\beta \sim 0.5$

$\bar{n}_e = 5 - 7.5 \times 10^{18}$ m^{-3}

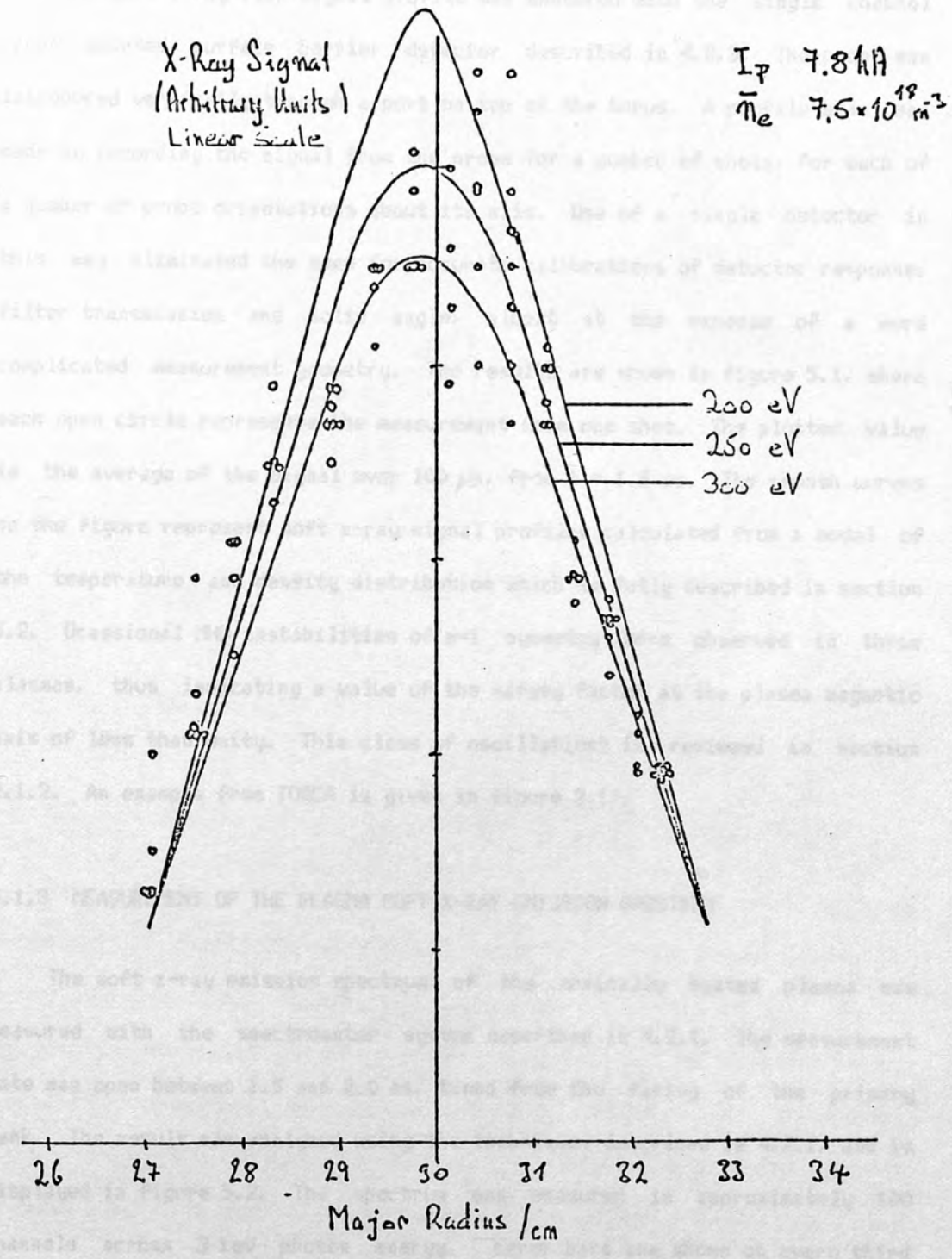

Figure 5.1

Soft x-ray signal profile, showing in addition calculated profiles for central temperatures of 200, 250, and 300 eV.

5.1.2 MEASUREMENT OF THE PLASMA SOFT X-RAY EMISSION PROFILE

The soft x-ray flux signal profile was measured with the single channel probe mounted surface barrier detector described in 4.2.3. The probe was introduced vertically through a port on top of the torus. A profile scan was made by recording the signal from the probe for a number of shots, for each of a number of probe orientations about its axis. Use of a single detector in this way eliminated the need for accurate calibrations of detector response, filter transmission and solid angle, albeit at the expense of a more complicated measurement geometry. The results are shown in figure 5.1, where each open circle represents the measurement from one shot. The plotted value is the average of the signal over 100 μs, from t = 1.5 ms. The smooth curves on the figure represent soft x-ray signal profiles calculated from a model of the temperature and density distribution which is fully described in section 5.2. Ocassional MHD instabilities of m=1 symmetry were observed in these plasmas, thus indicating a value of the safety factor at the plasma magnetic axis of less than unity. This class of oscillations is reviewed in section 2.1.2. An example from TOSCA is given in figure 3.17.

5.1.3 MEASUREMENT OF THE PLASMA SOFT X-RAY EMISSION SPECTRUM

The soft x-ray emission spectrum of the ohmically heated plasma was measured with the spectrometer system described in 4.2.1. The measurement gate was open between 1.5 and 2.0 ms, timed from the firing of the primary bank. The result was analysed using the techniques described in 4.2.1, and is displayed in figure 5.2. The spectrum was measured in approximately 100 channels across 3 keV photon energy. Error bars are shown on every third channel. The fitted line is calculated according to a least squares criterion, and the displayed error figure is that error returned by this process. The systematic error for this measurement condition, as calculated in 4.2.1, and displayed in figure 4.15, is less than 5 %. As discussed in

4.2.1.4, the spectrum gives a measure of the central electron temperature. The result here is 310 eV, with an error of 45 eV.

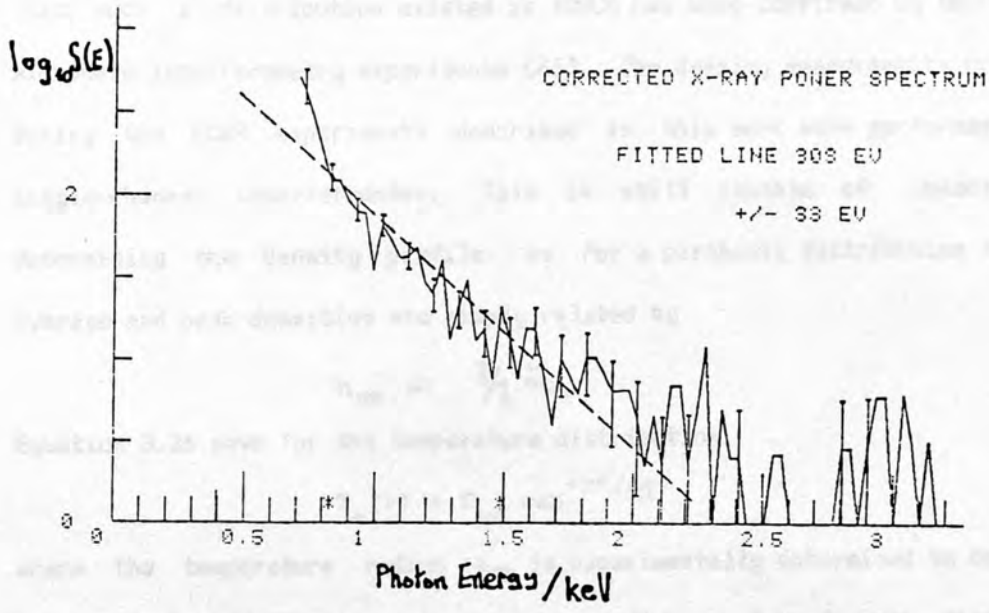

Figure 5.2

Power spectrum of the soft x-ray emission from TOSCA

5.2 CALCULATIONS TO DETERMINE THE TEMPERATURE PROFILE

Two-dimensional spatial profiles cannot (in general) be uniquely determined by diagnostic measurements with zero (e.g. plasma current) or sparse one-dimensional (e.g. the soft x-ray detector array) spatial resolution. Described in this section are calculations on models of the spatial distributions of plasma electron density and temperature characteristic of the tokamak. The basic form of these profiles is taken to be those which have been consistly measured on tokamaks similar to TOSCA, and having diagnostics with full spatial resolution, as reviewed in 3.2.3. These calculations are used to help determine the spatial profiles in TOSCA, by seeing how computed plasma properties can be made to match experimental observations, by adjustment of the parameters defining the profile.

Recalling equation 3.25, experiments have found the following expression to be descriptive of tokamak electron density distributions:

$$n_e(r) = n_{eo}(1 - r^2/a^2) \qquad 5.1$$

That such a distribution existed in TOSCA has been confirmed by two-channel microwave interferometry experiments [66]. The density measurements conducted during the ECRH experiments described in this work were performed with a single-channel interferometer. This is still capable of unambiguously determining the density profile, as for a parabolic distribution the line average and peak densities are simply related by

$$n_{eo} = 3/2\ \bar{n}_e \qquad 5.2$$

Equation 3.26 gave for the temperature distribution

$$T_e(r) = T_{eo}\ \exp^{-r^2/a_T^2} \qquad 5.3$$

where the temperature radius a_T is experimentally determined to be in the range 0,47 - 0,53 times the plasma minor radius a for devices similar to TOSCA. By working through the following calculations, an attempt is made to find values of this radius and central electron temperature which account for the observed properties noted in 5.1.

The current density is calculated as a function of radius from the temperature profile using the Spitzer [10] resistivity

$$\eta_{\parallel} = 6.53 \times 10^{-5}\ Z_{eff}\ \ell n\ \Lambda\ T_{eV}^{3/2}\ \ \Omega.m \qquad 5.4$$

for a fairly typical loop voltage of 2 V, a presumed Z-effective of 2, and uniform electric field. The term ln(lamda) is the Coulomb logarithm, evaluated according to reference [163], and electron temperature is expressed in electron volts. Total plasma current is simply calculated

$$I = \int \underline{j}.\underline{dS} \qquad 5.5$$

that is, the current density integrated over the minor cross-section. The mean conductivity temperature is calculated from

$$T_\sigma^{3/2}/eV = \frac{2R_p I}{a^2 V_L}\ .\ 6.53 \times 10^{-5} Z_{eff}\ \ell n\ \Lambda \qquad 5.6$$

The assumption of a parabolic density profile allows the calculation of the

thermal energy per unit length, defined as

$$W = \frac{3}{2}k\int nT\ dS \qquad 5.7$$

and the energy temperature

$$T_E = \int nT\ dS / \int n\ dS \qquad 5.8$$

where

$$T = T_e + T_i \qquad 5.9$$

T_i being the ion temperature and k is Boltzmann's constant. The peak ion temperature is estimated from the Artsimovitch [145] ion temperature formula, which gives a scaling by balancing ion Coulomb heating against neo-classical losses.

$$T_i = (5.9 \pm 0.5) \times 10^{-7} (IHR^2\bar{n})^{1/3} A^{-1/3}\ eV \qquad 5.10$$

H is the toroidal field strength in Gauss, R is the plasma major radius in cm, n is the mean electron density in cm^{-3}, and A is the ion atomic weight. The value of on-axis ion temperature found for the ECRH experiments is in the range 30 - 35 eV. With this value in mind, and with Z-effective certainly greater than unity, thus causing the electron density to be greater than the ion density, the ion contribution to total thermal energy may be neglected. The streaming parameter, defined as the ratio of electron drift (v_d) to thermal (v_{th}) speeds is also evaluated as function of radius, from

$$V_D = \frac{j}{n_e e} \quad ; \quad V_{th} = \left(\frac{2kT_e}{m_e}\right)^{\frac{1}{2}} \qquad 5.11$$

From the current density distribution, and in cylindrical geometry, it is possible to calculate the poloidal field profile from

$$B_\theta(r) = \frac{\mu_o}{2\pi r} \int_o^r j.2\pi r'.dr' \qquad 5.12$$

from which may be deduced the internal inductance per unit length

$$\ell_i = \frac{1}{\pi a^2\ B_\theta^2(a)} \int B_\theta^2\ dS \qquad 5.13$$

Poloidal-beta is calculated from

$$\beta_\theta = \frac{2\mu_o}{a^2 \pi B_\theta^2 (a)} \int nkT \, dS \qquad 5.14$$

The safety-factor profile is obtained from the poloidal field, after equation 2.8. In the sense of agreement between these calculations and the corresponding measurements described in 5.1, the best temperature profile was given by that defined by

$$a_T = 0.53a \; ; \; T_{eo} = 250 \text{ eV} \qquad 5.15$$

The temperature radius is thus close to that value derived from laser scattering measurements on TM-3 [69]. This profile, and the quantities derived from it, is shown in figure 5.3. As a furthur consistency check, this temperature profile was used in a calculation of the soft x-ray flux profile for comparison with the experiment described in section 5.1.2. Full account was taken of the measurement geometry, detector and filter characteristics, as described in chapter 3. The result of the calculation, for central temperatures of 200, 250, and 300 eV, is superimposed upon the measured points displayed in figure 5.1. A central temperature in the region 250 - 300 eV is indicated. Some asymmetry of the measured x-ray profile is evident, probably due to toroidal effects on the equilibrium distribution of temperature and density, or to non-uniform Z-effective profiles. This measurement is unable to separate Z-effective and temperature profile effects (see section 3.2), though as one might expect Z-effective to decrease with radius (at least near the plasma core) from ionisation equilibrium considerations, the deduced central temperature value may be the lower bound of the true value. (Recall that both a peaked Z-effective profile, and a smaller on-axis temperature give rise to a more peaked soft x-ray emission signal profile). Such Z-effective behaviour has been reported from experiments on PLT [132], and on the JIPP T-II [146] tokamaks.

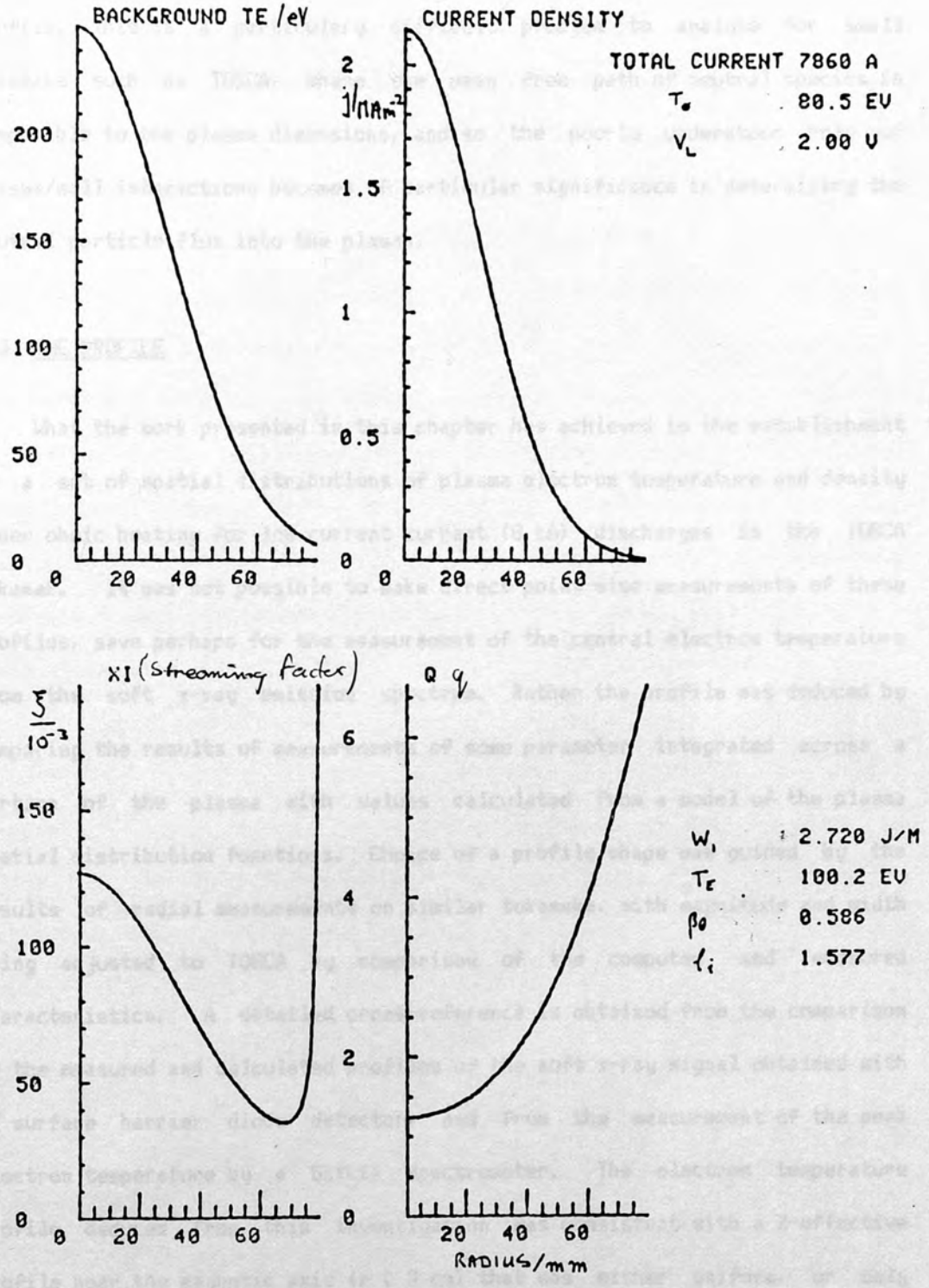

Figure 5.3

Computed profile characteristics at $\bar{n}_e = 7.5 \times 10^{18}$ m^{-3}

It should be noted that the available diagnostics have permitted very little input to the matter of deciding the value of Z-effective and its profile. This is a particulary difficult problem to analyse for small tokamaks such as TOSCA, where the mean free path of neutral species is comparable to the plasma dimensions, and so the poorly understood role of plasma/wall interactions becomes of particular significance in determining the neutral particle flux into the plasma.

5.3 THE PROFILE

What the work presented in this chapter has achieved is the establishment of a set of spatial distributions of plasma electron temperature and density under ohmic heating for low current current (8 kA) discharges in the TOSCA tokamak. It was not possible to make direct point-wise measurements of these profiles, save perhaps for the measurement of the central electron temperature from the soft x-ray emission spectrum. Rather the profile was deduced by comparing the results of measurements of some parameter integrated across a portion of the plasma with values calculated from a model of the plasma spatial distribution functions. Choice of a profile shape was guided by the results of radial measurements on similar tokamaks, with magnitude and width being adjusted to TOSCA by comparison of the computed and measured characteristics. A detailed cross-reference is obtained from the comparison of the measured and calculated profiles of the soft x-ray signal obtained with a surface barrier diode detector, and from the measurement of the peak electron temperature by a Si(Li) spectrometer. The electron temperature profile deduced from this investigation was consistent with a Z-effective profile near the magnetic axis ($r < 3$ cm) that was either uniform, or only slowly decreasing with plasma radius. The profile forms quoted in section 5.2 are consistent, to within reasonable error, with the measurements described in section 5.1. They are furthermore very similar to those determined by pointwise spatial measurements in the Soviet tokamak TM-3 [69]. The profiles

are also consistent with observations in a more qualitative sense. Firstly, rather high values of the streaming parameter are calculated (equation 5.11, exceeding 10 % on axis). This is reflected in the soft x-ray spectrum, where some departure from an ideal maxwellian distribution may be discerned. This behaviour is comparable with that found on other machines. The electron distribution function has been studied as a function of the streaming parameter in the Alcator [147,148,150] and FT [149] tokamaks, using soft x-ray spectra, electron cyclotron emission, and Thomson scattering diagnostics. Non-thermal distributions were apparent in each case for streaming parameters exceeding 3 %. Secondly, the calculated safety factor profile, with q(0) near to unity, is consistent with the observed MHD characteristics of the plasmas here under discussion. It has been established that the ions contribute negligibly to the plasma energetics. This profile is used in chapter 6 in an analysis of the observations of auxiliary heating experiments performed on this plasma condition in TOSCA.

CHAPTER 6 THE EFFECT OF ECRH ON THE TEMPERATURE PROFILE

High power resonance heating at the second harmonic of the electron cyclotron resonance has been applied to the TOSCA tokamak, using the principles outlined in chapter 2. In chapter 5, the nature of the ohmically heated plasma in TOSCA was determined in terms of the spatial distribution of electron temperature and density. The first part of this chapter presents detailed measurements of the effects of auxiliary plasma heating on this plasma profile, using a 200 kW gyrotron for high power second harmonic ECRH. New spatially resolved soft x-ray flux measurements reveal strong localised heating. Results are obtained on the spatial, magnetic field strength, and RF power dependence of the observed effects. Also described is the influence of ECRH on the electron velocity distribution function, as evidenced by a distortion in the spectrum of the continuum soft x-ray emission, and an auxiliary heating induced instability is reported.

In the second part of this chapter, the techniques used for the elucidation of the temperature profile of the ohmic plasma in chapter 5, together with the characteristics of the soft x-ray flux monitoring diagnostic calculated in chapter 3, are further applied in order to determine the effect of ECRH upon the temperature profile. The experimental data from the ECRH experiments reported in 6.1 are reduced to the form of local electron temperature profiles for comparison with the theoretical predictions of energy absorption from the microwave field presented in chapter 2.

6.1 OBSERVATIONS OF ECRH IN TOSCA

For the first time, spatially resolved observations have been made of high power heating at the second harmonic of the electron frequency in a tokamak. In this section are presented measurement results from a seven channel soft x-ray detector array and other diagnostics.

6.1.1 SPATIAL AND FIELD STRENGTH DEPENDENCE

The localisation of heating by ECRH is immediately apparent from figure 6.1, which shows the profile of the soft x-ray emission for an ohmically heated plasma, and for the same plasma with ECRH at 50 and 150 kW RF power. This profile was obtained using the soft x-ray array diagnostic described in section 4.2.2. Each plotted point represents the average, over 5 - 10 plasma shots, and over a period of 200 μs, of the soft x-ray signal from each detector of the array.

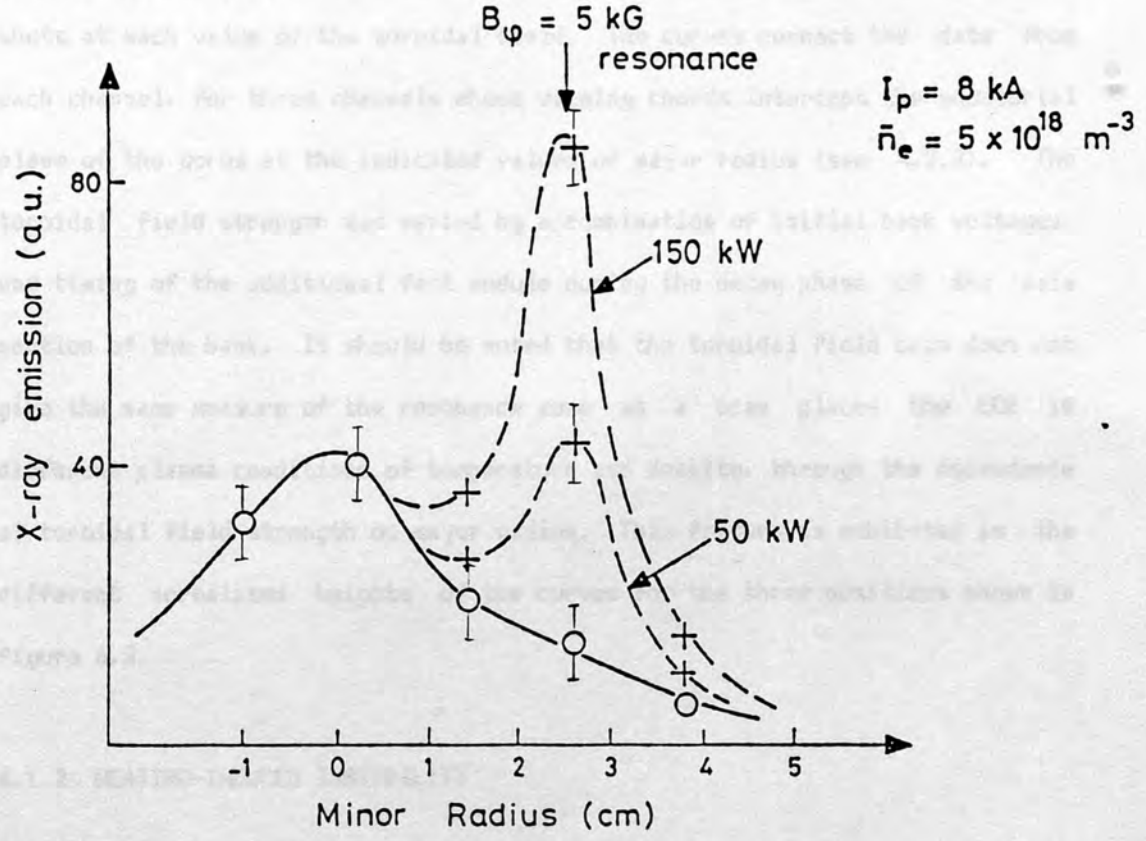

Figure 6.1

Observed soft x-ray emission profile for an ohmically heated discharge (full line), and for a discharge with ohmic and ECR heating (broken line).

The figure also shows the asymmetry of the heating effect, in that the soft x-ray signal is affected only on the outer half of the radial profile. This was a consistent feature of all the ECRH experiments conducted on TOSCA.

Figure 6.1 also shows that the heating effect of the ECRH is limited to a region 10 - 20 mm in width. This resonance zone size has been calculated in section 2.2.1, where a width of 5 mm determined by the Doppler broadening of the ECR was found.

Further profile width information is given figure 6.2, which shows the positional shift of the resonance position, as seen by the heating effect observed on the soft x-rays, as a function of the strength of the toroidal field component. The plotted points were averaged as above, over 5 to 10 shots at each value of the toroidal field. The curves connect the data from each channel, for three channels whose viewing chords intercept the equatorial plane of the torus at the indicated values of major radius (see 4.2.2). The toroidal field strength was varied by a combination of initial bank voltages, and timing of the additional fast module during the decay phase of the main portion of the bank. It should be noted that the toroidal field scan does not give the same measure of the resonance zone as a scan places the ECR in different plasma conditions of temperature and density, through the dependence of toroidal field strength on major radius. This feature is exhibited in the different normalised heights of the curves for the three positions shown in figure 6.2.

6.1.2 HEATING-INDUCED INSTABILITY

The soft x-ray signal frequently exhibits temporal variation on top of the main heating effect. The radial structure of this oscillation as determined from four viewing chords of the soft x-ray array diagnostic (see 4.2.2) is illustrated in figure 6.3. With such a limited number of views through the region of interest a detailed analysis of this feature is difficult, but from the information available some features of $m = 1$ symmetry, for example phase inversion, are apparent. There is a threshold RF power level associated with the onset of oscillation, which would be consistent with

the need for the heating to lower the local value of the safety factor below some stability limit. This power level is in the range ⟨ 20 - 100 kW.

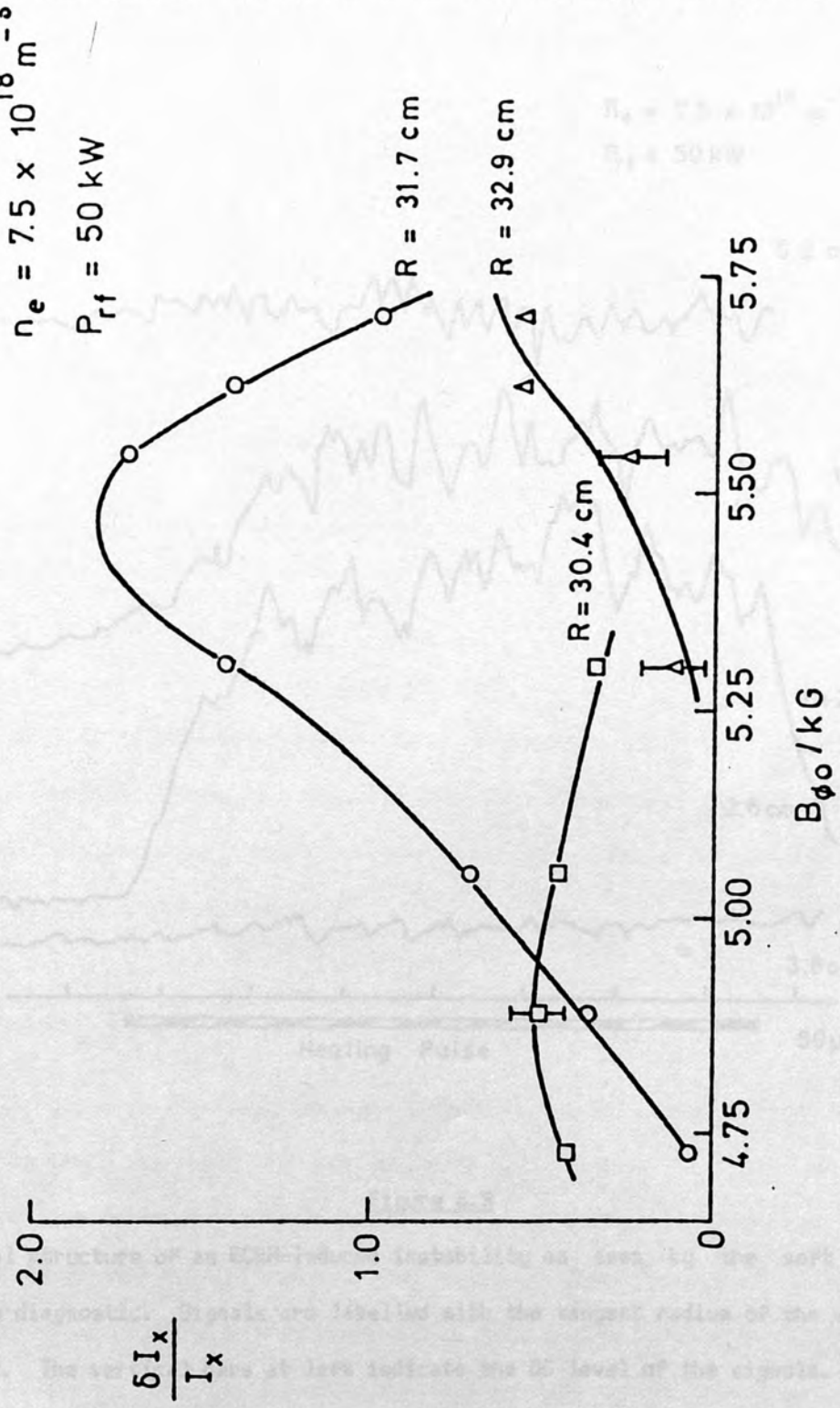

Figure 6.2

ECRH profile by toroidal field scan, as exhibited three soft x-ray flux signal channels, as a function of the toroidal field component.

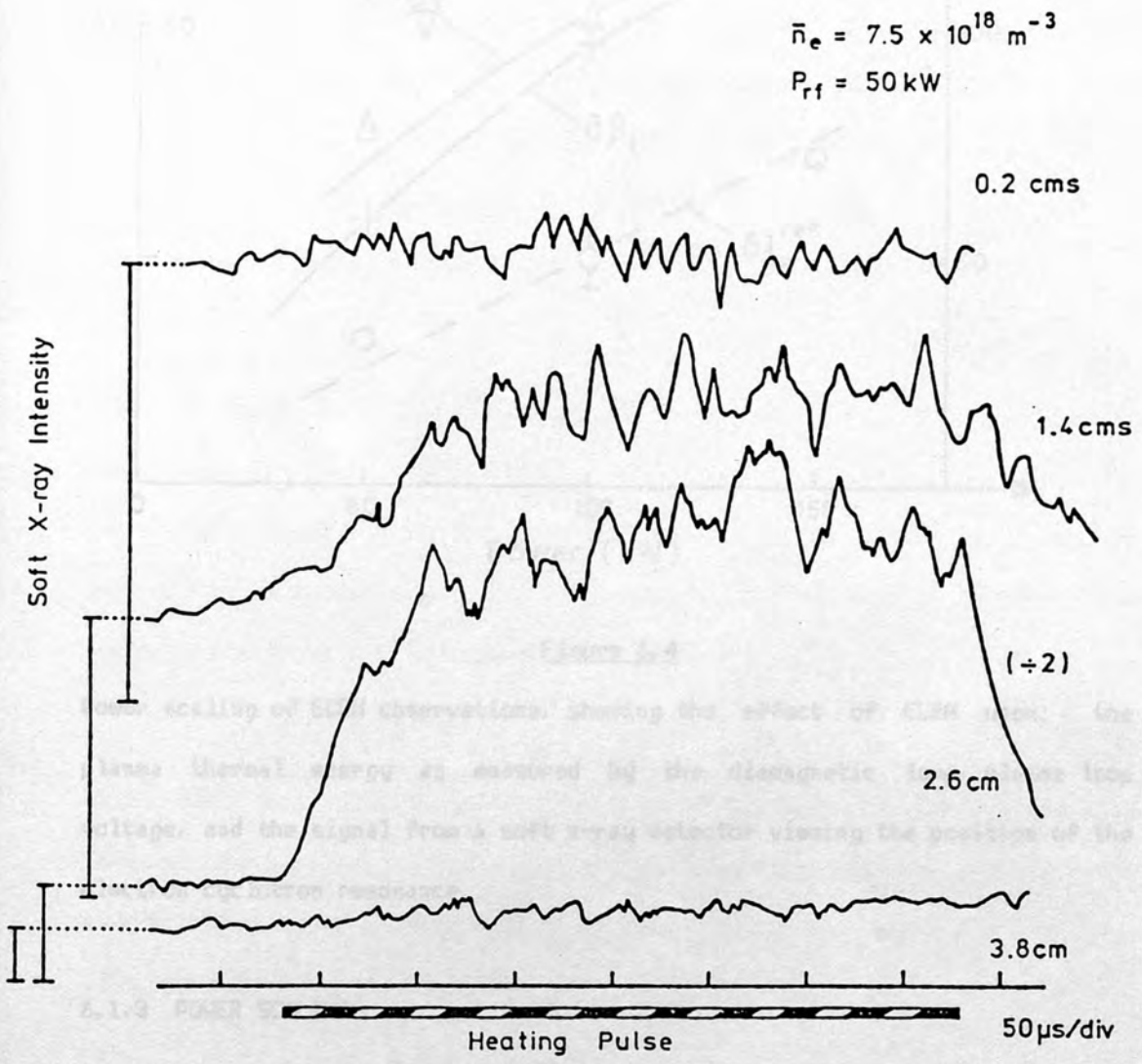

Figure 6.3

Radial structure of an ECRH-induced instability as seen by the soft x-ray array diagnostic. Signals are labelled with the tangent radius of the viewing chord. The vertical bars at left indicate the DC level of the signals. Each tick-mark on the horizontal axis represents 50 μs.

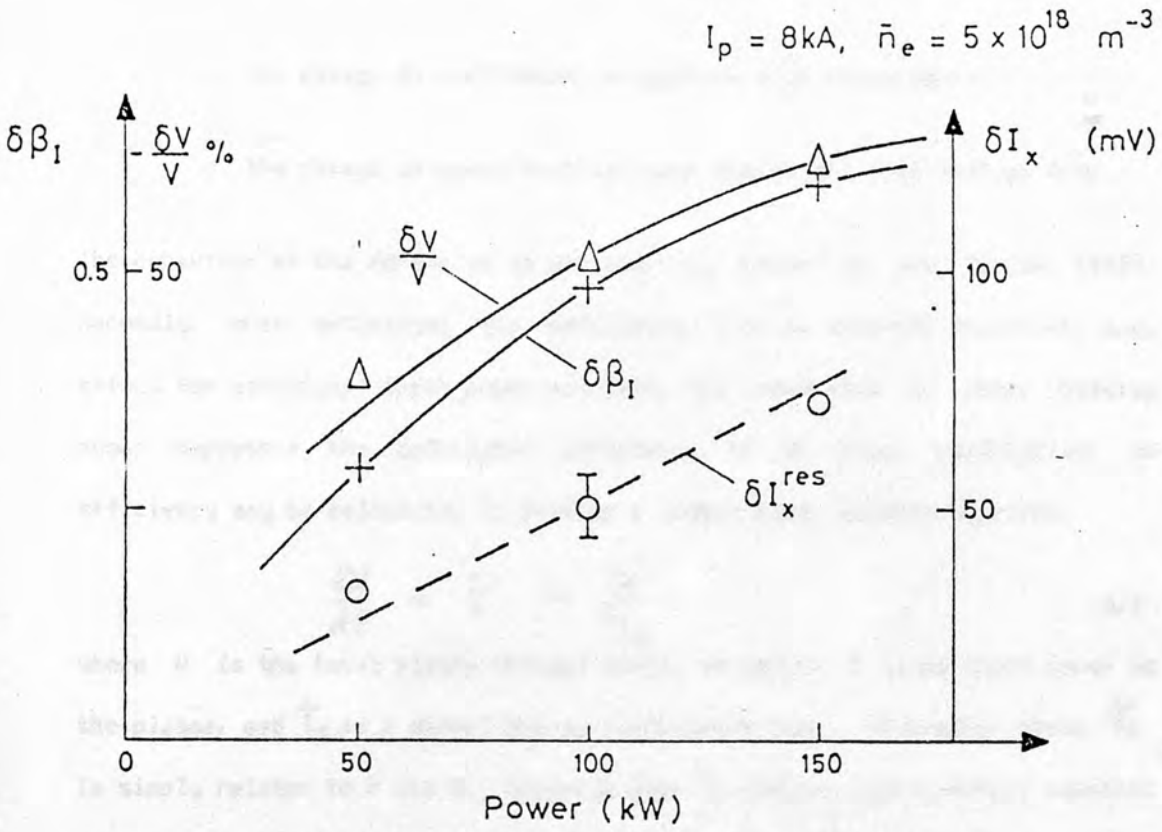

Figure 6.4

Power scaling of ECRH observations, showing the effect of ECRH upon: the plasma thermal energy as measured by the diamagnetic loop, plasma loop voltage, and the signal from a soft x-ray detector viewing the position of the electron cyclotron resonance.

6.1.3 POWER SCALING

The dependence on gyrotron output power of the soft x-ray signal viewing the resonance position is shown in figure 6.4. Also shown is the fractional loop voltage decrease, and poloidal-beta as measured by the diamagnetic loop. The relative loop voltage and beta show a similar rate of increase with power, but may be approaching a saturation level. It would be of interest to convert these figures into an estimate of the efficiency of the utilisation of the available RF power. In doing this, two factors need to be taken into account:

- the change in confinement properties with temperature,

- the change in ohmic heating power due to the loop voltage drop.

The behaviour of the former is as yet scarcely known in the tokamak [162]. Secondly, when estimating the efficiency from an external viewpoint, i.e. effect for additional input power provided, the reduction in ohmic heating power depresses the calculated efficiency of RF power utilisation. An efficiency may be calculated by writing a global power balance equation:

$$\frac{dW}{dt} = P - \frac{W}{\tau_E} \qquad 6.1$$

where W is the total plasma thermal energy as before, P is he input power to the plasma, and τ_E is a global energy confinement time. At steady state, τ_E is simply related to P and W. Assuming that τ_E remains approximately constant when the RF power is turned on, the RF heating efficiency emerges from equating the ohmic and ECRH cases of equation 6.1.

$$\frac{\beta_{OH}}{P_{OH}} = \frac{\beta_{ECRH}}{P_{OH} + \eta P_{ECRH}} \qquad 6.2$$

where beta has been substituted for W, as at constant plasma current (and hence constant poloidal field at the plasma boundary), the two are linearly related (see equation 5.14). From equation 6.2, efficiencies of 22, 16, and 13 % are calculated powers of 50, 100, and 150 kW.

6.1.4 OVERVIEW OF AN ECRH DISCHARGE

The effect of ECRH on the plasma may be seen very clearly in figure 6.5, an overview of an ECRH shot, as given by the primary diagnostics. The figure shows the temporal behaviour of the plasma loop voltage, one soft x-ray channel, second harmonic electron cyclotron emission, plasma horizontal emission, and plasma current. That ECRH produces a noticeable effect on the first four of these diagnostics is clear. The rise in the plasma current mid-way through the gyrotron pulse is not a result of ECRH; at this time an additional E-bank is fired to assist in controlling the plasma position.

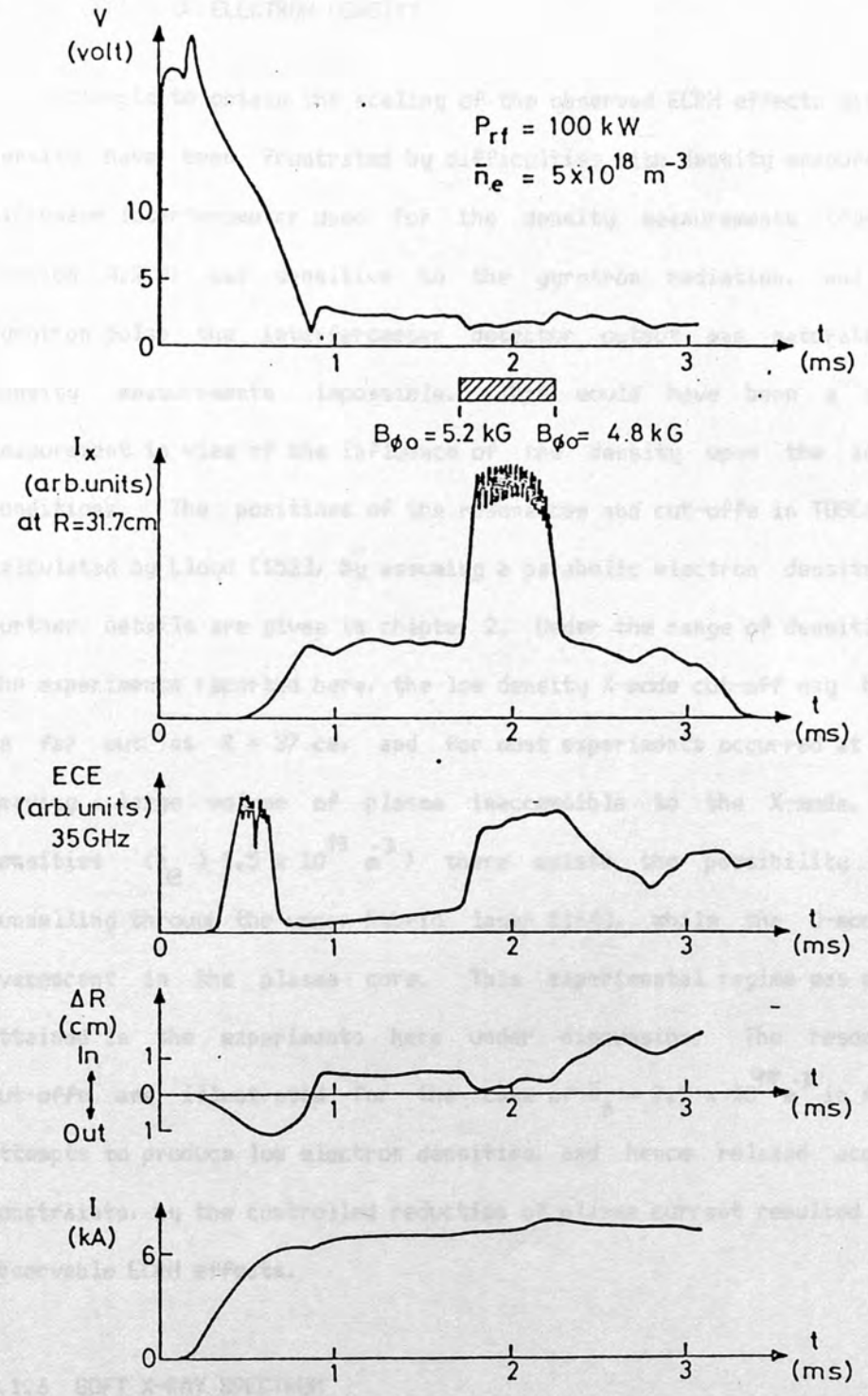

Figure 6.5

Overview of ECRH shot, as seen on loop voltage, soft x-ray emission from the region of the ECR, second harmonic ECE, plasma horizontal position and plasma current. The hatched area indicates the duration of the gyrotron pulse.

6.1.5 EFFECT OF ELECTRON DENSITY

Attempts to obtain the scaling of the observed ECRH effects with electron density have been frustrated by difficulties with density measurement. The microwave interferometer used for the density measurements (described in section 4.2.4) was sensitive to the gyrotron radiation, and during the gyrotron pulse the interferometer detector output was saturated, making density measurements impossible. This would have been a significant measurement in view of the influence of the density upon the accessibilty conditions. The positions of the resonances and cut-offs in TOSCA have been calculated by Lloyd [152], by assuming a parabolic electron density profile. Further details are given in chapter 2. Under the range of densities used in the experiments reported here, the low density X-mode cut-off may be present as far out as R = 37 cm, and for most experiments occurred at R > 34 cm, leaving a large volume of plasma inaccessible to the X-mode. At high densities ($\bar{n}_e > 1.5 \times 10^{19}$ m^{-3}) there exists the possibility of X-mode tunnelling through the upper hybrid layer [164], while the O-mode becomes evanescent in the plasma core. This experimental regime was not however attained in the experiments here under discussion. The resonances and cut-offs are illustrated for the case of $\bar{n}_e = 7.5 \times 10^{18}$ m^{-3} in figure 2.6. Attempts to produce low electron densities, and hence relaxed accessibility constraints, by the controlled reduction of plasma current resulted in reduced observable ECRH effects.

6.1.6 SOFT X-RAY SPECTRUM

The influence of RF heating on the soft x-ray spectrum is shown in figure 6.6, which was obtained using the x-ray energy pulse height analysis system described previously. This figure shows the non-thermal portion of the spectrum from an ohmically heated discharge, together with that obtained during ECR auxiliary heating experiments under the same conditions,

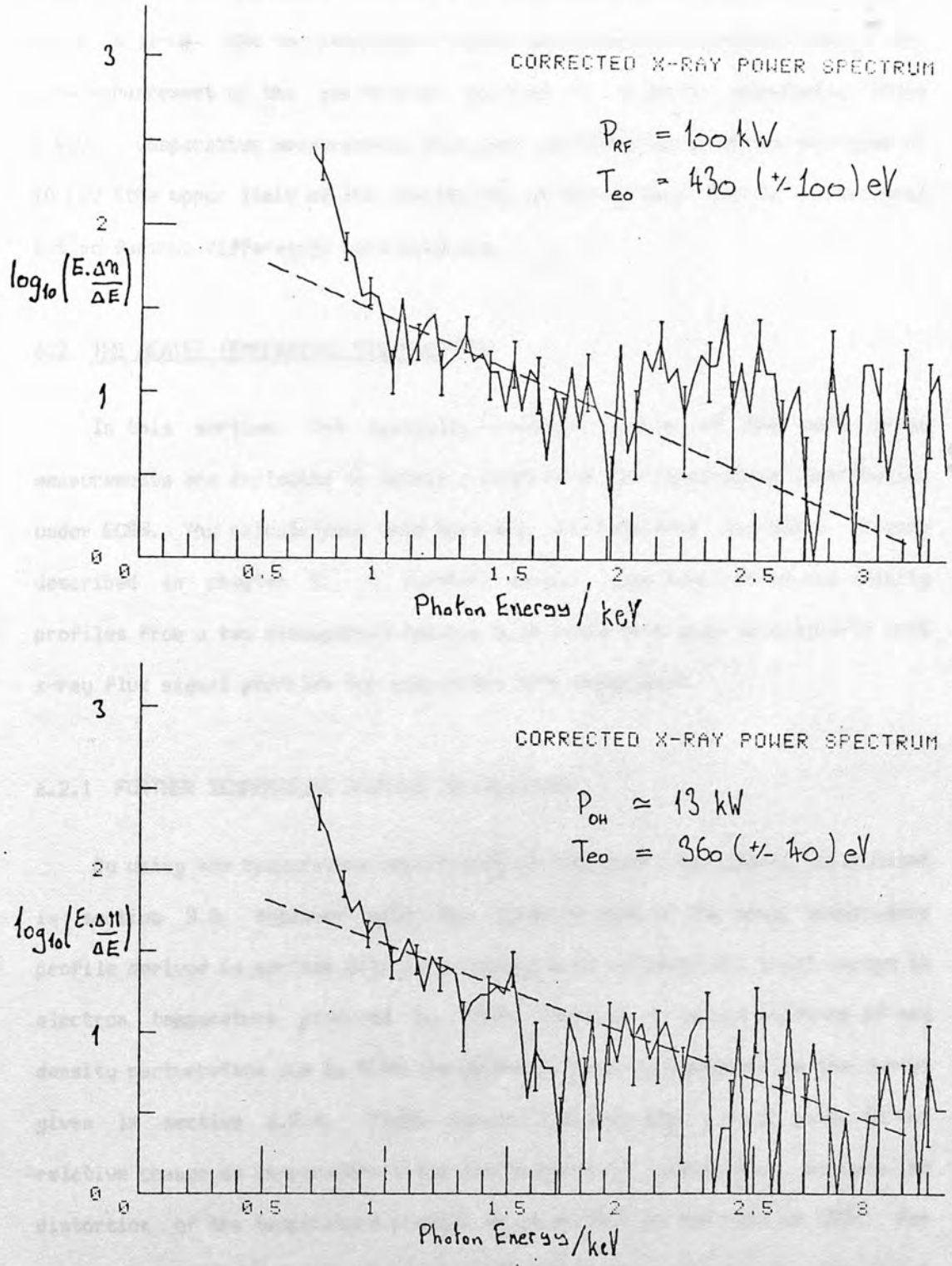

Figure 6.6

The effect of ECRH on the soft x-ray emission spectrum: a) with ECRH, b) ohmic heating alone. Reference to the broken line reveals RF heating to be accompanied by an increase in the non-thermal level of the spectrum.

at identical time periods. As a further precaution against the measurement of pulse pile-up, the two measurements were conducted at a constant count rate. Some enhancement of the non-thermal portion is evident, especially above 2 keV. Comparative measurements have been performed up to photon energies of 10 keV (the upper limit of the sensitivity of the surface barrier detectors) but no furthur differences were observed.

6.2 THE HEATED TEMPERATURE DISTRIBUTION

In this section, the spatially resolved nature of the soft x-ray measurements are exploited to obtain a profile of the temperature distribution under ECRH. The calculations used here are an extension to those already described in chapter 5. A further section uses temperature and density profiles from a two dimensional tokamak heat conduction code to calculate soft x-ray flux signal profiles for comparison with experiment.

6.2.1 FURTHER TEMPERATURE PROFILE CALCULATIONS

By using the temperature sensitivity of the soft x-ray signal calculated in section 3.2, together with the inferred idea of the ohmic temperature profile derived in section 5.1, it is possible to estimate the local change in electron temperature produced by ECRH. There is as yet no evidence of any density perturbation due to ECRH, so we may proceed by reference to the curves given in section 3.2.4. These curves can only give a rough guide to the relative change in temperature since the sensitivity calculation assumes no distortion of the temperature profile as is evident in the case of ECRH. For the observed soft x-ray signal enhancement, which is generally in the range 2 - 5 times (depending upon RF power and other plasma parameters), with the toroidal field chosen so as to place the ECR on the outside of the profile, a local temperature enhancement of 30 - 125 % is indicated. If the observed soft x-ray signal enhancement is due to bulk heating of the thermal part of

the electron population, then the consequences of this new temperature profile can be evaluated as in section 5.2. The heated profile is modelled by the addition of a temperature component due to ECRH, with radial distribution chosen to fit the soft x-ray observations. This is written as

$$T_e(r,\theta) = T_{e_{OH}}(r) + T_{e_{ECRH}}(r,\theta) \qquad 6.3$$

where $T_{e,OH}$ is the temperature profile under ohmic heating, and $T_{e,ECRH}$ simulates the modification due to ECRH, written as

$$T_{e_{ECRH}} = T_{o,ECRH} \exp \frac{-(r-r_{ECR})^2}{r_o^2} \exp^{-\theta^2/\theta_o^2} \qquad 6.4$$

The distribution in poloidal angle is not well resolved as a result of the position of the soft x-ray array, and is introduced as a parameter. However, some poloidal information is available from further calculations, presented in paragraph 6.2.2. The ECRH components of the temperature distribution used in the calculation more closely match those which would be expected from the strong X-mode heating scheme [15] (low-density, as described in section 2.2.1) than those corresponding to the relatively high density results described here. The model of section 5.2 can be used to evaluate the scaling of the effect of local heating on the properties of the discharge. The current density is calculated in accordance with observations on the basis of constant toroidal plasma current, the decrease in plasma resistance due to heating then being exhibited as a decrease in loop voltage. Figure 6.7 shows the relative plasma resistance decrease, as a function of local heating. Figure 6.8 gives a plot of the results of a similar calculation for beta-internal.

The calculated ECRH effects can be seen to be highly dependent upon the chosen poloidal width parameter, for which there is no measurement data available. Indications from the heat conduction calculations presented in paragraph 6.2.2 are that an angular width in the range 1.5 - 1.75 rad may not be unreasonable.

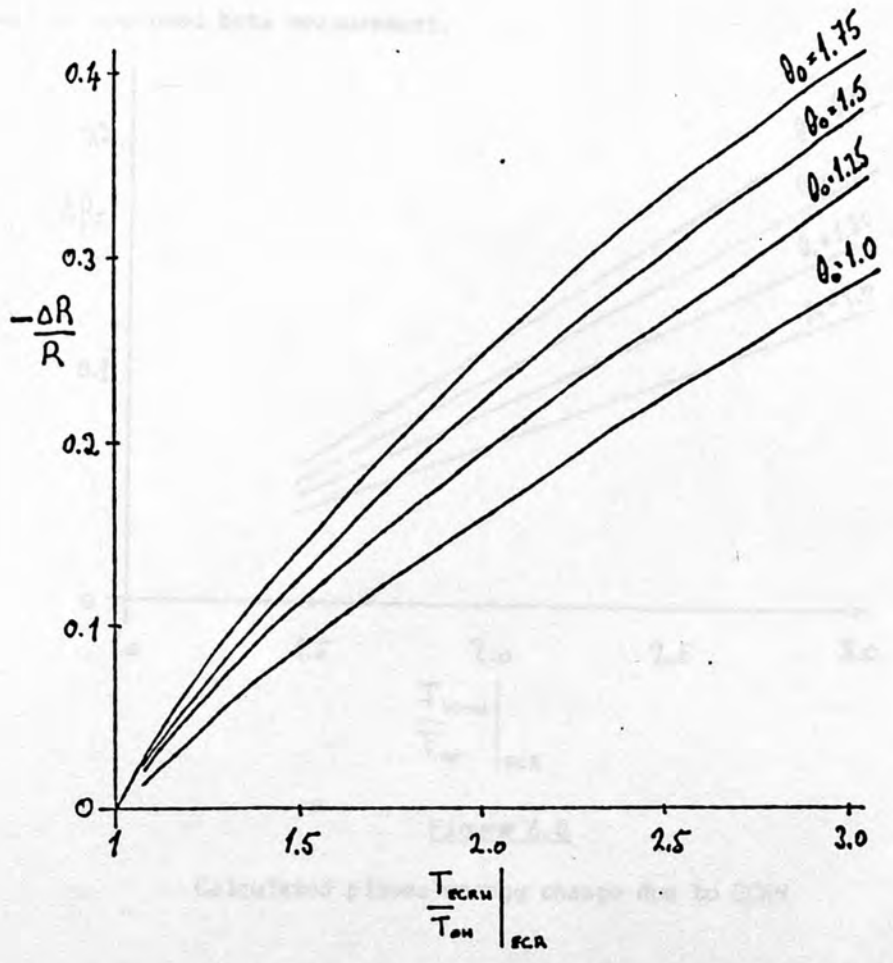

Figure 6.7

Calculated plasma resistance change due to ECRH

The calculated resistance behaviour (figure 6.7) is in fair agreement with observation (cf. figure 6.4), assuming that as the plasma current is observed to remain constant, the change in loop voltage is merely a manifestation of a changing plasma resistance. The maximum measured voltage drop (> 50 %) is outside the range of these predictions, but it should be noted that this is a rather variable quantity at apparently constant RF power.

The calculated change in plasma energy (figure 6.8) due to ECRH is down by a factor of more than two on the experimental data shown in figure 6.4. It is possible that this discrepancy is less than the error in the diamagnetic loop measurement, one of the measuring coils apparently having been damaged during vacuum vessel modifications. Further discussion on this point must

await an improved beta measurement.

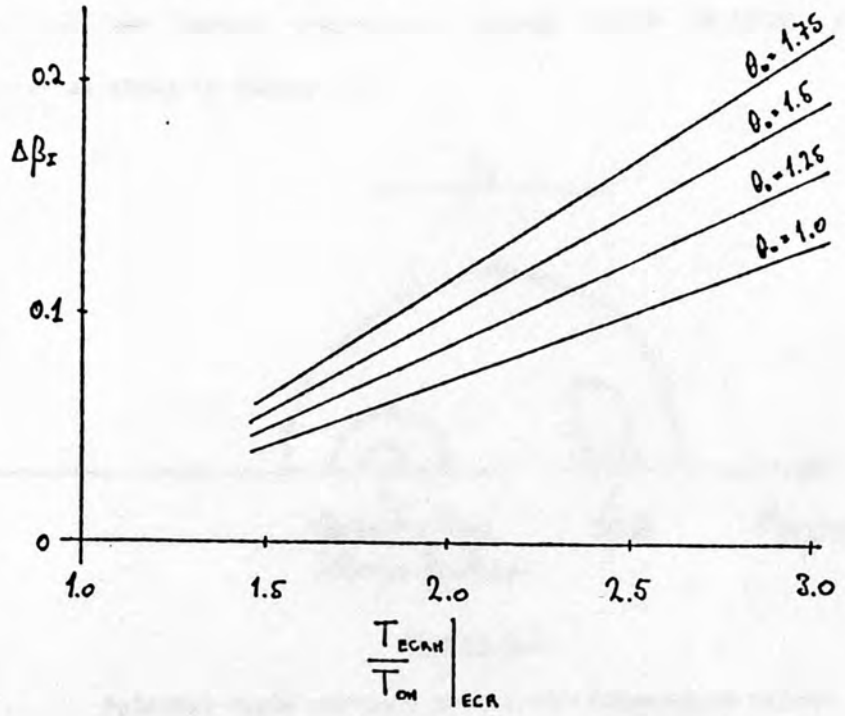

Figure 6.8

Calculated plasma energy change due to ECRH

It may be concluded from the calculations presented in this paragraph that if RF power is channelled into bulk heating of the plasma electrons, then large local temperature increases can be expected. The observed integral characteristics of the plasma may be in accordance with this view, in that the observed relative voltage change for 50 kW RF power implies a three-fold increase in the electron temperature at the ECR, and that the measured plasma energy change requires a similar local temperature gain.

Local Heating and Stability

In view of the instability observed by the soft x-ray signal at high levels of heating (see figure 6.3), it is of interest to calculate the behaviour of the safety factor near the ECR. The usual definition of q for a circularly symmetric system, as given in section 2.1.2, is

$$q(r) = \frac{rB_\phi}{RB_\theta(r)} \qquad 6.5$$

The calculation of the poloidal field is complicated in this case by the presence of the heated temperature island, which destroys the circular symmetry, as shown in figure 6.9.

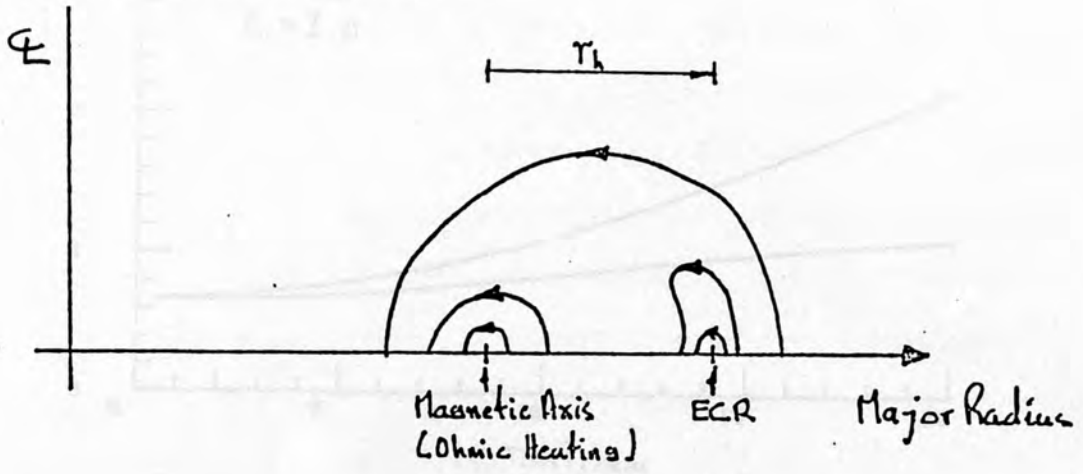

Figure 6.9

Poloidal field contours around the temperature island

The procedure for the evaluation of q near the ECR is to apply Ampere's Law to a circular integration path, which gives

$$\int \underline{B}.\underline{d\ell} = \mu_o \int \underline{j}.\underline{dS} \qquad 6.6$$

then if circular symmetry were to hold around the ECR,

$$2\pi|r-r_h|B_\theta = \mu_o \bar{j}_\phi |r-r_h|^2.\pi \qquad 6.7$$

where r_h is the position of the ECR, and $\bar{j}_\phi$ is the mean current density through the surface S of radius $r - r_h$. Then

$$B_\theta = \frac{\bar{j}_\phi}{2} \mu_o |r-r_h| \qquad 6.8$$

The value of q at the ECR will then be given by

$$q = \lim_{r \to r_h} \frac{2B_\phi}{R\bar{j}_\phi} \qquad 6.9$$

An example of the q-profile, calculated for one heating condition, is shown in figure 6.10. ECRH can very easily drive the local value of q below unity, in violation of an important tokamak stability condition. The two curves show the value of q as a function of $r-r_h$, evaluated approaching r from $R > R_h$ and $R < R_h$. The safety factor is found to be less than unity over a considerable region.

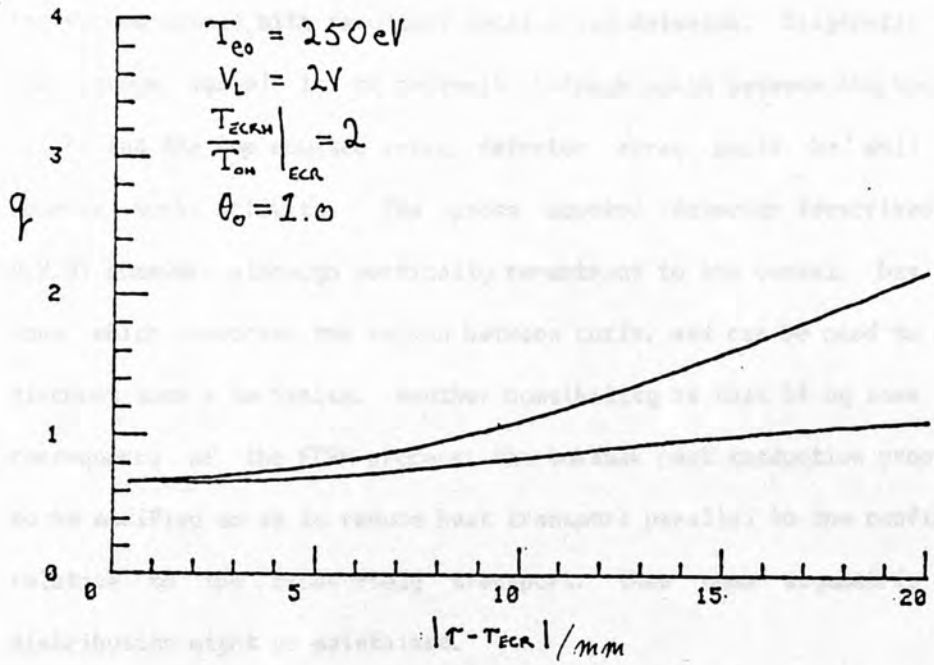

Figure 6.10

Calculated safety factor near the ECR

6.2.2 HEAT CONDUCTION AND X-RAY PROFILE CALCULATION

An immediately apparent feature of the ECRH experiments conducted so far has been the asymmetric profile of soft x-ray signal enhancement. This is most surprising, for if the increase in signal is due to local heating of the electrons then one might expect the effect of rapid heat conduction parallel to the magnetic field, and moderate safety factor, to result in an effective transport of thermal energy around the magnetic flux surfaces coincident with the resonance zone. That this is not the case then indicates some departure from this simple view of tokamak conduction.

There exist in principle a number of ways in which a tokamak could behave in accordance with the soft x-ray observations, through the influence of the RF heating on the distribution of electron velocities. One suggestion is the creation of an abnormally large concentration of electrons trapped by the toroidal field ripple between coils. Such trapped electrons drift down in the radial field gradient, there being no net rotational transform, to intercept

the vacuum vessel with resultant local x-ray emission. Diagnostic access to the vacuum vessel is of necessity through ports between the toroidal field coils, and the top mounted x-ray detector array would be well placed to observe such activity. The probe mounted detector (described in section 4.2.3) however, although vertically re-entrant to the vessel, has a viewing cone which traverses the region between coils, and can be used to effectively discount such a mechanism. Another possibility is that if by some detail or consequence of the ECRH process, the tokamak heat conduction properties were to be modified so as to reduce heat transport parallel to the confining field relative to the cross-field transport, then some asymmetric temperature distribution might be maintained.

In order to investigate the scope of some possible anomalous conduction behaviour, tokamak heating by a gyrotron has been simulated in a 2-D transport code [154], which attempts to follow the evolution of the temperature and current density profiles. Anomalous heat conduction is represented by manipulation of the heat conduction coefficients. By reducing the ratio of parallel to perpendicular conduction by 100 times the normal cylindrical tokamak value, it was possible to generate an asymmetric temperature profile similar to that evaluated in section 6.2. The gyrotron contribution to the plasma heating equation was of the form

$$S(r,\theta) = A \exp \frac{-(r-r_{ECR})^2}{r_o^2} \exp -\theta^2/\theta_o^2 \qquad 6.10$$

The distribution parameters were chosen in accordance with heating zone width calculations already described in 2.2 [15, 151]. The coefficient A was selected with regard to the ratio of ohmic to effective ECRH power, as determined by Fielding's heating profile calculations [15]. Different size temperature perturbations were obtained by stopping the calculation at intervals. The data sets obtained gave local temperature gains at the simulated ECR zone in the range 1.46 - 2.52. The temperature and current density were calculated on a 50x20 (r,θ) mesh. An example of the temperature

distributions obtained is given in figure 6.11.

Analysis proceeds by using these distorted electron temperature profiles as templates for comparison of their calculated x-ray characteristics against the measured x-ray profile during ECRH. The signal calculation takes full account of the measurement geometry, filter transmission and detector response, as detailed in section 3.2. A parabolic electron density profile is assumed, with initial conduction calculations being performed in cyclindrical geometry. An example of the radial profiles of soft x-ray signal calculated from these data is illustrated in figure 6.12, which shows a family of curves calculated from a data set with a two-fold local temperature gain. The central temperature is introduced as a parameter.

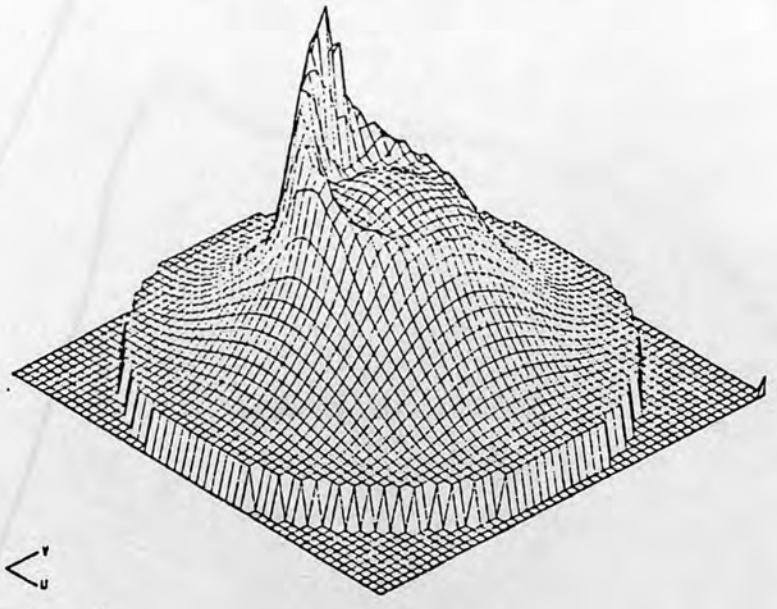

Figure 6.11

Temperature profile with a local gain of 1.98

The signal calculations are reduced to radial profiles of the soft x-ray enhancement produced by ECRH for comparison with experimental measurements. Figure 6.13 shows the result for the smaller temperature perturbations, for central electron temperatures of 200 and 300 eV. The asymmetry in the calculated profile is evident, with a profile width and magnitude well reproducing the experimental measurements. The radial profile obtained by the

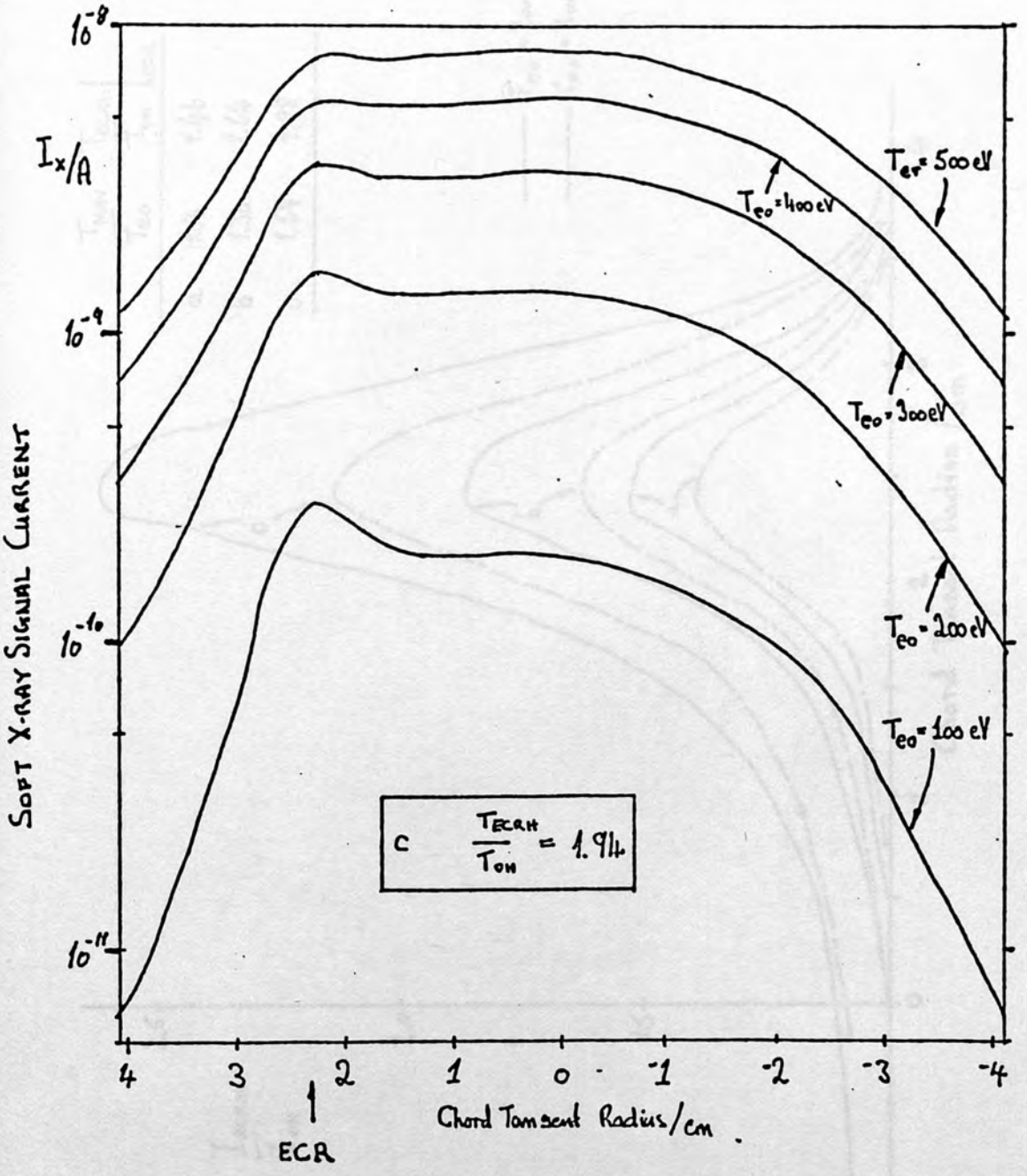

Figure 6.12

Soft x-ray signal current profile calculated for surface barrier detectors on TOSCA

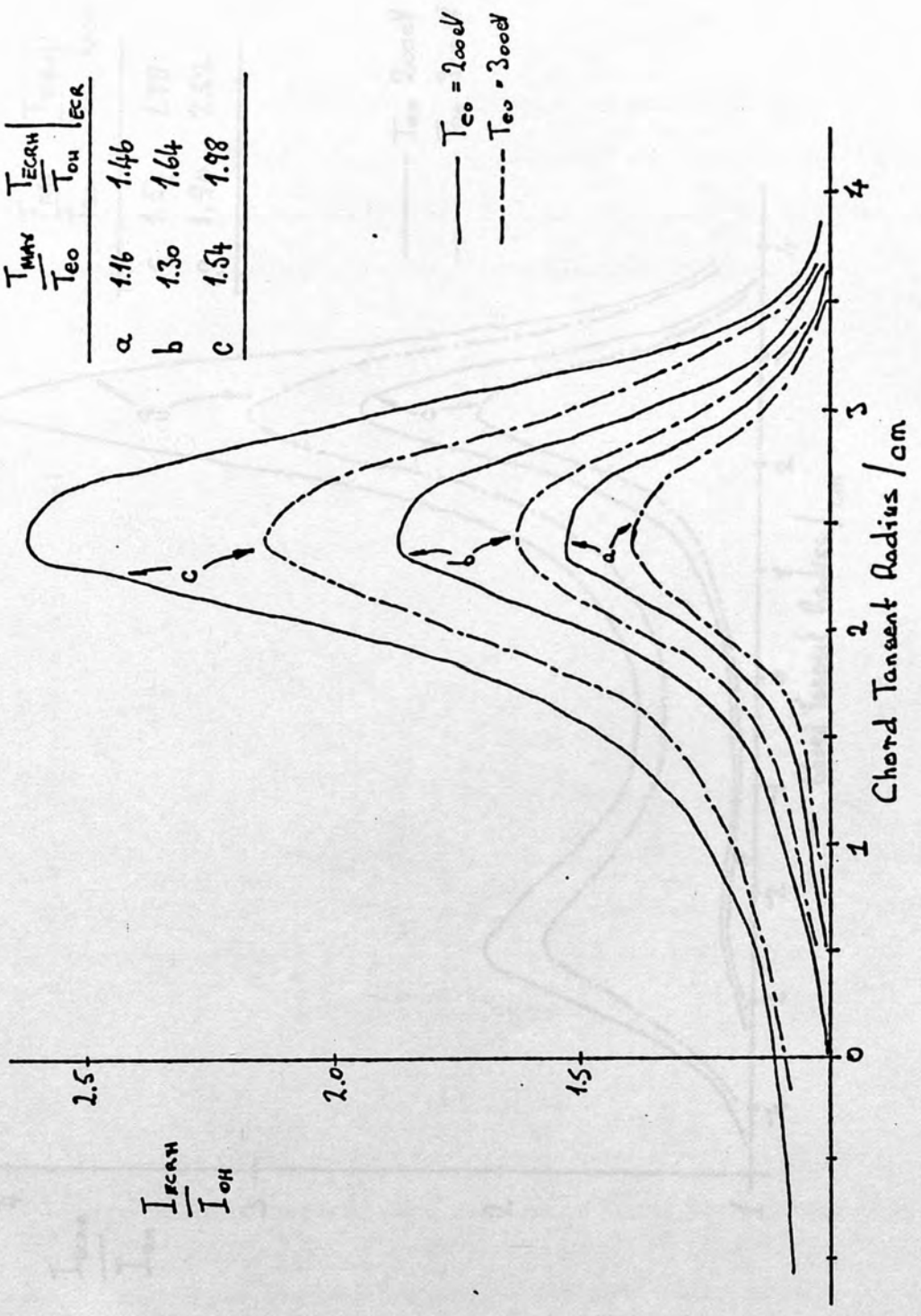

Figure 6.13

Profiles of soft x-ray signal enhancement - small ΔTe case

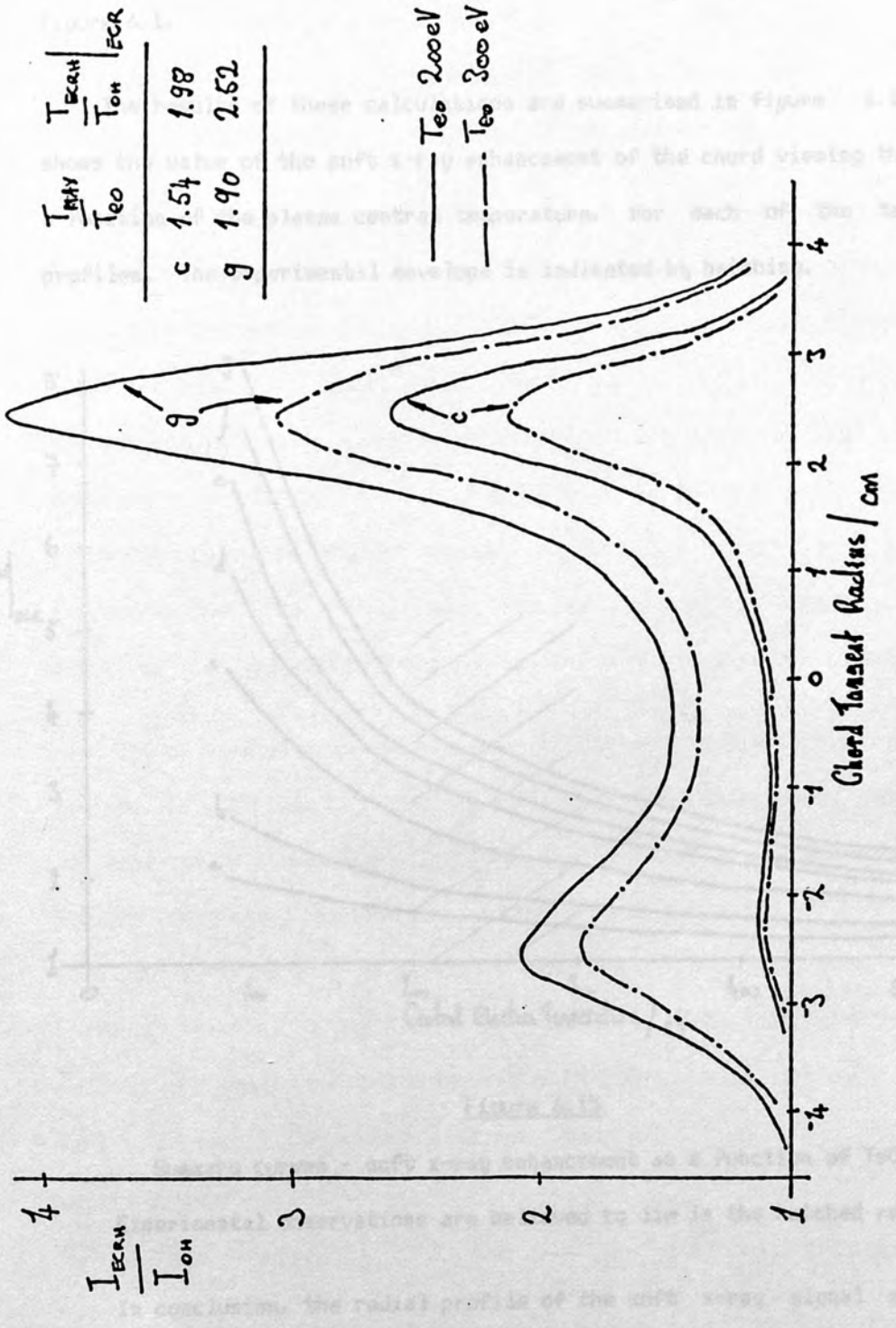

Figure 6.14

Profiles of soft x-ray signal enhancement - large ΔTe case

above procedure for the larger temperature gain cases is shown in figure 6.14, where appreciable enhancement of the soft x-ray signal on the inside of the profile is observed, which is not evident in the experimental result shown in figure 6.1.

The results of these calculations are summarised in figure 6.15, which shows the value of the soft x-ray enhancement of the chord viewing the ECR, as a function of the plasma central temperature, for each of the temperature profiles. The experimental envelope is indicated by hatching.

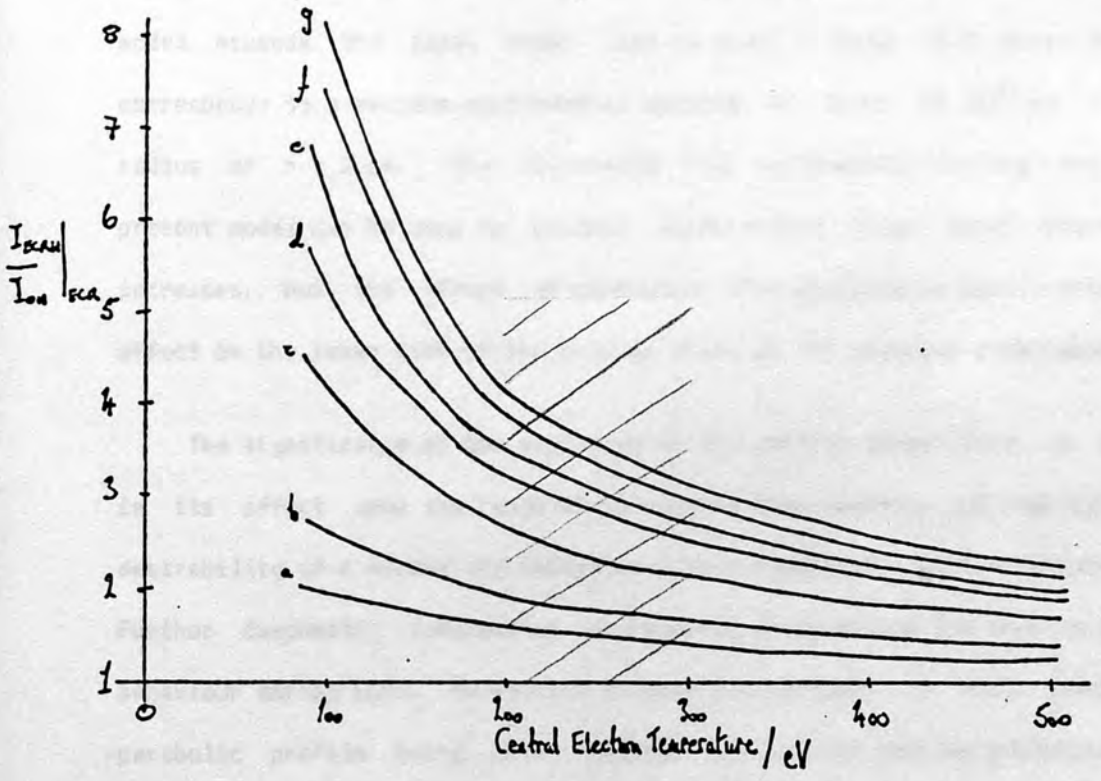

Figure 6.15

Summary curves - soft x-ray enhancement as a function of Te0.

Experimental observations are believed to lie in the hatched regime.

In conclusion, the radial profile of the soft x-ray signal enhancement has been obtained from an asymmetric temperature distribution derived from a model of anomalous heat conduction in a cylindrical tokamak. The calculated width of the soft x-ray signal is in good agreement with the experimental

profile. Comparison of the calculated and observed magnitudes of soft x-ray flux enhancement show the calculation to predict values on the low side of experiment, in that for RF powers of greater than 100 kW, local soft x-ray signal enhancements of greater than five times could on occasion be obtained, which for likely electron temperatures in TOSCA requires that the ratio of ECRH electron temperature to ohmic at the ECR exceeds 2.5.

The anomalous conduction properties used in this study are described by the ratio $\kappa_{\parallel}/\kappa_{\perp} = 100$, where the κ's are the conduction coefficients with respect to the confining magnetic field. The peak additional heating in the model exceeds the local ohmic rate by about a factor of 8, which in TOSCA corresponds to a maximum supplemental heating of about 10 Wcm^{-3} at a minor radius of r = 2 cm. The relatively high supplemental heating rate in the present model can be used to produce sufficiently large local temperature increases, but the effect of conduction then produces an easily detectable effect on the inner side of the profile which is not observed experimentally.

The significance of the magnitude of the central temperature is evident in its effect upon the range of calculated enhancements, and highlights the desirability of a second and independent measurement of electron temperature. Further diagnostic information is required to determine the density profile behaviour during ECRH. No density effects are included in this model, the parabolic profile being held constant through the heating evolution. Any density decrease associated with ECRH would clearly work strongly against a soft x-ray signal enhancement (see equation 3.6).

6.3 SUMMARY

New spatially resolved measurements of the effect of second harmonic ECRH in a small tokamak have here been reported. The dependence of the observed effect upon position, magnetic field strength, and radio frequency power is revealed. Other significant features of ECRH in TOSCA were the enhancement of

non-thermal emission in the soft x-ray spectrum, and the asymmetry of the observed profile of the heating effect, significant heating occurring only at a major radius greater than that of the plasma magnetic axis. Similarly, significant heating effects were observed only when the ECR was placed on the outside of the magnetic axis.

Using the calculated sensitivity of the soft x-ray flux diagnostic to plasma temperature variations, the size of the temperature gain at the ECR during the gyrotron heating pulse was estimated, subject to the stated limitations on the sensitivity calculation. The measured soft x-ray flux signal profile indicated that ECRH resulted in a strongly asymmetric temperature profile in minor cross-section. The calculations of tokamak integral properties detailed in chapter 5 were performed using such a temperature distribution. The calculated plasma resistance and thermal energy were compared with those measured during ECRH. It was shown that the temperature at the ECR, as indicated by these calculations, is sufficient to reduce the value of the MHD safety factor at the ECR to less than unity, in violation of an important tokamak stability condition.

As an alternative approach to the estimation of the temperature change brought about by ECRH, results from a tokamak heat conduction code were used. In this model, ECRH was simulated by the introduction of an appropriate localised heating term. The spatial temperature profiles produced by this code were used to calculate the profile of the soft x-ray flux signal. By comparing this latter result with experimental observations, a confirmatory measure of the local temperature gain due to ECRH was obtained.

CHAPTER 7 ELECTRON CYCLOTRON RESONANCE HEATING IN TOSCA

In section 6.2, the data from the observations of second harmonic ECRH in TOSCA was reduced, using the techniques developed earlier in this work, to spatial profiles of electron temperature. In this section a possible underlying mechanism is outlined which accounts for the observed features of conditional and localised heating. This mechanism is concerned with the role of plasma electrons trapped by toroidal field inhomogeneity, and the influence of ECRH upon the orbits of these trapped electrons.

7.1 PARTICLE TRAPPING

The conservation of energy of a charged particle as it follows a magnetic field line may be written as [153]

$$\frac{1}{2} m v_{\parallel}^2 + \mu . B = \varepsilon \qquad 7.1$$

where ε is the constant energy, $v_{\parallel}$ is the velocity parallel to the field and μ is the magnetic moment. The magnetic moment arises from the velocity component perpendicular to the field, and is defined as

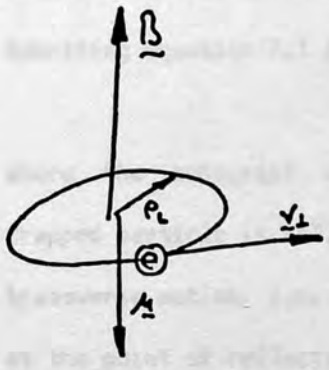

$$\mu = \text{(circulating current).(area of loop)}$$

$$= (e . \frac{\omega}{2\pi}) . (\pi \rho_L^2)$$

$$= \frac{e^2 B}{2\pi m} . \pi \left(\frac{V_\perp m}{eB} \right)^2$$

$$= \frac{m V_\perp^2}{2B}$$

For quasi-periodic motions, μ is an adiabatic invariant [32] in that it remains constant in fields which change slowly over distances of order ρ_L, and with times of order ω^{-1}. Then from equation 7.1, as a particle following a field line moves from a region of low field to a region of high field, with constant magnetic moment, $v_{\parallel}$ falls accordingly. In tokamak field geometry particles with small $v_{\parallel}$ at the region of minimum field (outer side of the torus) become trapped by the toroidal field variation with major radius.

Trapped particles travelling to and fro experience radial drifts in opposite directions [153], and their orbit guiding centres execute the so-called banana orbits, illustrated in figure 7.1.

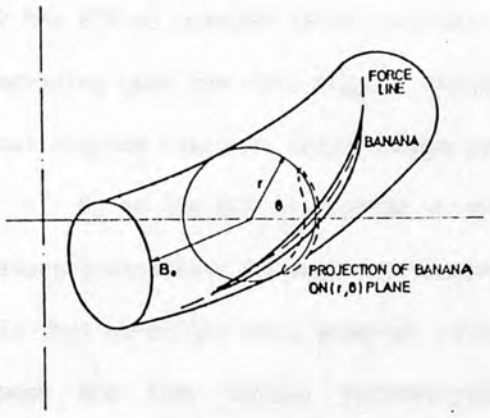

Figure 7.1

Trapped particle trajectories

7.2 INFLUENCE OF ECRH ON TRAPPED PARTICLES

ECRH acts by increasing the electron energy perpendicular to the magnetic field. This results in an increase in the magnetic moment component of energy (and an increase in total energy), with consequent effect upon trapping. Rewriting equation 7.1 as

$$E + \mu B_o = C \qquad 7.2$$

where the subscript defines quantities measured at the outer equator, a trapped particle is reflected at the point where all its energy is in transverse motion, i.e. $E_{\parallel} = 0$ and $B_r = C/\mu$, where B_r is the field strength at the point of reflection. The effect of heating upon a trapped electron can be evaluated by determining the behaviour of B_r as is increased by repeated passage of the electron through the ECR zone. The problem is formulated by supposing that the magnetic moment is increased by an amount $\Delta\mu$ with each passage through the heating zone. Then

$$B_{r_i} = C_i/\mu_i \qquad 7.3$$

$$C_{i+1} = C_i + \Delta\mu B_o \qquad 7.4$$

$$\mu_{i+1} = \mu_i + \Delta\mu \qquad 7.5$$

$$B_{r_{i+1}} = \frac{C_i + \Delta\mu B_o}{\mu_i + \Delta\mu} \qquad 7.6$$

It is easy to show that

$$B_{r_n} \rightarrow B_o \quad \text{as} \quad n \rightarrow \infty$$

provided that the ECR is outside of the magnetic axis, the rate of approach to the limit depending upon the size of $\Delta\mu$. The significance of the position of the ECR is that trapped electron trajectories can only converge toward the point where $B = B_o$ if the ECR is outside of the magnetic axis, thus allowing for the necessary transitions through the resonant zone. The consequence of this result is that particles once trapped, either by collision or by repeated passage through the ECR, become increasingly localised and energetic. Furthermore, if the resonance zone is placed on the outside of the magnetic axis, then energetic electrons are concentrated in the region of the ECR. Here then is a mechanism which provides for the two principle features discussed in the model of section 6.2, namely the concentration of high energy electrons (reflected as localised heating), with limited toroidal freedom leading to reduced toroidal conduction capability.

Further evidence may be obtained from the information in the measured soft x-ray spectrum, and the calculated energies of the ECRH-induced trapped particles. The observed spectral features may be related to trapped particle orbit half widths. The orbital half width is given by Furth [6] as

$$\Delta r = r_p (r/R)^{\frac{1}{2}} \qquad 7.7$$

where r_p is the electron Larmor radius in the poloidal field. Substituting for r_p gives

$$\Delta r \cong 3.4 \times 10^{-6} \frac{T_{ev\perp}^{\frac{1}{2}}}{B_p} (r/R)^{\frac{1}{2}} \text{ m} \qquad 7.8$$

With observed spectral enhancement at about 3 keV (see figure 6.6), and a poloidal field strength of 20 mT at r = 20 mm (calculated from equation 5.10), the half-width is evaluated as

$$\Delta r \sim 2\text{-}3 \text{ mm} \qquad 7.9$$

i.e. the full orbit width is the same size as the calculated resonance zone size [151] (calculated in section 2.2.1).

One obtains a view of ECRH in TOSCA acting as a pinch mechanism, spatialy concentrating trapped electrons toward the location of the resonant field value. Since the resonant zone has a finite width, the effect of these energetic electrons, as seen for example in the soft x-ray signal, is observed across a finite width in minor cross-section. Furthermore, as the orbit width of a trapped electron is related directly to its transverse energy (see equation 7.7), the size of the resonant zone may also determine the maximum energy attained by a trapped electron, in the following way. It was proved previously (equation 7.6) that trapped electron orbits converge toward the ECR provided that the resonance lies outside the magnetic axis of the system. The limit of this convergence mechanism is clearly reached when the trapped electron orbit no longer intersects the resonant heating zone. Thus a condition for the maximum energy a electron may achieve will very approximately be given by that found from equating the banana orbit width with the resonant heating zone size. This condition arises as a result of the effect of electron-ion collisions, as a result of which a trapped electron may pass through the ECR with a number of different values of velocity parallel to the magnetic field as its orbit converges toward the ECR, with correspondingly greater or lesser Larmor radii. It is precisely the distribution of parallel velocites that give rise to the Doppler broadening of the ECR to a resonant zone of finite width. This second feature which regulates the ECR heating of a trapped electron provides an explanation for the form of the measured soft x-ray spectrum, which showed enhanced radiation over the ohmic case in the region 2.5 - 3 keV. When electron energies exceed this value, the size of their Larmor radii takes them once again outside of the resonant heating zone. These ideas are summarised in figure 7.2.

Of some interest, as a test of this hypothesis, would be the study of the dependence of ECRH effectiveness as a function of plasma current. This would be significant as a consequence of the effect of the poloidal field strength on the banana orbit half-width, so the heating profile width might be expected

to be some function of the plasma current.

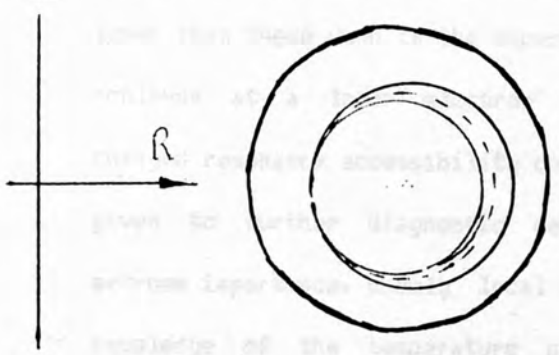

A trapped electron executes banana orbits.

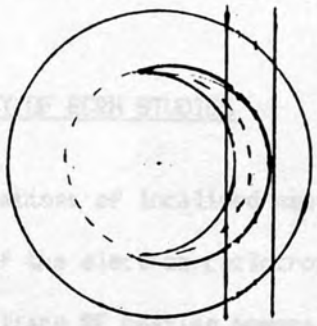

Resonant heating increases the magnetic moment of electrons passing through the resonant heating zone. The orbits converge . . .

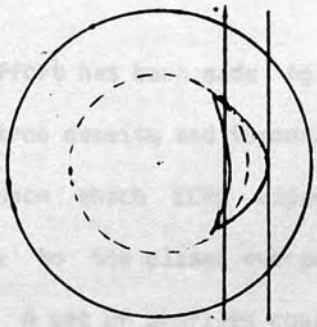

until the banana orbit width $\simeq$ resonance zone width.

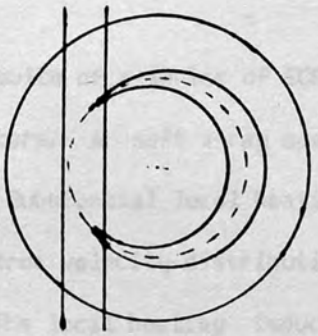

When the ECR is on the inside of the magnetic axis, convergence of trapped electron trajectories is thus limited.

Figure 7.2

Resonant heating of trapped electrons in TOSCA

There are difficulties with this experiment however, which lie in the

interdependence of density, temperature and current in the tokamak. Currents lower than those used in the experiments described in this work can only be achieved at a lower electron density, which would result in significantly changed resonance accessibility conditions. Secondly, high priority should be given to further diagnostic development. Two areas in particular are of extreme importance, namely local temperature measurement to increase the knowledge of the temperature profile, and secondly any form of density measurement during the heating pulse.

7.3 SUMMARY OF ECRH STUDIES

Observations of localised heating in a tokamak, utilising the second harmonic of the electron cyclotron resonance, are here reported for the first time. Auxiliary RF heating powers in excess of 150 kW have been used in a plasma where the ohmic heating rate was less than 16 kW.

Some effort has been made to determine the spatial distributions of plasma electron density and temperature characteristic of the ohmically heated discharges upon which ECRH experiments have been conducted. The ionic contribution to the plasma energetics under these conditions was shown to be negligible. A set of profiles consistent with experimental measurements was obtained.

The results of a series of ECRH experiments, as monitored by soft x-ray flux detectors, a soft x-ray spectrometer, and other diagnostics, have been presented. Substantial local heating was observed, and some distortion of the plasma electron velocity distribution function was evident from the soft x-ray spectrum. The local heating induced an $m = 1$ instability. The observed heating profile was found to compare very favourably with predictions for strong X-mode heating, despite the presence of an X-mode cut-off at large minor radius.

Calculations of the integral characteristics of the plasma have been performed, based on an inferred temperature profile, with a perturbed temperature component estimated from the calculated temperature sensitivity of the soft x-ray flux signals, and are presented in section 6.2.1. The calculated values are in fair agreement with experiment, with a local temperature increase of 4-times being necessary to account for a 50 % plasma resistance reduction. Furthermore, it has been shown that the localised heating can lower the value of the safety factor at the ECR to below the tokamak stability limit of $q = 1$, which may be in accord with observed localised gyrotron-induced oscillations in the soft x-ray flux. The observed radial profile of soft x-ray flux enhancement, taken with existing knowledge of tokamak plasmas, implies that some anomalous heat conduction is induced in the experiments.

An anomalous tokamak heat conduction model, with high local heating simulating ECRH, was used to generate temperature profiles with local temperature increases at the ECR sufficiently large to account for the observed soft x-ray signal, neglecting any ECRH-induced density behaviour. Integral characteristics of the discharge, calculated from profiles with similar local temperature increases, were in fair agreement with measurement. The convergence of the value of the local temperature gain due to ECRH, deduced from both the x-ray signal calculation, and from the plasma integral characteristics calculation, lends considerable support to the assertion of bulk plasma electron population heating.

Finally, a possible mode of action of ECRH in TOSCA is indicated, which may account for the observed features of conditional, local, heating, as observed with soft x-ray detectors with a known energy sensitivity, and anomalous toroidal energy transport. This mechanism postulates that the observed effects are due to the influence of the RF power upon the trapped electron population. The approach to this final description of the plasma

under ECRH is summarised in figure 7.3.

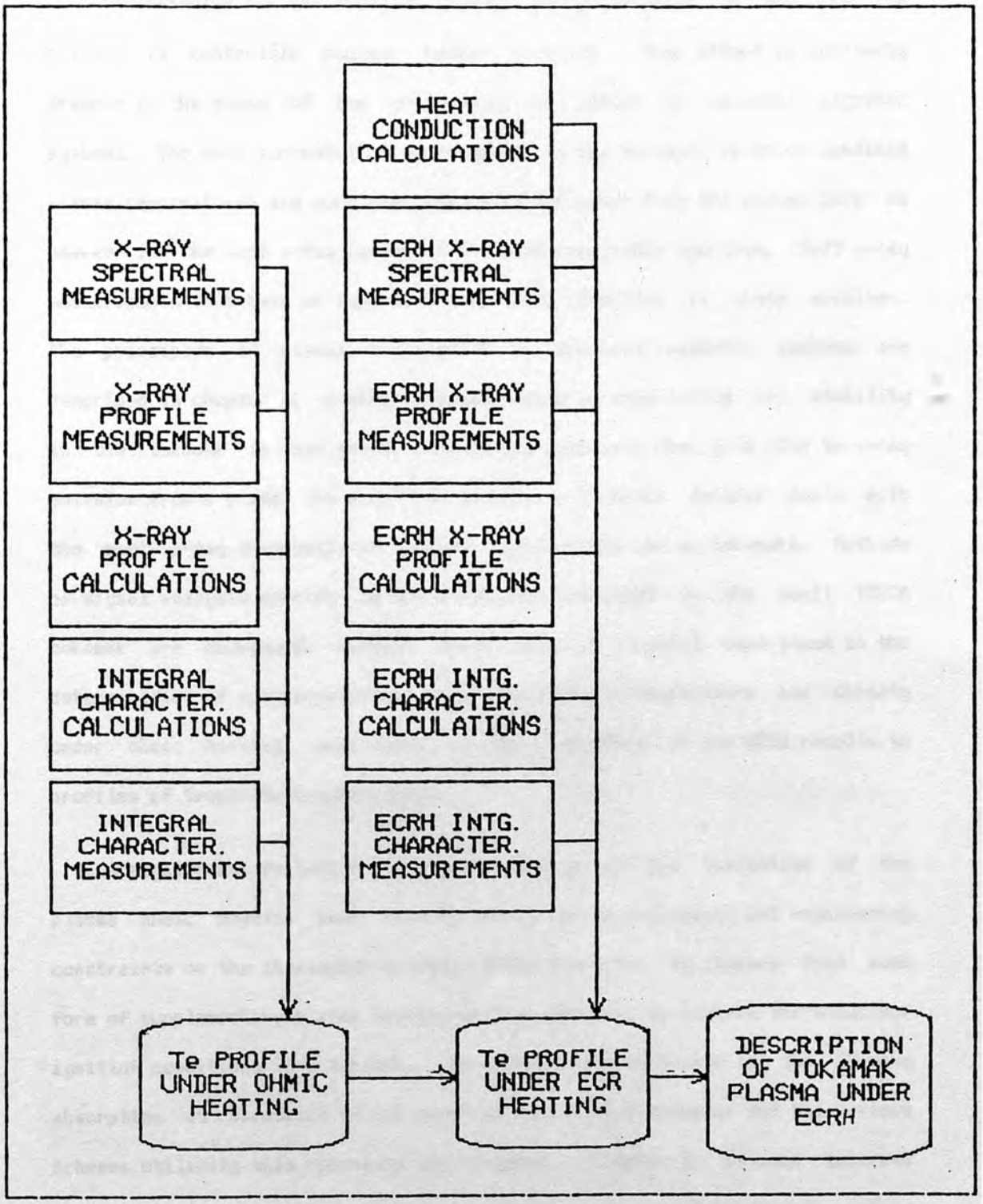

Figure 7.3

Summary of experiments and conclusions on the TOSCA tokamak

7.4 CONCLUSION

The stimulus for the study of plasma x-ray emission is the role of plasmas in controlled nuclear fusion research. Much effort is currently devoted to the study of the confinement of plasma in toroidal magnetic systems. The most succesful of such systems is the tokamak, in which confined plasma temperatures are such that the radiation power from the plasma core is peaked in the soft x-ray region of the electromagnetic spectrum. Soft x-ray measurements thus have an important diagnostic function in these machines. The principles of plasma confinement in toroidal magnetic systems are described in chapter 2. A more detailed review of equilibrium and stability in the tokamak is then given. The atomic processes that give rise to x-ray emission from a plasma are described in chapter 3, which further deals with the soft x-ray diagnostic techniques developed for use on tokamaks. Methods of signal analysis specific to the diagnostic installed on the small TOSCA tokamak are developed, results which were of crucial importance in the determination of spatial profiles of plasma electron temperature and density under ohmic heating, and hence to the reduction of the ECRH results to profiles of temperature enhancement.

A significant feature of the tokamak design is the limitation of the plasma ohmic heating power density set by the technological and engineering constraints on the attainable toroidal field strength. It appears that some form of supplementary plasma heating will be required to achieve thermonuclear ignition conditions in a tokamak. One such heating mechanism is the EM-wave absorption at harmonics of the electron cyclotron frequency, and the various schemes utilising this resonance are reviewed in chapter 2. Renewed interest in this form of heating has been created by the availability of gyrotron microwave generators, which now permit high power heating experiments. A 200 kW, 28 GHz device has recently been installed on TOSCA. Auxiliary heating experiments at the second harmonic of the ECR in low current (< 8 kA)

discharges are reported. The form of the ohmically heated plasma electron temperature distribution characterising these discharges was established by the comparison of experimental measurements with properties calculated from a model of the temperature profile. Points of comparison were the central electron temperature, the radial profile of the soft x-ray flux signal, the axial current density, total plasma current, and plasma thermal energy. The temperature profile deduced in this way was found to be very similar to that measured by Thomson scattering on the Soviet tokamak TM-3.

A property of the ECR in the tokamak is its spatial localisation, due to the dependence of the strength of the dóminant toroidal field on major radius. ECRH then has the potential for (in addition to bulk plasma heating) current profile (and hence MHD stability) control, and DC current drive, both of which would be of great practical benifit in tokamak operation. The spatial resolution of the soft x-ray diagnostics on TOSCA were here fully exploited in the study of the heating effect, which is indeed found to be localised in the region of the ECR. The soft x-ray observations show that the prevailing transport mechanism does not freely allow the conduction of thermal energy around the magnetic flux surfaces coincident with the ECR. Also reported are the effects of ECRH on the plasma loop voltage and thermal energy in these discharges. Experiments further show that the RF power is ineffective if the ECR is placed on the inside of the plasma magnetic axis. The profile of the soft x-ray signal gain during ECRH is reduced to a modified electron temperature profile, using the analysis methods developed earlier in this work. Local temperature at the ECR could be increased by more than a factor of two. The consequences of the modified profile on the surface-integral characteristics of the discharge were calculated and found to be in fair agreement with experiment, inferring that some bulk electron heating had been achieved. X-ray spectrum measurements have been conducted during ECRH, but have not detected an electron temperature increase, possibly due to the overlap of the emission from the cooler but denser core with that from the

hotter ECR region. The temperature profile was further investigated with the aid of a two-dimensional heat conduction and field diffusion code. ECRH was simulated in the code by the introduction of a high local heating source. Asymmetric electron temperature profiles were produced by manipulation of the ratio of the heat conduction coefficients with respect to the confining magnetic fields. One-dimensional soft x-ray signal profiles were calculated from the distributions so produced, and their characteristics compared with observations recorded during ECRH. With the ratio $\chi_{\parallel}/\chi_{\perp} = 100$, it was possible to generate soft x-ray signal profiles in good agreement with experiment for small temperature increases at the ECR (< x2). Larger temperature increases resulted in sufficient transport around the flux surfaces to give a noticeably perturbed signal on the opposite side of the profile. That both the surface integral calculations, and the x-ray signal profile calculations, require similar increases in electron temperature at the ECR to reproduce the respectively observed behaviours, is good evidence for effective heating of the bulk of the electron population in the region of the ECR, and thus demonstrated the potential of ECRH for plasma current profile control.

The role of trapped electrons in accounting for the observed features of ECRH is TOSCA is discussed. It is shown how the action of cyclotron resonance heating can concentrate energetic trapped electrons in the region of the ECR if the resonance is placed on the outside of the magnetic axis. The presence of energetic electrons is confirmed by a feature in the x-ray spectrum, where enhanced radiation in the band 2 - 3 keV is observed. The way in which the width and position of the ECR controls the accumulation and energy of trapped electrons at the ECR is shown. Ways in which further studies may forward the understanding and application of this heating mode are proposed.

REFERENCES

1 H A B Bodin, B E Keen, Rep Prog Phys 40(1977)1415

2 L A Artsimovich, Nucl Fusion 12(1972)215

3 Y Wen, Culham Lab Internal Note TN(80)3 (1981)

4 D Ciscato, IEA Workshop on Computer Control and Data Acquisition, Tokai-mura, 1979

5 V S Mukhovatov, V D Shafranov, Nucl Fusion 11(1971)605

6 H P Furth, Nucl Fusion 15(1975)487

7 J A Wesson, Nucl Fusion 18(1978)87

8 M D Kruskal, USAEC Report NYO-6045 (1954)

9 V D Shafranov, Sov Phys J Atom Energy 1(1956)709

10 L Spitzer, 'Physics of Fully Ionised Gases', Interscience, NY, 1956.

11 R C Birch, C W Gowers, F A Hass, P A Jones, K McGuire, D C Robinson, A Sykes, M Turner, A J Wootton, 9 Proc Eur Conf on Controlled Fusion and Plasma Physics, Oxford, 1(1979)43

12 H Eubank et el, 7 Proc Int Conf on Plasma Physics and Controlled Nulcear Fusion Research, Innsbruck, 1978, paper IAEA-CN-37/C-3

13 A C Riviere, in Plasma Physics and Nuclear Fusion Research (ed R D Gill), Academic Press, London, 1981.

14 J P Dougherty, ibid.

15 P J Fielding, Culham Laboratory Preprint CLM-P615. (1980)

16 P J Fielding, in Plasma Physics and Nuclear Fusion Research (ed R D Gill), Academic Press, London, 1981.

17 A V Gapanov, V A Flyagin, A Sh Fix, A L Gol'denberg, V I Khizhnkak, A A G Luchinin, G S Nusinovich, M I Petelin, Sh Ye Tsimring, V G Usov, S N Vlasov, V K Yulpatov, Int J Infrared and Millimeter Waves, 1(1980)351

18 Varian Corporation, Publication No 4360.680(1980)

19 V V Alikaev, G A Bobrovskii, M M Ofitserov, V I Poznyak, K A Razumova, ZhETF Pis Red 15(1972)41

20 V V Alikaev, G A Bobrovskii, V I Poznyak, K A Razumova, Yu A Sokolev, 5 Proc Eur Conf on Controlled Fusion and Plasma Physics, Grenoble, 1(1972)108

21 V V Alikaev, G A Bobrovskii, V I Poznyak, K A Razumova, V V Sannikov, Yu A Solokov, A A Shmarin, Sov J Plasma Phys 2(1976)212

22 V V Alikaev, G A Bobrovskii, V I Poznyak, K A Razumova, Yu A Sokolov, 5 Proc Int Conf Plasma Phys and Controlled Nuclear Fusion Research, Tokyo, 1974, paper IAEA-CN-33/A9-4

23 H P Furth, 9 Proc Eur Conf on Controlled Fusion and Plasma Physics, Oxford, 2(1979)309

24 International Tokamak Reactor Workshop, Zero Phase Report, IAEA Vienna, 1980.

25 M Bornatici, F Engelmann, C Maroli, V Petrillo, FOM-Innstituut voor Plasmafysica Report IR 80/034 (1980)

26 E Ott, B Hui, K R Chu, Phys Fluids 23(1980)1031

27 S Tanaka, T Maekawa, Y Terumichi, Y Hamada, IEEE Trans Plasma Sci PS-8(1980)68

28 D W Swain et al, 9 Proc Eur Conf on Controlled Fusion and Plasma Physics, Oxford, 1(1979)44

29 R M Gilgenbach, et al Phys Rev Lett 44(1980)647

30 R M Gilgenbach, et al Nucl Fusion 21(1981)319

31 R C Isler et al, 8 Proc Int Conf Plasma Phys and Controlled Nuclear Fusion Research, Brussels, 1980, paper IAEA-CN-38/A5

32 R J Hastie in Plasma Physics and Nuclear Fusion Research (ed R D Gill), Academic Press, London, 1981.

33 P H Rutherford, Princeton University, Plasma Physics Laboratory Report MATT-976 (1973)

34 V S Strelkov, 9 Proc Eur Conf on Controlled Fusion and Plasma Physics, Oxford, 2(1979)387

35 B Hui, E Ott, P T Bonoli, P N Guzdar, Nucl Fusion 21(1981)339

36 J G Cordey, T Edlington, D F H Start, Culham Lab Preprint CLM-P636 (1981)

37 P Alexandroff, H Hopf, Topologie 111(1935)552

38 J M Greene, J L Johnson, Adv Theor Phys 1(1967)195

39 I N Golovin, et al, Proc 2 United Nations Conf on Peaceful Uses of Atomic Energy, Geneva, UN, NY 32(1958)72

40 D C Robinson, R E King, 3 Proc Int Conf Plasma Phys and Controlled Nuclear Fusion Research, Novosibirsk, 1(1968)263

41 E P Butt, H C Cole, A N Dellis, A Gibson, M Rusbridge, D Wert, 1 Proc Int Conf Plasma Phys and Controlled Nuclear Fusion Research, Culham, 2(1965)751

42 M J Forrest, N J Peacock, D C Robinson, V V Sannikov, P D Wilcock, Culham Lab Report CLM-R107 (1970)

43 E I Yurchenko, Sov Phys Tech Phys 12(1968)1057

44 D G Lominadze, 'Cyclotron Waves in Plasma', Pergamon Press, Oxford, 1981.

45 S Puri, F Leuterer, M Tutter, J Plasma Phys 9(1973)89

46 K McGuire, D C Robinson, Nucl Fusion 19(1979)505

47 M J Boyle, Proc SPIE 106(1977)86

48 R C Chase, J K Silk, Appl Opt 14(1975)2096

49 N M Ceglio, H I Smith, Rev Sci Instrum 49(1978)15

50 N M Ceglio, J Appl Phys 48(1977)1563

51 J Gar, J M Forsyth, Appl Opt 17(1978)1

52 N M Ceglio, D T Attwood, E V George, J Appl Phys 48(1977)1556

53 N M Ceglio, L W Coleman, Phys Rev Lett 39(1977)20

54 K Sayanagi, J Opt Soc Am 57(1967)1091

55 P M Cambell, G Charatis, G R Marty, Phys Rev Lett 34(1971)74

56 J Bateman, M Cowlin, A Dines, P A Gaisford, R Gill, F Hoare, M Hobby, K McGuire, W Millar, A Nertney, G Sadler, P Thomas, Report on JET Design Study 17-2. (1980)

57 F C Jahoda, E M Little, W E Quinn, G A Sawyer, T F Stratton, Phys Rev 119(1960)843

58 Equipe TFR, Nuclear Fusion 17(1977)213

59 R Bardet CEA Report EUR-CEA-FC-1038 (1980)

60 R Bardet CEA Report EUR-CEA-FC-885 (1977)

61 S von Goeler, N Sauthoff, M Bitter, K Brau, D Eames, B Fraenkel, A Greenberger, K Hill, R Horton, G Hovey, J Hovey, W Roney, W Stodiek, Princeton University, Plasma Physics Laboratory, Report PPPL-1383 (1977)

62 B L Henke, R L Elgin, R E Lent, R B Ledingham, Norelco Reporter 14(1967)112

63 F Pohl, IPP-Garching Report IPP 6/193 (1980)

64 K M McGuire, D Phil thesis, Oxford University, 1980

65 K B Axon, C Wilson, Culham Lab Internal note. (1979)

66 C W Gowers, Culham Lab Internal Note TN(79)1 (1979)

67 G Lisitano, P Morandi, B Cannici, E Rossetti, N Gottardi, IPP-Garching Report IPP III/17 (1975)

68 E Apgar, B Coppi, A Gondhalekar, H Helava, D Komm, F Martin, B Montgomery, D Pappas, R Parker, D Overskei, 7 Proc Int Conf Plasma Physics and Controlled Nuclear Fusion Research, Berchtesgaden, 1976, IAEA-CN-35/A5

69 V V Sannikov, Sov Phys JETP 45(1977)63

70 J C Hosea, C Bobeldijk, D J Grove, 4 Proc Int Conf Plasma Physics and Controlled Nuclear Fusion Research, Madison (1971), IAEA-CN-28/F-7

71 D J Grove, D L Dimock, E Hinnov, J C Hosea, L C Johnson, E B Meservey, E L Tolnas, Princeton University, Plasma Physics Laboratory, Report MATT-813 (1970)

72 L A Berry, C E Bush, J L Dunlap, P H Edmonds, T C Jernigan, J F Lyon, M Murakami, W R Wing, 5 Proc Int Conf Plasma Physics and Controlled Nuclear Fusion Research, Tokyo, 1974, IAEA-CN-33/A5-2

73 J Lasalle, P Platz, Revue de Physique Appliquee 12(1977)192

74 N Bretz, D Dimock, V Foote, D Johnson, D Long, E Tolnas, Applied Optics 17(1978)192

75 H Griem in 'Plasma Spectroscopy", McGraw-Hill, NY,1964

76 K Bockasten, J Opt Soc Am 51(1961)943

77 W L Barr, J Opt Soc Am 52(1962)885

78 J Glasser, J Chapelle, J C Boatner, Applied Optics 17(1978)3750

79 P Smeulders, IPP-Garching Report IPP 2/240 (1978)

80 E W Hansen, J Opt Soc Am 71(1980)304

81 F Pohl, IPP-Garching Report IPP 6/173 (1978)

82 J Schivell, IEEE Trans Plasma Sci PS-8,No 3(1980)226

83 E Silver, W Roney, IEEE Trans Plasma Sci PS-8,No 2(1980)231

84 N R Sauthoff, Proc SPIE 106(1977)40

85 N R Sauthoff, S von Goeler, Princeton University, Plasma Physics Laboratory, Report PPPL-1447 (1978)

86 American Science & Engineering, Inc, Cambridge, Mass 02139 Report 'Magnetic Island Structure in the Alcator A Tokamak' (1979)

87 AS & E Report ASE-4422 (1979)

88 R Petrasso, M Gerassimenko, F H Seguin, J Ting, R Krogstad, P Gauthier, W Hamilton, A T Ramsey, P Burstein, Rev Sci Instrum 51(1980)585

89 T F Stratton in 'Plasma Diagnostic Techniques', (Eds Huddlestone & Leonard), Academic Press, NY, 1975

90 S von Goeler, W Stodiek, H Eubank, H Fishman, S Grebenschikov, E Hinnov, Nuclear Fusion 15(1975)301

91 W J Karzas, R Latter, Astrophys J Suppl 6,No 55(1961)167

92 P J Brussard, H C van de Hulst, Rev Mod Phys 34(1962)507

93 A L Merts, R D Cowan, N H Magee, Los Alamos Scientific Laboratory Report LA-6220-MS (1976)

94 C Jordan, Mon Not R Astr Soc 142(1969)501, and 148(1970)17

95 A Burgess, Astrophys J 139(1964)776, and 141(1965)1588

96 K M McGuire, MSc thesis, Oxford University (1977)

97 V A Piotrowicz, PhD thesis, CNAA,1981

98 Z H Cho (ed), IEEE Trans Nucl Sci NS-21(1974), Special Issue on 3-D Image Reconstruction

99 W Swindell, H H Barrett, Physics Today 30,No 12(1977)32

100 Y Yatsumoto, K Migata, S Himeno, T Enoto, Y Ozawa, IEEE Trans Plasma Sci PS-9No 1(1981)18

101 A M Cormack, Phys Med Biol 18,No12(1973)195

102 S von Goeler, W Stodiek, N Sauthoff, Phys Rev Lett 33(1974)1201

103 S von Goeler, 7 Proc Eur Conf Controlled Fusion and Plasma Physics, Lausanne, 2(1975)71

104 N Fujisawa, M Nagami, H Yokomizo, M Shimada, S Konoshima, S Seki, T Sugawara, Y Ohaza, H Ioki, G Jahns, N Brooks, R Groebner, A Kitsumezaki, Japan Atomic Energy Research Institute Report JAERI-M9181 (1980)

105 The ORMAK Group, 7 Proc Eur Conf Controlled Fusion and Plasma Physics, Lausanne, 2(1975)24

106 G L Jahns, Proc SPIE 106(1977)36

107 J D Callen, G L Jahns, Phys Rev Lett 38(1977)491

108 B V Wadell, G L Jahns, J D Callen, H R Hicks, Oak Ridge National Laboratory Report ORNL/TM-5840 (1977)

109 J L Dunlap, US-Japan Workshop on Tokamak Results, Oak Ridge, Tennessee (1980)

110 V K Pare, A P Navarro, J L Dunlap, J D Bell, W R Wing, American Physical Society, Division of Plasma Physics Meeting, San Diego, 1980

111 N R Sauthoff, S von Goeler, W Stodiek, Nuclear Fusion 18(1978)1445

112 K McGuire, N Sauthoff, R Fonek, R J Hawryluk, G L Schmidt, APS-DPP Meeting, San Diego, 1980

113 Equipe TFR, 7 Proc Eur Conf Controlled Fusion and Plasma Physics, Lausanne, 2(1975)1

114 C Breton, C De Michelis, M Finkenthal, M Mattioli, Phys Rev Lett 41(1978)110

115 N R Sauthoff, S von Goeler, D R Eames, W Stodiek, Princeton University, Plasma Physics Laboratory, Report PPPL-1553 (1979)

116 TFR Group, 9 Proc Eur Conf Controlled Fusion and Plasma Physics, Oxford, 1979, paper EP10

117 M A Dubois, D A Marty, A Pochelon, Nuclear Fusion 20(1980)1355

118 T Sugawara, N Fujisawa, M Shimada, G L Jahns, H Kokomizo, M Nagami, K Ioki, A Kitsunezaki, Japan Atomic Energy Research Institute Report JAERI-M9180 (1980)

119 A Weller, IPP-Garching Report 2/251 (1980)

120 N Fujisawa, S Konoshima, M Nagami, S Seki, H Kokomizo, M Shimada, G L Jahns, S Ejima, R Groebner, N H Brooks, A Kitsunizaki, Japan Report JAERI-M9179 (1980)

121 D A Marty, P Smeulders, D Launois, CEA Report EUR-CEA-FC-969 (1978)

122 S von Goeler, W Stodiek, H Eubank, Y Sun, P Thomson, S Slusky, Princeton University, Plasma Physics Laboratory, Report MATT-1060 (1974)

123 N D Vinogradova, Yu V Esupchuk, P E Kovrov, K A Razumova, I Szentpetery, G Hrehun, B Kardon, G Hordozy, 7 Proc Int Conf Plasma Physics and Controlled Nuclear Fusion Research, Innsbruck, 1978 IAEA-CN-37/N-3

124 R Bartiromo, A Tuccillo, CNEN Report 80.24/p (1980)

125 G R Dyer, G H Nielson, G G Kelly, Nucl Instrum Meth 161(1979)365

126 P Blanc, P Brouquet, N Uhre, CEA Report EUR-CEA-FC-962 (1978)

127 P Brouquet, CEA Report EUR-CEA-FC-1002 (1979)

128 P Blanc, P Brouquet, N Uhre, Nucl Instrum Meth 159(1979)375

129 S Suckewer, E Hinnov, J Schivell, Princeton University, Plasma Physics Laboratory, Report PPPL-1430 (1978)

130 E Hinnov, M Mattioli, 5 Culloquium on UV and X-Ray Spectroscopy, London, 1977

131 N Bretz, D Dimock, A Greenberger, E Hinnov, E Merservey, W Stodiek, S von Goeler, 5 Proc Int Conf Plasma Physics and Controlled Nuclear Fusion Research, Tokyo, 1974, IAEA-CN-33/A3-1

132 S von Goeler et al, 2 Conf on Hot Plasma Diagnostics, Kharkov, USSR, 1977

133 B S Fraenkel, X-Ray Spectroscopy 9(1980)189

134 P Platz, J Ramette, E Belin, C Bonnelle, A Gabriel, CEA Report EUR-CEA-FC-1057 (1980)

135 M Klapisch, J L Schwob, M Finkenthal, B S Fraenkel, S Egert, A Bar-Shalom, C Breton, C De Michelis, M Mattioli, Phys Rev Lett 41(1978)403

136 S Suckewer, Physica Scripta 23(1981)72

137 C De Michelis, M Mattioli, CEA Report EUR-CEA-FC-1084 (1981)

138 R A Brooks, G Di Chiro, Radiology 117(1975)561

139 TFR Group, Plasma Physics 19(1977)349

140 K M McGuire, D C Robinson, A J Wootton, 7 Proc Int Conf on Plasma Physics and Controlled Nulcear Fusion Research, Innsbruck, 1978, IAEA-CN-37/T-1-1

141 Equipe TFR, Nuclear Fusion 18(1978)647

142 D A Gedcke, X-Ray Spectrometry 1(1972)129

143 R C Trammell, IEEE Trans Nucl Sci NS-25,No 2(1978)910

144 M W D Mansfield, Culham Lab Internal Note TN(78)21 (1978)

145 L A Artsimovich, A V Glukhov, M P Petrov, Zh E T F Pis Red 11(1970)449

146 K Toi, S Itoh, K Kadota, N Noda, K Sakurai, K Sato, S Tanahashi, S Yasue, Nuclear Fusion 19(1979)1643

147 G J Boxman, B Coppi, L C J M de Kock, B J H Meddens, A A M Oomens, L T M Ornstein, D S Pappas, R R Parker, L Perioni, S E Segre, F C Schuller, R J Taylor, 7 Proc Eur Conf on Controlled Fusion and Plasma Physics, Lausanne, 1975, 2(1975)14

148 J E Rice, K Molvig, H I Helava, Massachussetts Institute of Technology Report PFC/JA-81-5 (1981)

149 U Ascoli-Bartoli, et al, CNEN Report 80.8/p (1980)

150 L Pierone, S E Segre, Phys Rev Lett 34(1975)928

151 B Lloyd, Culham Lab, private communication

152 B Lloyd, Culham Lab internal note TN(81)2 (1981)

153 B B Kadomtsev, O P Pogutse, Nuclear Fusion 11(1971)67

154 T C Hender, Culham Lab, private communication

155 M W Alcock, P R Collins, N R Ainsworth, in Joint Workshop on ECE and ECRH, Culham Lab Publication CLM-ECR(1980)

156 F S Goulding, D A Landis, IEEE Trans Nucl Sci NS-25,No 2(1978)896

157 H A B Bodin, A A Newton, Nuclear Fusion 20(1980)1255

158 L A Berry, J D Callen, J F Clarke, R J Colchin, E C Crume, J L Dunlap, P H Edmonds, G R Haste, J T Hogan, R C Isler, G L Jahns, N H Lazar, J F Lyon, M Murakami, R V Neidigh, W R Wing, 5 Proc Int Conf on Plasma Physics and Controlled Nuclear Fusion, Tokyo, 1(1974)101

159 V A Piotrowicz, Culham Lab, private communication

160 D C Robinson, Culham Lab note 'Electron Temperature Measurement by Laser Light Scattering from the Zeta Plasma', 1967, TPGN-82

161 C Breton, C De Michelis, M Mattioli, CEA Report EUR-CEA-FC-853 (1976)

162 J Hugill, Nuclear Fusion 23 No 3(1983)

163 D Green, (ed.) Plasma Formulary, US Naval Research Laboratory, Washington, D.C. 20375

164 W Schottky, in Zeitschrifft fuer Physik, Berlin, 1942(?).

164 B Lloyd, Culham Lab internal note TN(81)4 (1981)

APPENDIX - PUBLISHED PAPERS

Contributions to the 10th European Physical Society Conference on Controlled Fusion and Plasma Physics, Moscow, September 1981.

1 'High Power ECRH at the Second Harmonic in TOSCA', M W Alcock, P A Gaisford, B Lloyd, A W Morris, W A Morris, R Peacock, D C Robinson, M A Protheroe, and Y Wen.

2 'Local Heating and Current Drive Investigations in TOSCA', M W Alcock, T Edlington, P A Gaisford, T C Hender, B Lloyd, and D C Robinson.

Contribution for the 10th EPS Conf. on Controlled Nuclear Fusion and Plasma Physics, Moscow, Sept. 1981.

HIGH POWER ECRH AT THE SECOND HARMONIC IN TOSCA

M W Alcock, P A Gaisford*, B Lloyd**, A W Morris**, W A Morris, R Peacock, D C Robinson, M A Protheroe* and Y Wen***

Culham Laboratory, Abingdon, Oxon, OX14 3DB, UK
(Euratom/UKAEA Fusion Association)

*Royal Holloway College, University of London
**University of Oxford, ***Peoples' Republic of China

ABSTRACT ECRH experiments at 28GHz, power levels of 20→150kW and at the second harmonic have been performed. Theory predicts strong absorption and local heating and both are observed. The loop voltage can be decreased by 50%, the plasma energy content increases and a current redistribution occurs.

INTRODUCTION High power ECRH has been applied to plasmas in the TOSCA device [1] with λ=1cm, a pulse length of up to 2ms and at a power level of up to 150kW from the low field side of the torus using the circularly polarised TE_{02} mode. The objective of these experiments is to increase beta, control the current distribution and investigate current drive. The regions in which auxiliary heating has been investigated were $0.4T < B_\phi < 0.6T$, $6kA \leq I \leq 14kA$, $2.5 \times 10^{18} m^{-3} \leq \bar{n}_e \leq 1.5 \times 10^{19} m^{-3}$. The plasma position was controlled in some experiments with a fast feedback system with a time constant of 40μs. The effectiveness of heating at the second harmonic has been confirmed experimentally[2] and local efficient heating for an optically thin plasma at the second harmonic predicted[3]. The theoretical calculations which include wall reflections indicate that strong local heating for the X-mode at small radii is favoured by a geometrical effect of the flux-surface and resonance configuration. Figure 1 shows the variation of the predicted heating profile with increasing central density for the X-mode. The profile moves outwards at higher densities due to the presence of the low density X-mode cut-off.

EXPERIMENTAL RESULTS Figure 2 shows a number of the characteristics associated with the heating pulse, namely a decrease in the loop voltage by up to 50% (e.g. 1.6V to

0.8V), an increase in the plasma current of typically 10% (associated with a decrease in plasma inductance), no change in the plasma density (in contrast to heating studies at the fundamental), an outward displacement of the plasma column, an increase in the local soft X-ray emission (E∿1keV) in the resonant region and an increase in the cyclotron emission at 35 GHz. An increase in the transverse energy of the plasma is also observed with a diamagnetic loop. No significant increase in the emission or impurity radiation at 4647Å (OII) is observed. The cyclotron emission is observed with a super heterodyne detector employing a local oscillator tunable from 28-40GHz. The emission is typically observed to increase by a factor of 2 or 3 upon injection of a 100kW pulse from the gyrotron. The rise and fall times are usually comparable to the bulk energy confinement times. The role of superthermal electrons is not yet fully established partly because of harmonic overlap and the initial emission in Fig.2 is

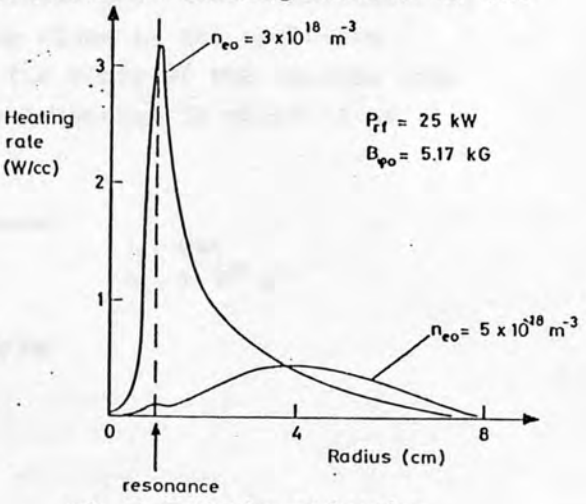

Fig. 1 Variation of heating profile with density

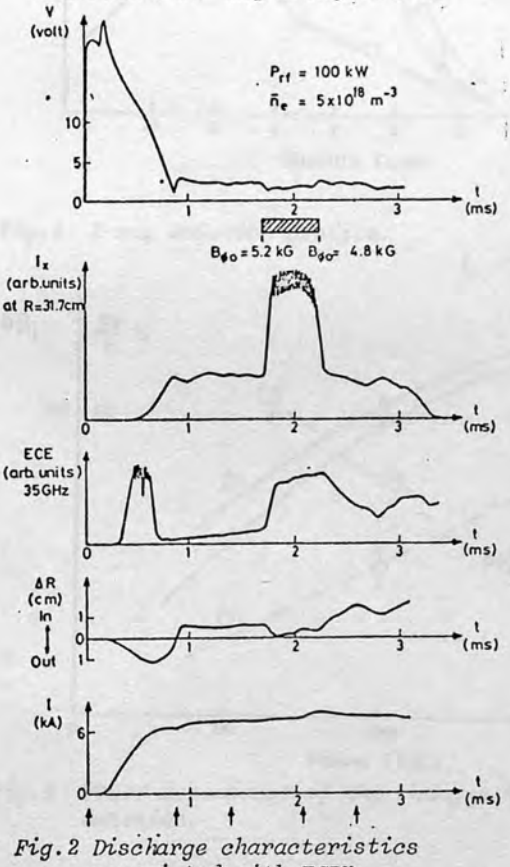

Fig. 2 Discharge characteristics associated with ECRH. (Arrows shown bank timings.)

correlated with the presence of high energy electrons, as observed on a Si(Li) detector. The soft X-ray emission observed vertically at seven spatial positions simultaneously indicated strong local heating close to the cyclotron resonance as shown in Fig.3. The width of the heating zone is typically 20mm and the local heating is observed at

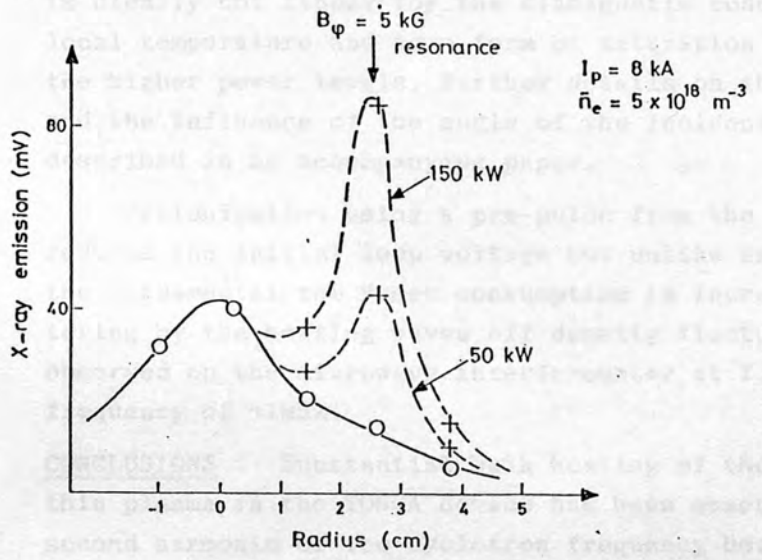

Fig.3 X-ray emission profile.

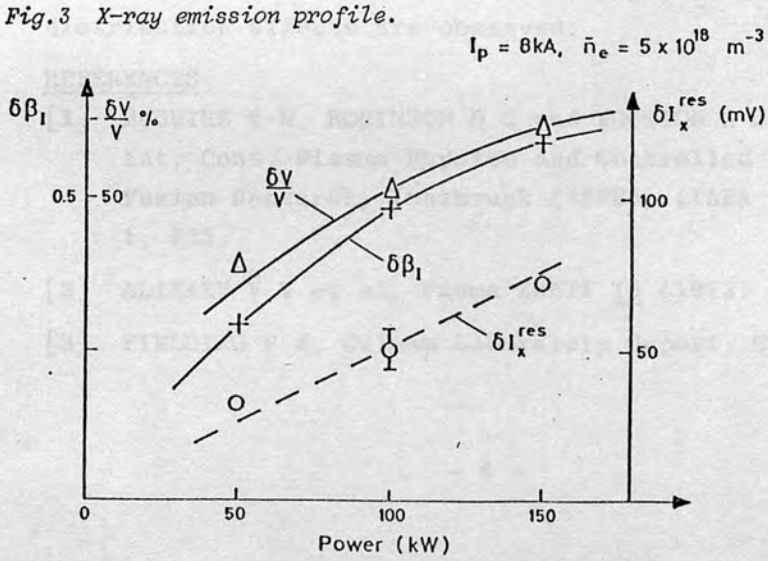

Fig.4 Power dependence of the changes in loop voltage, β_I and X-ray emission.

densities both above and below the X-mode cut-off value, in contrast to theoretical predictions which indicate that tunnelling through the evanescent layer is not expected to be significant. At these temperatures (∿300eV) the emission signal is approximately proportional to T^2 so that a substantial rise in local temperature occurs. The power dependence of some of the discharge characteristics is shown in Fig.4. The dependence is clearly not linear for the diamagnetic conductivity and local temperature and some form of saturation is indicated at the higher power levels. Further details on the local heating and the influence of the angle of the incident radiation are described in an accompanying paper.

Preionisation using a pre-pulse from the gyrotron reduces the initial loop voltage but unlike experiments at the fundamental the V.sec consumption is increased. Scattering by the heating waves off density fluctuations is observed on the microwave interferometer at 1.4mm and at a frequency of ∿1MHz.

CONCLUSIONS Substantial bulk heating of the optically thin plasma in the TOSCA device has been observed at the second harmonic of the cyclotron frequency both above and below the X-mode cut-off. Local absorption and current redistribution effects are observed.

REFERENCES

[1] McGUIRE K M, ROBINSON D C and WOOTTON A J, Proc. 7th Int. Conf. Plasma Physics and Controlled Nuclear Fusion Research, Innsbruck (1978), (IAEA Vienna, 1979), 1, 335.

[2] ALIKAEV V V et al, Pisma ZhETF 15 (1972) 41.

[3] FIELDING P J, Culham Laboratory Report, CLM-P615 (1980).

Contribution for the 10th EPS Conf. in Moscow, Sept. 1981

LOCAL HEATING AND CURRENT DRIVE INVESTIGATIONS ON TOSCA

M W Alcock, T Edlington, P A Gaisford*, T C Hender*,
B Lloyd** and D C Robinson

Culham Laboratory, Abingdon, Oxon, OX14 3DB, UK
(Euratom/UKAEA Fusion Association)

*Royal Holloway College, University of London
**University of Oxford.

ABSTRACT ECRH experiments at the second harmonic show local heating when the cyclotron resonance is on the outer flux surfaces. Above a critical power level this induces continuous m=1 activity in the heating zone. The local heat conduction coefficient is close to the INTOR value and the parallel heat conduction may be anomalous. Attempts to detect a wave driven current using a variable angled antenna ($\pm 50^{o}$) indicates that the current is less than 3A/kW in the plasmas used in these investigations.

INTRODUCTION The resonance zone width for ECRH is generally much less than the plasma radius and localised heat-

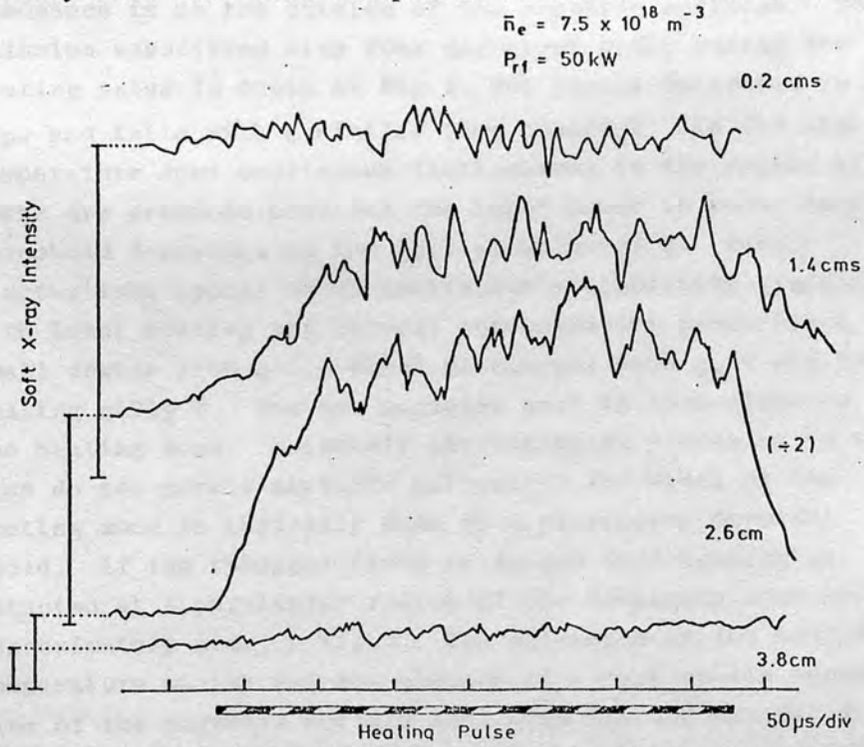

Fig.1 Soft X-ray emission from four radii during the heating pulse.

ing is possible in an optically thick plasma, when the directionality of the injected radiation is controlled. This is important for current profile and instability control and heat conduction studies. Even in an optically thin plasma when one must take account of reflections there is a geometrical effect[1] which permits strong local maxima in the heating profile thus allowing such investigations in small tokamaks. Theory[2] also indicates that cyclotron waves should be suitable for generating a current if the absorption is predominantly on one side of the resonance which is possible for the X-mode in a small tokamak at sufficiently high temperatures with the waves launched preferentially in one direction.

LOCAL HEATING EXPERIMENTS The soft X-ray emission observed vertically from a seven channel diode array indicates that strong local heating occurs close to the cyclotron resonance both above and below the X-mode cut-off provided the resonance is on the outside of the magnetic surfaces. The emission associated with four different radii during the heating pulse is shown in Fig.1. The signal saturates in some 50μs and falls with a similar time constant. In the high temperature zone continuous fluctuations in the region of 50kHz are produced provided the input power is above some threshold dependent on the initial value of q. These fluctuations appear to be continuous m=1 activity associated with local heating and current concentration producing a small region with $q<1$. These discharges have $q_a \sim 7$ and before heating $q(0) \lesssim 2$. The new magnetic axis is thus close to the heating zone. Evidently the transport processes in this case do not permit sawtooth activity. The width of the heating zone is typically 20mm at a particular toroidal field. If the toroidal field is varied then heating is detected at a particular radius if the resonance zone moves approximately 30mm, - Fig.2. The existence of two sustained temperature maxima and the absence of a peak on the opposite side of the magnetic surface indicates the 2-D nature of the heat conduction process in the tokamak. We have used a 2D

anisotropic heat conduction and field diffusion code with a local heating source to simulate this behaviour. The experimental results can be reproduced by reducing the parallel heat conduction by 100 x as shown in Fig.3.

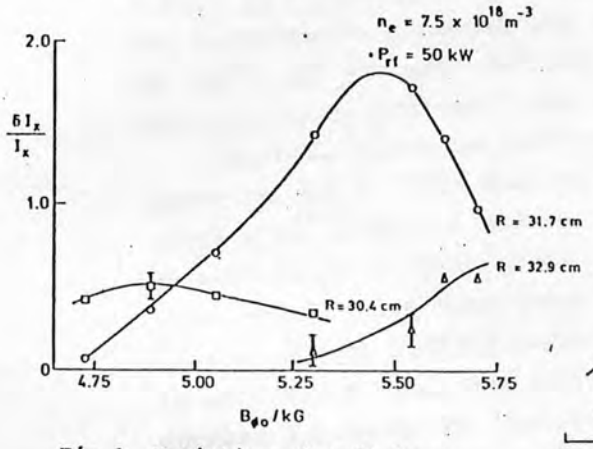

Fig. 2 Variation of soft X-ray emission at three-radial positions with toroidal field.

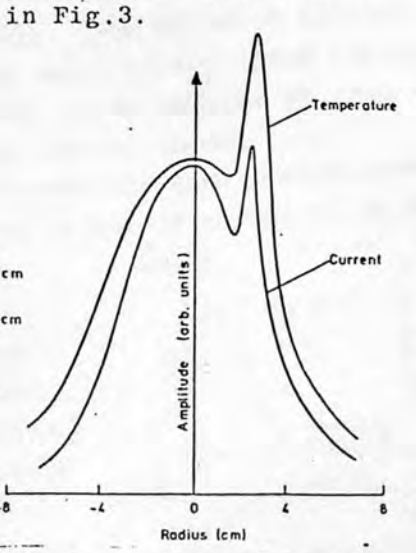

Fig. 3 Temperature and current profile associated with anomalous parallel heat conduction.

From the heating and decay times and the width of the heating zone we obtain a local average heat conduction coefficient of 0.5 m^2s^{-1} in the hot core of the plasma which is about six times smaller than the average INTOR value. An alternative explanation for the failure of the temperature to be uniform on a magnetic surface is that the ECRH produces perpendicular runaway and electrons with energies of $\sim$ 3keV become trapped with large banana orbits of width $\sim$1-2cm, which is in accord with the observed absence of local heating on the high field side of the plasma. No evidence for this non-thermal perpendicular electron distribution has however been obtained.

CURRENT DRIVE EXPERIMENTS Theoretical ray tracing and absorption calculations for the X-mode in TOSCA at a central density of 4.5x$10^{18}m^{-3}$ and temperatures of 600eV indicate that a net current of some 30A/kW should be produced. The calculations suggest that the optimum angle of injection is less than 14^o and that although the single pass absorption

can be quite high (80%) the local current produced on one side of the resonant layer is approximately cancelled by that on the opposite side of the layer. This should produce a substantial change in the current profile and is likely to excite mode activity. The directed antenna in the experiments produces its power in two lobes (normally at $\pm 20^{o}$), at $+8^{o}$ and $+48^{o}$ and can be rotated so that one lobe should be efficient for current drive.

Typical discharge waveforms for such an experiment are shown in Fig.4. The heating is not as efficient as for the usual $\pm\ 20^{o}$ antenna and in general the soft X-ray emission is not fully sustained throughout the heating pulse. In both directions, the plasma current increases by typically 10% associated with the decrease in inductance, and resistance but there is a difference in the two directions of up to 300 amps for 100 kW input. As with the perpendicular antennae the high power ECRH does not produce run-away discharges.

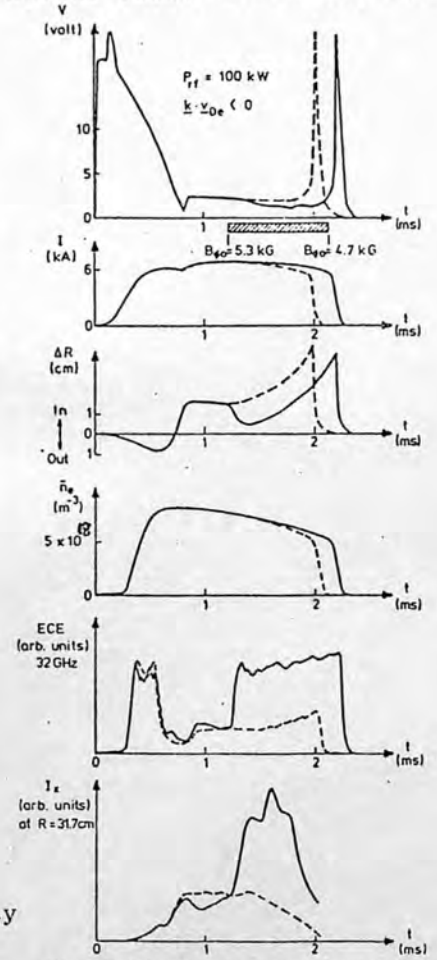

Fig.4 Discharge waveforms for a directed antenna.

CONCLUSIONS The local heating on the outer flux surfaces may be associated with anomalous parallel heat conduction or with the presence of perpendicular electron runaway leading to a build up trapped electrons. The efficiency for current drive in these experiments appears to be low, possibly because the single pass absorption is low.

REFERENCES

[1] FIELDING P J, Culham Laboratory Report, CLM-P615 (1980).
[2] CORDEY J G et al, Culham Laboratory Report, CLM-P636 (1981)